UNIVERSITY
OF TRENTO - Italy
DEPARTMENT OF INDUSTRIAL ENGINEERING

XXVIII cycle

-

Doctoral School in Materials Science and Engineering

Biodegradable stents made of pure Mg and AZ91 alloy through SPS sintering

Pedro Augusto de Oliveira Botelho

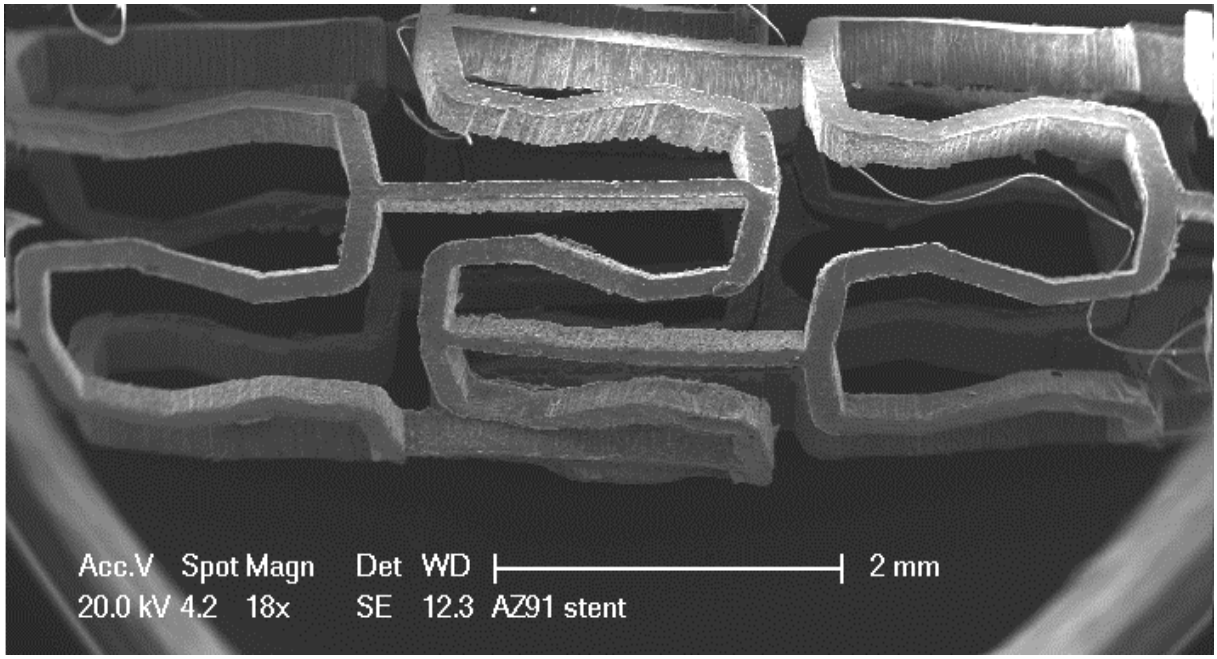

November 2015

BIODEGRADABLE STENTS MADE OF PURE MG AND AZ91 ALLOY THROUGH SPS SINTERING

Pedro Augusto de Oliveira Botelho
E-mail: pa.deoliveirabotelho@unitn.it
pedroabotelho@gmail.com

Approved by:

Prof. Giovanni Straffelini, Advisor
Department of Industrial Engineering
University of Trento, Italy.

Ph.D. Commission:

Prof. Emanuela Cerri,
Department of Industrial Engineering
University of Parma, Italy.

Prof. Nuno M. Neves,
Department of Polymer Engineering
University of Minho, Portugal.

Prof. Antonella Motta,
Department of Industrial Engineering
University of Trento, Italy.

University of Trento,
Department of Industrial Engineering

November 2015

University of Trento - Department of Industrial Engineering
- - - - - - - - -

Doctoral Thesis

Pedro Augusto de Oliveira Botelho - 2015
Published in Trento (Italy) – by University of Trento

ISBN: - - - - - - - - -

To my beloved wife
and my children

Abstract

The implantation of stents is an effective procedure to unblock the arteries of patients with serious heart problems. Traditionally, stents are made of inert materials such as stainless steel and titanium alloys. It has been shown that the traditional stents can cause restenosis or thrombosis. In recent years the proposal of biodegradable stents is attracting the interest of the industry and the research, since the stent is mechanically needed only in the first year, eliminating the problems caused by the long duration of the implant.

Magnesium (Mg) alloys are of increasing interest because of their engineering properties, including the high strength to density ratio. Recently, they have been also proposed as biomaterials for the production of bioabsorbable stents and for other medical devices due to its harmless effect to human body when compared with other structural materials.

In this work, the possibility to produce biodegradable stents made of magnesium starting from the powder is investigated. Pure Mg and the AZ91 Mg powders were used in the present study. Pure Mg powder was sintered by Spark Plasma Sintering at 400 and 470 °C, and the AZ91 powder was sintered at 400 °C without homogenization and at 470 °C after homogenization.

The preforms produced by sintering were then submitted to hot compression, rod extrusion and tube extrusion at 330 and 380 °C with different strain rates. During all the process was not possible to obtain recrystallization or grain refinement on pure Mg, and after the tube extrusion it has shown a high brittleness and sever defects, which led to the decision of proceed only with AZ91 alloy.

The AZ91 presented good recrystallization in al process, always following the Zener-Hollomon relation. The grain size obtained was as small as 1.5 μm. The AZ91 tube was then submitted to manual machining and laser cutting and it was possible to obtain the stent precursors.

The results of the present investigation have demonstrated the suitability of the proposed route for producing Mg-based stents. It is clear, however, that the process has to be further optimized, investigating also the possibility of using different types of powder with a tailored composition.

Table of contents

Chapter I

Introduction

Mg alloys are of increasing interest because of their engineering properties, including the high strength to density ratio. Recently, they have been also proposed as biomaterials for the production of bioabsorbable stents [1], [2] and for other medical devices due to its harmless effect to human body when compared with other structural materials [1–3].

Usually, these alloys are produced by casting technologies and then submitted to hot working processes. The Powder Metallurgy (PM) route is not largely used for Mg alloys because the powders display a high reactivity to oxygen and thus, easily form oxides on their surfaces, which render quite difficult the sintering process [3]. However, for biodegradable stents, very small grain size is required, in first place because it enhance the mechanical properties [4–6], and also to improve corrosion behaviour [1], [7], thus, the goal of selecting powder metallurgy (PM) technique is to start with a small grain and try to reduce it even more through extrusion. The possibility of using PM is possible to produce reliable stents, open a wide field of research to develop new alloys that can improve the final product. The proposed fabrication route of the stents would be as follows:

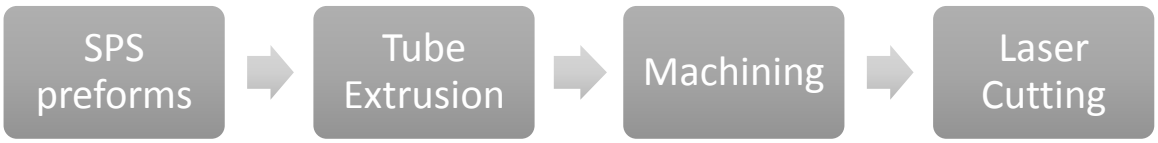

Within PM techniques, the spark plasma sintering (SPS) showed to be highly effective on breaking the oxide layers of the particle and giving good densification of sintered Mg alloys [3], [8]. The possibility of producing cylindrical powder preforms made by pure Mg and AZ91 alloy (with nominal

chemical composition: 90Mg-9Al-1Zn-Mn, in wt %), using Spark Plasma Sintering (SPS) has been investigated.

Pure Mg was sintered at 400 and 470 °C and further submitted to hot compression and hot extrusion. However, under tube extrusion presented serious problems on the integrity of the material and the investigation continued only with the AZ91 alloy

On AZ91, the sintering was also performed at 400 and 470 °C. The presence of a eutectic reaction between the Mg rich α-phase and the γ-phase (with nominal composition $Mg_{17}Al_{12}$), that produces a liquid at about 440 °C is proved to be harmful for SPS. To avoid the formation of such phase and be able to achieve the temperature of 470 °C, a solubilisation treatment was introduced into the sintering cycle.

The behaviour of the AZ91 under hot compression and rod extrusion was also investigated. Both the hot compression and rod extrusion were performed at 330 °C and 380 °C at strain rates of 0.056 s^{-1} and 0.002 s^{-1}. The material has shown a good consolidation after SPS, grain refinement after extrusion and decrease of γ-phase during the SPS process and on the extrusions performed at 380 °C. The extrusion of tubes can improve even more the results obtained before, since it promotes a higher strain, allowing the dynamic recrystallization to occur and as result obtaining a more refined and homogenized microstructure.

In order to prepare the tubes to the laser cutting, the wall thickness must be reduced from 2 mm to about 0.35 mm; such reduction will be achieved by turning. It is very important that the tolerances are followed, to ensure a good laser cut.

Laser cutting is a widely used technique used to produce metallic stents [9–15]. The main advantage is to be a noncontact cutting method and to be capable of cut very precise and complex shapes [16]. Lasers can cut stents of a wide range of materials, such as stainless steel, Nitinol and also magnesium alloys [1]. Many aspects can influence on the final quality of the laser cutting, the tube geometry, surface roughness and large precipitates on the microstructure for example.

Chapter II

Literature Review

2.1. Biodegradable Stents

2.1.1. Cardiovascular diseases

Cardiovascular diseases are disorders of the blood vessels and/or the heart, which results in a decreased supply of blood to certain physiological body areas. The insufficient blood supply to the heart, for example, result in the rapid shortage of oxygen to the cardiac cells, due to ischemia, which, if prolonged, can lead to necrosis of a part of the cardiac tissue, with relative circulatory problems in other districts [17].

Vascular diseases are the leading cause of death in industrialized countries (48% for a total of 2 million deaths per year) [18]. Most of these diseases are linked to atherosclerosis, a chronic inflammatory disease of the arteries that occurs because of cardiovascular risk factors, such as: smoking, air pollution, high cholesterol, diabetes, hypertension and obesity [18].

Atherosclerosis is an extremely frequent arterial disease characterized by the formation of fibroadipose plaques, known as atheroma or atherosclerotic plaques in the thickness of the inner layers of the arteries wall. This alteration of the vessel wall occurs, preferentially, in the arteries of large and medium size, such as the aorta, the coronary arteries, kidney and brain, in particular in correspondence of bifurcations. Anatomically, the atheroma makes the storage of lipids in the artery, mainly represented by the cholesterol carried by lipoproteins. Monocytes present in the blood are recruited from the vessel wall and are transformed into macrophages that phagocytose these substances causing, locally, inflammatory events, which determine the migration and proliferation of smooth muscle cells and the formation of a fibrotic capsule that can calcify. These events culminate in the destruction of the elastic tissue,

muscle and in the formation of a scar-like fibrous tissue. The artery also tends, in part because of calcification, to stiffen and become clogged, not allowing an adequate passage of blood flow (Fig. 2.1) [17].

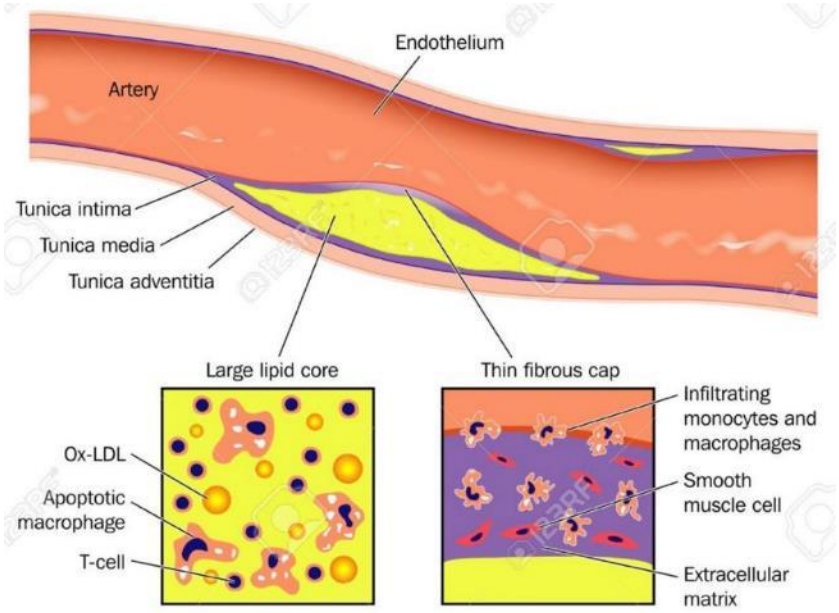

Fig. 2.1 - Formation of atheroma. The deposit of lipids in the tunica intima of the artery due to the recruitment of monocytes that transform into macrophages engulfing these substances and causing the migration of smooth muscle cell proliferation and the formation of a scar-like fibrous tissue.

Gradually the lumen of the artery tends to narrow (called stenosis). The reduction of the vascular lumen, caused by stenosis, decreases the irrigation of the tissues, and if the vessel is completely closed, can lead to cell death and consequent necrosis [17].

Other diseases resulting from atherosclerosis are acute coronary syndrome and thrombosis. Clinical symptoms of acute coronary syndrome are manifested by the formation of a thrombus large enough to obstruct the lumen of the coronary artery and slow the flow of blood. Thrombosis is the rupture of atherosclerotic plaque due to the higher speeds that are consequence of the narrowed lumen. The rupture of the capsule fibro-adipose puts in contact the contents of the plaque with the blood and induces the adhesion, aggregation, and platelet activation with consequent formation of thrombi [17].

2.1.2. Surgical solutions

Over the years, different therapeutic approaches have been proposed for the treatment of atherosclerotic diseases. In 1969 the first coronary artery bypass grafting (CABG) was performed, which consists to suture a section of saphenous vein, mammary artery or artificial tubes made of PTFE® and Dacron®, respectively for small vessels (diameter less than 6 mm) and medium/large calibre upstream and downstream of the occluded coronary artery in order to circumvent the stenosis and restore normal blood flow to the heart. This type of intervention is, however, very invasive because it is an open surgery with a need for extra-corporeal circulation. All this involves the risk of complications such as bleeding, infection, stroke, kidney failure, heart attack and pre- and post-operative re-clogging of the bypass time.

Gruentzig proposed a different approach for these problems in 1977, who introduced a new surgical technique called percutaneous transluminal coronary angioplasty (PTCA), showed on Fig. 2.2 [19]. PTCA is a minimally invasive surgical technique that consists of inserting a balloon catheter through the obstructed artery, which is pushed inside the lumen until reaches the local of occlusion, and then is inflated, pressing the plaque against the walls of the vessel and re-opening the artery lumen, thus restoring proper blood flow. After the expansion, the balloon is deflated and removed from the vessel.

The main problem lies in the PTCA reocclusion of the vessel (restenosis), found in 30-40% of cases treated with this treatment within 6 months after surgery [20].

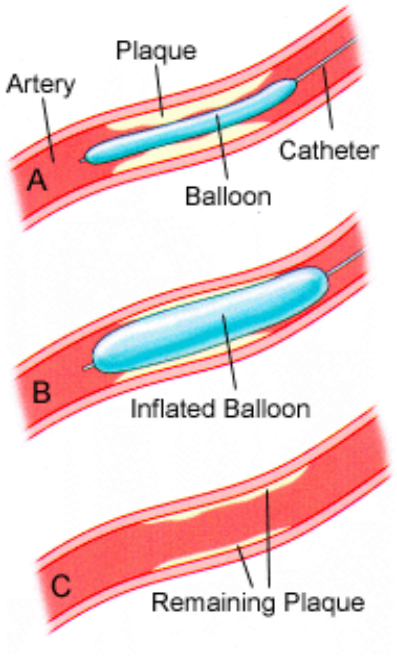

Fig. 2.2 - PTCA technique. A balloon catheter is pushed inside the lumen until reaching the local of occlusion, and thereafter inflated in order to press the plaque against the walls of the vessel and reopen the artery lumen, restoring the proper blood flow.

2.1.3. Stent implant approach

In 1986, Sigwart and Puel made safer technique of angioplasty realizing the first responders to the coronary arteries using stents. The stent is a cylindrical mesh, which is pushed into the lumen of the artery by a catheter and when located at the stenosis, is expanded at the level of the obstruction until its diameter is equal to that of the original lumen of the vessel in such a way to reduce the stenosis.

Generally, stents are produced in two different ways:

- by arranging and welding very thin wires (up to 0.076 mm of diameter) in order to obtain the desired structure;
- by extrusion of metal hollow pipes with a very thin wall, subsequently machined with laser cutting technology, obtaining, the desired geometry without the need for mechanical or thermal joints [21].

Typically, a stent has a wall thickness varying between 0.056 and 0.2 mm, inner diameter before expansion from 0.99 to 1.15 mm and, after expansion, the outer diameter and the length can reach values, respectively from 2 to 6

mm and 7 to 45 mm [21]. The materials typically used commercially for the manufacture of stents are: AISI 316L stainless steel, shape-memory alloy Nitinol (Ni-Ti), and alloys Cobalt- Chromium (Co-Cr). There are also other materials being tested, such as iron, magnesium and its alloys, platinum-iridium (Pt-Ir) alloys, and tantalum (Ta). The mechanical properties of these materials are summarized in Table 2.1, where we can observe the mechanical characteristics of the materials used for the study and the production of the stent, shown next to the AISI 316L steel, the material mainly used for the manufacture of vascular stents.

Table 2.1- Mechanical properties of the main metals used to produce cardiovascular stents [20].

Metal	Elastic modulus (GPa)	Yield strength (MPa)	Tensile strength (MPa)	Density (g/cm^3)
316L stainless steel (ASTM F138 and F139; annealed)	190	331	586	7.9
Tantalum (annealed)	185	138	207	16.6
Cp–Titanium (F67; 30% cold worked)	110	485	760	4.5
Nitinol	83 (Austenite phase)	195–690 (Austenite phase)	895	6.7
	28–41 (Martensite phase)	70–140 (Martensite phase)		
Cobalt–chromium (ASTM F90)	210	448–648	951–1220	9.2
Pure iron	211.4	120–150	180–210	7.87
Mg alloy (WE43)	44	162	250	1.84

Regarding the implant of the stents, they are classified as:

1) Balloon-expandable stents are usually obtained through the laser cut from a tube extruded in AISI 316L stainless steel and cobalt-chromium alloy having a diameter of 2.50 to 4.50 mm. Such stents are mounted on a balloon catheter in its closed configuration and undeformed shape, and then plastically deformed at the site of occlusion by the application of a high pressure (Fig. 2.3).

2) Self-expanding stents (Fig. 2.3) are made of nickel-titanium alloys (Nitinol), with the property of shape memory materials able to recover the initial shape even after high strains. In this case, the stent is obtained starting from a tube of Nitinol having the same diameter of the vessel (or slightly higher), then elastically deformed and introduced into the closed configuration and the deformed up to the site of occlusion by means of a guide catheter.

Subsequently, the guide catheter is retracted and the stent expands elastically, returning to its original size [22].

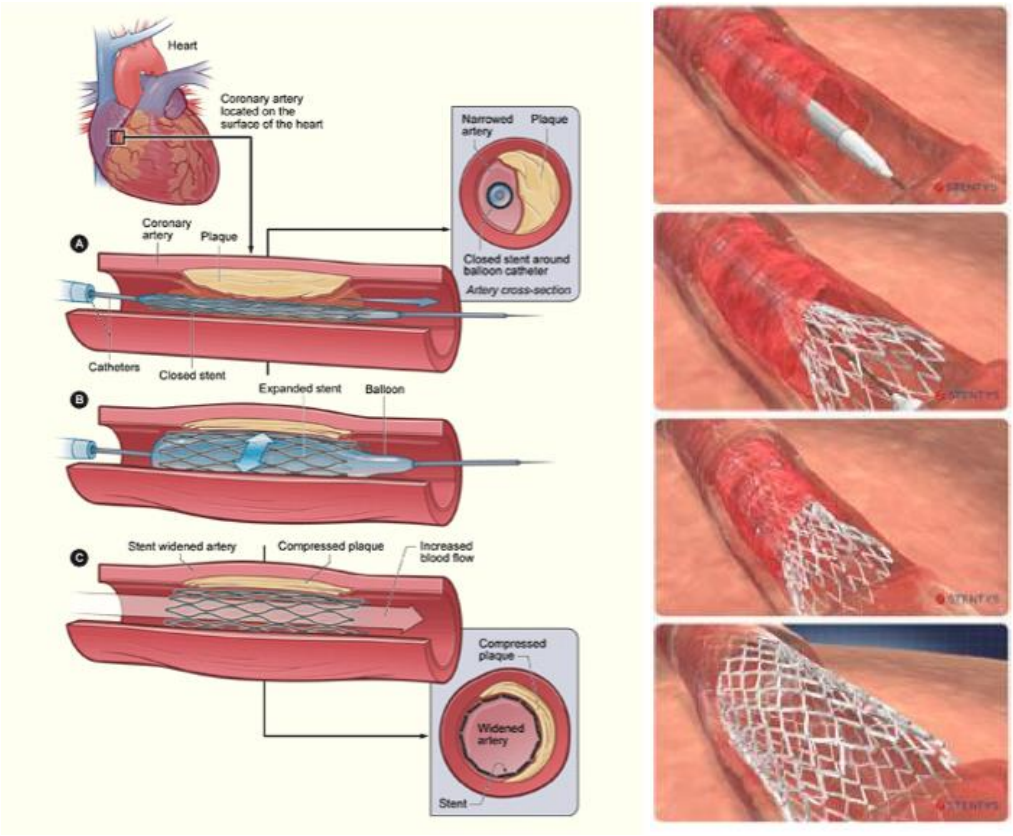

Fig. 2.3 - An example of balloon expandable stent on the left and a self expandable stent on the right.

In general, the characteristics that a stent must possess are the following [20]:

- Ability to be crimped into the catheter guide;
- The contact surface stent/vessel must be as small as possible;
- Adequate flexibility for the positioning step;
- Good expandability once reached the site of interest and the balloon is inflated (balloon expandable stents);
- Sufficient radial strength to withstand the forces imposed by the vessel atherosclerosis and without collapsing;
- Radiopacity, i.e., the ability to be detected by technologies such as x-ray;
- Hemocompatible, to prevent platelet adhesion and therefore the phenomenon of restenosis.

Restenosis is the most common complication associated with the implant of a coronary stent and is caused by the migration and proliferation of smooth muscle cells in the intima of the vessel wall, with the formation of the called neointima, a smooth muscle tissue within the lumen that tends to proliferate excessively (neointimal hyperplasia) and reobstruct the vessel. The recruitment and proliferation of smooth muscle cells it is part of the normal inflammatory process due to the damage that the stent causes the endothelium. Other complications may be due to perforation of the wall during the expansion of the stent or the migration of the same in other body sites.

Consequently, in recent years, research activity has focused on the reduction of excessive growth of neointima to minimize the phenomenon of stent restenosis. Stents of different geometry and design have been developed. In the early 1990s it was developed the Drug Eluting Stent (DES) to try to prevent restenosis. It consists of a stent coated with a polymeric material loaded with a drug with antiproliferative action, to prevent muscle cell proliferation and intimal hyperplasia. The drugs most frequently used are sirolimus and paclitaxel. The drug release is needed especially in the first stage after implantation, because it is in this time that can occur the formation of neointima.

The first-generation DES were made using a metal structure, usually made of stainless steel AISI 316L, covered with a layer of non-biodegradable polymeric material. Several studies [23], [24] have shown that drug-eluting stents, introduced into clinical practice in 2001, have reduced effectively the stent restenosis, when compared to common metal stent and also reduced the phenomena of neointimal hyperplasia [25].

Nevertheless, the results are still not completely satisfactory, due to some intrinsic problems, such as the persistence of polymer coating even after the completion of the drug release, that has been associated with thrombotic occlusion of the system [23]. The release of antiproliferative drugs inhibits the migration and proliferation of smooth muscle cells. However, the drugs currently used have effect not only on smooth muscle cells, but also on endothelial cells with the result that, in this case, it inhibits the process of

endothelialization. A normally functioning endothelium intact and is vital in preventing the activation of the coagulation cascade and platelet activation. This implies that the risk of late stent thrombosis is the major concern regarding the use of drug eluting stents.

Studies of patients who died due to an event of late stent thrombosis have shown that DES coated with non biodegradable polymer able are associated with a persistent inflammation of the arterial wall and delayed healing characterized by a reduced endothelialization of the structure of the stent, when compared to common metal stents.

2.1.4. Biodegradable Stent

One of the most promising solutions proposed to solve such problems is to produce stents made of biodegradable material. The role of stenting becomes temporary: once restored the physiological lumen, the presence of the stent in the body becomes unnecessary; eliminating the stent, is possible to avoid restenosis.

The materials applied for the biodegradable stents must be biocompatible, biodegradable and the degradation products must produce no harm to human body. In addition, the rate of degradation of the stent must be such as to maintain the mechanical characteristics required during the process of remodeling and healing of the vessel [26]. It is essential that the loss of cohesion and mechanical strength of the stent during the resorption is by the support offered by the newly formed tissue. In addition, the candidate material should, ideally, possess mechanical properties close to those of stainless steel AISI 316L, the most used material for the manufacture of coronary stents and often considered as a reference for the development of new material applied to stent production.

The rate of degradation of the stent must be very slow in the beginning, in order to maintain the mechanical integrity during the healing of the vessel. A period of 6-12 months with adequate mechanical characteristics is required to complete the process of remodelling and healing of the vessel. Subsequently,

as the mechanical integrity of the stent decreases, the degradation has to progress at a speed that does not cause a build-up above the physiological limits of the degradation products around the implant site. A total period of 12-24 months after the implant is considered a reasonable time for the complete degradation of the stent [26].

Based on these requirements, two classes of materials have been proposed for the realization of biodegradable stents: polymers and metals. Despite the advantages, at the moment there are two major obstacles to the use in a large scale of polymer stent as coronary stents: the lack of radiopacity, which induces the application of radiopaque marks (such as gold implantation) on the surface of the stent and the reduced mechanical strength, when compared to stainless steel AISI 316L, requiring thicker structures [27]. Compared to polymer biodegradable stents, the metallic biodegradable stent possess the advantage of offering higher mechanical performance and are, therefore, more suited to withstand the pressure exerted by the vessel wall of the artery.

The first biodegradable metallic stent was made of iron (Fe> 99.8 %) and implanted in 2001 into the descending aorta of rabbits. Iron is a material well accepted by the human body, as it is an element found in many parts of the body, especially associated with hemoglobin in the bloodstream; it is also an interesting candidate for the realization of biodegradable metal stent from the point of view of its mechanical characteristics. Iron has a high radial stiffness, due to its high elastic modulus of 190 GPa, a feature that allows realizing the stent with fine mesh [28].

The results of the installation of the first biodegradable iron stent showed no significant evidence of inflammatory response and neointimal hyperplasia and did not reveal any signs of toxicity, local and / or systemic due to degradation products [28]. However, as demonstrated by in vivo studies that followed, iron degrades too slowly in biological fluids (after 18 months of implant, shows no signs morphological and / or mechanical failures due to degradation). In addition being a ferromagnetic material iron impedes the use of nuclear magnetic resonance (NMR) technique as a diagnostic imaging.

2.2. Magnesium Alloys

2.2.1. Introduction

Although magnesium (Mg) was produced only in 1808, it took about a century to develop a significant demand for it. Applications for magnesium as a structural material were, at the time, very few. The major part of the production was used as an alloying element for aluminium alloys and yet a smaller part were used in deoxidation process of steel, chemical and pyrotechnics and other minor uses [29].

During the Second World War (WWII), the production of magnesium as structural material rose, achieving 228.000 ton per year in 1944. The most part of this production was used for aircraft parts. After WWII, it had been attempts to use magnesium to peacetime applications, but failed in most part. The most known and successful was the Volkswagen Beetle, which carried more than 20 kg of magnesium. It used large magnesium alloy die castings for the transmission housing, the crankcase and a high number of small parts [29]. Although magnesium is a very promising material for many applications since is considerable lighter than aluminium, but it is also a very challenge material. What makes magnesium hard to use in a higher scale are: the high cost of production, not as workable as aluminium, not many developed alloys, no recycling procedure and specially the issues about the corrosion and safety of it. For those reasons, magnesium took some time to pass from the top-notch engineering for military application to daily civilian uses.

However, more than 4 decades later, the renewed interest in produce magnesium alloys rose, driven by the automobile, household and sport industry. In all cases, the main point was again to take advantage of its low weight. With the technologies more stable and the requirement of reducing the weight of some products the huge automotive industry entered on the game. Once the automotive industry, embraces the use of magnesium, it will become very economically interest for many other fields [30].

Recently magnesium has also being proposed as a biomaterial. Some of its characteristics, as the weight, the young modulus, and tensile strength are very similar to a cortical bone, for instance. The characteristic, however, that make magnesium a special candidate to biomaterial is that the products of corrosion are harmless, and in some cases even necessary to the human body. Therefore, instead of having this as a downside, the researchers have proposed a different approach. Instead of fighting against the corrosion, to let the material be absorbed by the body, while the body itself reconstruct the bone for example, in other applications, as for cardiovascular stents, the magnesium will be only present as a structural material as long as is necessary for the vessel to gain enough strength, and then the magnesium can be absorbed by the body.

2.2.2. Magnesium Properties

Magnesium, is an alkaline metal with atomic number 12, atomic weight 24.3050, the atomic diameter is 0.320 nm and in the solid metallic state presents a hexagonal close structure as in the Fig. 2.4. Its lattice parameters at room temperature are a=0.3209 and c=0.5210 resulting in a c/a ratio of 1.6236 which is very close to the ideal value of hexagonal close which is 1.633. Thus, magnesium may be considered a perfect hexagonal close material [29].

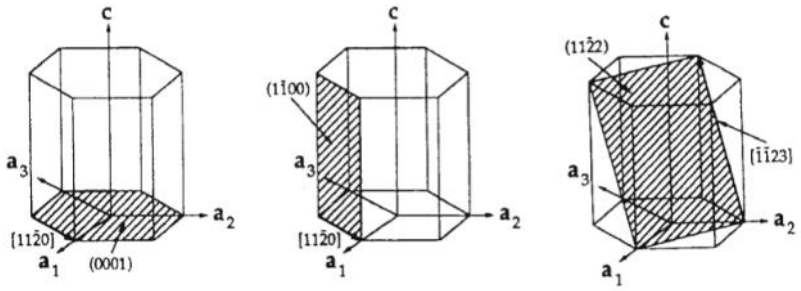

Fig. 2.4 - Magnesium unit cell and major planes and directions.

Regarding the physical metallurgy, magnesium alloys show a favourable trend towards packaging with other atoms favouring the formation of solid solutions, since the magnesium atomic diameter is of the order of 0.320 nm, enabling dissolution of the alloying elements atoms [31].

Magnesium alloys have a high thermal conductivity, high diffusivity and a relatively high electrical conductivity, important when the ground is required, and they are also ferromagnetic, which make them ideal for use in parts requiring a blockage against electromagnetic fields [29].

At room temperature, magnesium alloys have a modulus of elasticity (E) of 45 GPa, a shear modulus of 16.5 GPa and Poisson's ratio of 0.35. Due to the lack of slip planes on the crystal structure of Mg, at room temperature it presents a low tolerance to plastic deformation, usually presenting brittle behaviour. This does not occur on higher temperatures, allowing the material to be processed by many techniques such as hot extrusion, forging and rolling [32].

Magnesium has sufficient hardness for some structural applications, except those involving severe abrasion. Although there is a wide variation in hardness among the magnesium alloy, its abrasion resistance only varies up to 20% [29].

Another important feature for magnesium alloys is its excellent damping capacity compared to other metals. The damping capacity can be an interesting property in the selection of raw materials for the aircraft industry as well as for electronic equipment parts [29].

2.2.3. Magnesium Alloys

Due to the mechanical limitations of pure magnesium, it must be alloyed with other metals in order to have a real importance on engineering application. The process to develop alloys based on the application, e.g., biomaterials is quite similar to those used for FCC and BCC metals. The first thing to do when choosing the alloying element is to find another metal that has an appropriate atomic size to the magnesium structure. Although there are about 25 metals fulfilling this parameter, only few of them are appropriate alloying elements. The solubility is frequently limited by the relative valence

effect and due the chemical affinity with tin and silicon, which causes the formation of stable compounds [30].

Therefore, about ten elements can be considered as an alloying element for magnesium. Most of them can modify only ductility, elastic properties and hardness, without changing the elastic constant.

The formation of intermetallics reduces the ductility and frequently limits the application of the alloys to casting process. Despite that, these intermetallics showed to improve creep resistance, if the precipitates are formed with right size and distribution.

Aluminium is the main alloying element for magnesium alloys; it increases the workability, mechanical strength and ductility at room temperature. The aluminium also has a role to increase corrosion resistance of the Mg alloy [30]. The commercial Mg alloys have between 2 and 11% of aluminium [33].

Manganese is added to the alloy to help increase the corrosion resistance. Because it has high affinity with iron, removing the available iron, which is strongly related to the corrosion induction [33].

Zinc improves the room temperature strength by solid solution strengthening, also elevates the fluidity, ductility and elongation [30].

Calcium is a cheap alternative to develop creep resistance alloys, essentially replacing the $Mg_{17}Al_{12}$ with $Al_{12}Ca$. In addition, calcium can act as deoxidant [29].

Lithium is the only element that can reduce the density of magnesium alloys. It can increase ductility, but reduces the strength of the alloy [33].

Rare earths are commonly used to produce magnesium alloys to improve high temperature strength and creep resistance [31].

Zirconium is used as a grain refinement agent in alloys containing zinc and rare earths, but not with aluminium or manganese, since they form a stable compound with zirconium [33].

2.2.4. AZ91 Alloy

AZ91 Mg alloy is being proposed as a biomaterial, within an area where high purity alloys are needed, and AZ91 is one of the first high purity alloys on the market. It is one of the most common alloys, due to its broad use in the aerospace industry and it is finding its place on automotive industry as well.

AZ91 alloy is composed of 9% aluminium, 1% of zinc and residual percentage of silicon, nickel, manganese, iron and cupper, and of course predominated by magnesium. According to the phase diagram (Fig. 2.5), it presents two microstructural phases: the matrix α-Mg and the intermetallic phase γ ($Mg_{17}Al_{12}$).

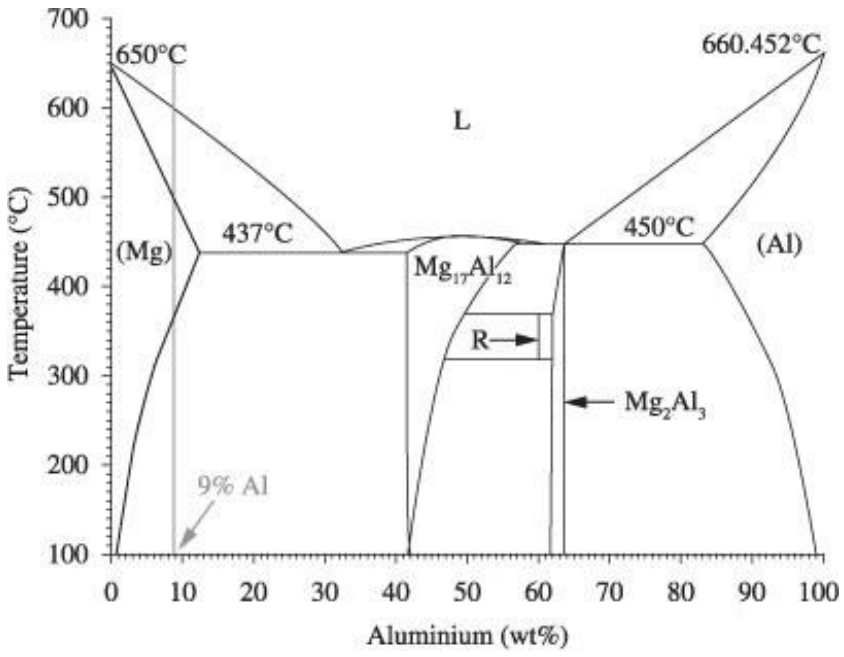

Fig. 2.5 - Phase diagram of Mg-Al.

Magnesium alloys are susceptible to solid solution strengthening, cold hardening, grain refinement and precipitation [34]. Among the alloy elements used on magnesium alloys, the most common are aluminium, zinc, zirconium, manganese, rare earth silver. These elements are in magnesium in order to improve mechanical and corrosion properties.

Most of commercial alloys are stable at room temperature and present good combination of mechanical properties, corrosion resistance and melting. However, temperatures above 373K (120°C) they usually presents low creep resistance and decrease its mechanical properties [35].

On AZ91 alloys, aluminium and magnesium form the intermetallic phase $Mg_{17}Al_{12}$, called γ-phase (sometime in literature it is also called β phase). The structure of γ-phase is body centred cubic (BCC), the unit cell contains 34 atoms of Mg and 24 atoms of aluminium, as can be seen on Fig. 2.6. The BCC structure is completely incompatible with the hexagonal close-packed (HCP) of the matrix. This incompatibility can induce high brittleness on the interface between the two phases, and if the γ-phase is not well controlled, the presence of such phase can harm the mechanical properties of the AZ91 severely. Beside the incompatibility, the γ-phase itself is quite brittle and can induce some micro-cracks into the material. The volume and morphology of γ-phase can strongly influence on the mechanical properties [36].

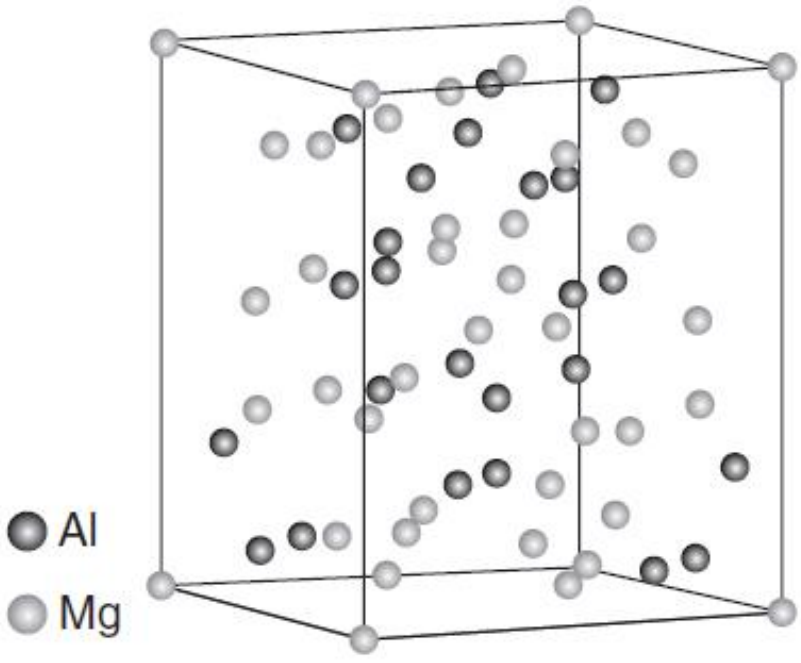

Fig. 2.6 - Atomic structure of $Mg_{17}Al_{12}$ intermetallic phase.

In non-equilibrium solidification, the matrix becomes supersaturated with Al, in particular in the interdendritic regions which give rise to the discontinuous precipitation of $Mg_{17}Al_{12}$ (Fig 2.7), especially when exposed to process

requiring elevated temperatures and pressure, such as sintering and extrusion. In order to decrease the harming effect of the precipitation of γ-phase, the alloys can be heat-treated by dissolving the γ-phase through solution treatment and further precipitation as a plate-like phase, which is considerably less harmful for the material properties.

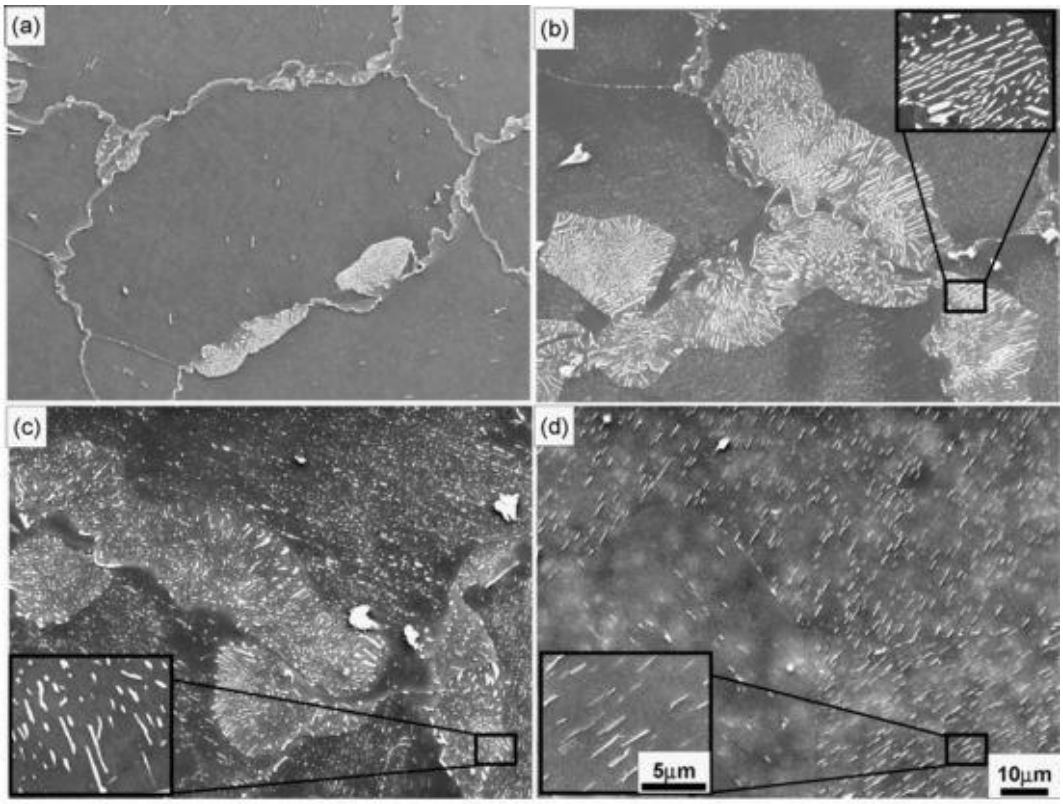

Fig. 2.7 - Typical microstructures of (a) AZ91 homogenized at 415 °C for 24h and AZ91 just after heating to compression temperatures of (b) 300 °C, (c) 350 °C and (d) 400 °C and soaking for 5 min [37].

The γ-phase strengthens Mg–Al alloys and specially AZ91. The γ-phase increases the strength by creating obstacles to slip and accumulating dislocation pile-ups at its interface up to a certain level of strain (2.1%); however, further strain (5.4%) does not change the dislocation pile-up, but instead leads to dislocation accumulation inside the γ-phase [29]. The γ-phase softens at elevated temperatures, due to its partial metallic bonding, which adversely affects elevated temperature strength and creep resistance. Its discontinuous precipitation from the supersaturated Mg matrix during creep leads to grain boundary deformation and migration. Many alloys have been developed to improve the creep resistance by adding Ca, Sr and REs to Mg–Al alloys to eliminate the discontinuous precipitation of $Mg_{17}Al_{12}$ [38].

2.2.5. Magnesium as a biomaterial

Biodegradable implants objective is to provide a temporary (mechanical) support while the injured tissue heals. Once the tissue is completely healed, the substitutive material should gradually degrade and further disappear, leaving a fully recovered tissue, as if there was nothing before there.

Nowadays, the biodegradable materials are, in most part, based on polymers, ceramics or organic materials. These types of materials are not known for its high mechanical performance, at least not such as metallic materials, which can deliver higher performance regarding especially mechanical properties. Thus, the idea of producing biodegradable implants based in metals, as magnesium, shows very promising.

Metals were used as biomaterials for the first time by the Romans, who used metal clips for skin adaptation [39]. Some metals were also used at the beginning of osteosynthesis such as silver, copper, lead, iron, gold and platinum. Nevertheless, these metals were rejected on the surgical use for several reasons. Gold and platinum despite the excellent corrosion resistance properties, are very expensive and does not show high mechanical resistance. Lead showed to be toxic. Silver and iron are still considered suitable biomaterials. For osteosynthesis, pure silver suffered from the mechanical point of view, even if its antibacterial effect is appreciated up to date. The use of iron as a biomaterial decrease since metallosis was observed after iron implants [40]. Metallosis is a deposition of metal into the soft tissues from abrasion with metallic components, leading to the tissue death [41]. These clinical observations led to the paradigm that metal implants should be necessarily corrosion resistant.

In recent years, many studies broke this paradigm by applying some metals in the development of medical products. Especially magnesium and iron-based materials has been proposed as temporary biomaterials which degrade in vivo by corrosion [2], [27], [42–45].

The basic concept of biodegradable metals is to compose the metals of elements which can be cleared from the body by physiological pathways and which do not exceed the toxicity limits during the corrosion process [39].

As shown in Table 2.2, several magnesium alloys have been studied as biomaterials. AZ31 and AZ91 enhanced the osteogenesis response and increase newly formed bone [42]. The AE21 was capable of gradually degrade in a pig artery and is a promising cardiovascular implant material [45].

Table 2.2 - Some magnesium alloys studied as a biomaterial [7].

Alloy type	Aluminum (wt.%)	Rare earth element	Zinc (wt.%)	Other
AE21	2	1 wt.% (Ce, Pr, Nd)		
AZ31	3		1	
AZ91	9		1	
WE43		3 wt.% (Nd, Ce, Dy), 4 wt.% (Y)		
LAE442	4	2 wt.% (Ce, La, Nd, Pr)		4 wt.% Li
AM60B	6		0.07	0.33 wt.% Mn
Mg–Ca				<2 wt.% Ca
Mg–Zn–Y		~0.36–1.54 wt.% Y	2	
Mg–Mn–Zn			1	1.2 wt.% Mn

2.2.6. Magnesium as a material for cardiovascular applications

The first application of cardiovascular magnesium dates back to 1878, when Edward C. Huse used a suture in Mg to stop arterial bleeding. Subsequently, the magnesium has been used in other applications such as cardiovascular biodegradable material for suture threads, connectors for vascular anastomosis and wires for treatment of aneurysms [28].

Magnesium is a promising material for the realization of biodegradable installations, due to its well-known biocompatibility. It is very abundant in human body and is essential for the life of the organism. It has a lower density than other metal materials (ρ = 1738 kg/m^3), an elastic modulus of about E = 11.7 -18.2 GPa, thus presenting better physical and mechanical properties when compared to polymeric materials proposed for the manufacturing of biodegradable stents.

Magnesium and its alloys corrode in aqueous solutions for pH values less than 11, and thus, in physiological conditions, these materials degrade according to the following reactions [46]:

$$Mg \rightarrow Mg^{2+} + 2e^{-} \quad (1)$$

$$2H_2O + 2e^{-} \rightarrow H_2 + 2OH^{-} \quad (2)$$

$$Mg(s) + 2H_2O(g) \rightarrow Mg(OH)_2(aq) + H_2(g) \quad (3)$$

The layer of magnesium hydroxide, which is formed on the surface of the material offers a weak protection and behaves as a passivation film in pure water. However, in aggressive environments containing chlorides, such as biological fluids, the film is destroyed and continued corrosion with formation of soluble compounds of magnesium is observed:

$$Mg(OH)_2 + 2Cl^{-} \rightarrow MgCl_2 + 2OH^{-} \quad (4)$$

The development of hydrogen gas (following reaction (3)) and the presence of a strongly alkaline environment represent a significant risk to the health of the patient, as they represent non-physiological conditions [46].

It has been proposed both pure magnesium and some alloys for the production of biodegradable stents [27], [28]. The first in vivo study in 20 patients with severe ischemia of the lower limbs treated with biodegradable stents made with magnesium alloy WE43 (3.7-4.3% Y, 2.4-4.4% rare earths, 0.4% Zr) was published in 2005 by Peeters et al. [47]. The results of this study have shown the potential of magnesium for the realization of biodegradable metal stent, since there was not observed toxicity or allergic reactions.

However, early studies on the kinetics of corrosion of the magnesium alloys in physiological environment have shown that the main limitation of these alloys for the construction of stents is their excessive degradation rate inside the human body (to pH 7.4-7.6), as the times of degradation of the device are not comparable with the healing time of the vessel. Currently, the lifespan of a magnesium stent in physiological environment is of the order of 2-3 months,

while the function of mechanical support of a stent is requested for a period of the order of 6-12 months after the implant.

The rapid degradation of the installations in magnesium can lead to loss of mechanical integrity in a short period [28]. One of the critical issues to be improved in order to achieve superior performance of biodegradable stents made of magnesium, therefore, is the slowing down of the kinetics of corrosion, in order to extend the period of time during which the action of mechanical support of the stent is effectively exercised.

Some strategies to improve the corrosion resistance and slow down the corrosion rate, by changing the composition of the alloy, making changes surface by introducing polymer coatings or change the design of the stent. In addition, among the factors relevant to the performance of the stent, the fabrication route plays a fundamental role, since the grain size, the mechanical properties and the absence of structural defects depend greatly from it. It has been shown in some studies [48], [49] that the rate of degradation decreases with decreasing grain size, in particular for the pure Mg [48] and for the aluminium-zinc alloys (such as AZ91) [49].

The hot extrusion is the most commonly process used for the production of the tubular stent precursor. The extruded tubes are then laser cut and then subjected to a chemical etching. This treatment in the process of production of the stent is intended to remove the burr around the cutting groove and the roughness on the surface of the metal, due to the process of laser machining (Figure 2.8) [50].

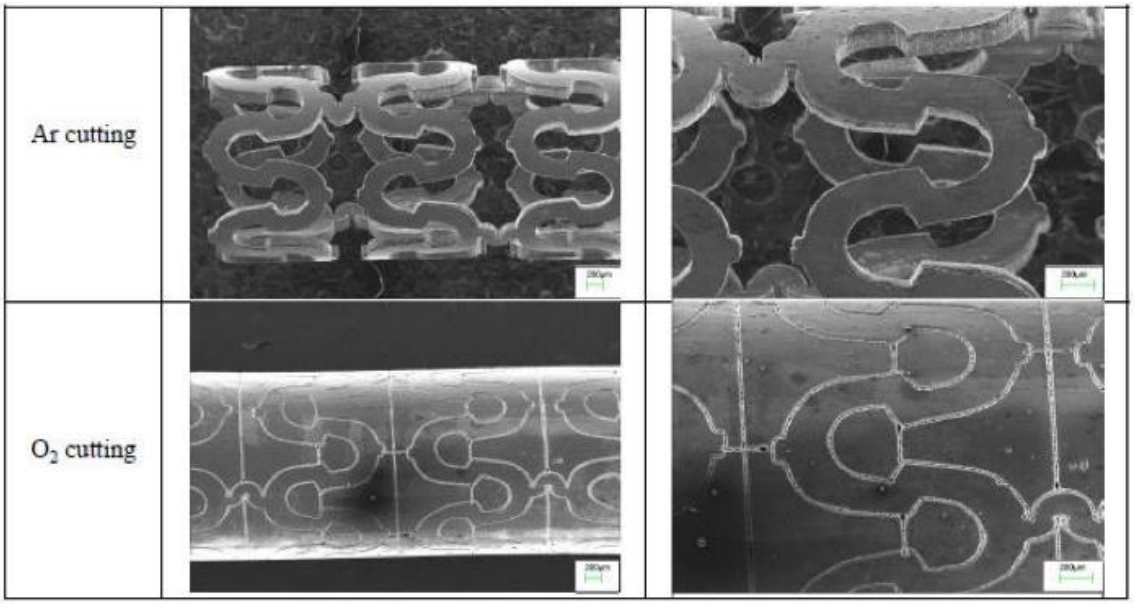

Fig. 2.8: SEM Images of AZ31 stent subjected to laser cutting [50].

A recent study performed by Farè et al. [51] showed that the magnesium alloys corrode in the physiological environment at a rate that is too high for its use as a structural material for biodegradable implants. The addition of alloying elements can slow down the corrosion rate of magnesium alloys, but the elements added to develop alloys with better characteristics compared to pure Mg are limited to just a few metals, known to be tolerated in the human body, such as calcium, zinc, manganese and a small percentage of rare earths. However, the corrosion resistance of magnesium alloys is still not sufficient to meet the clinical requirements [52], being necessary to improve the microstructure and coat the stent with a biodegradable polymeric material.

Chapter III

Fabrication Route

3.1. Introduction

Usually, magnesium alloys are produced by casting technologies and then submitted to hot working processes. The Powder Metallurgy (PM) route is not largely used for Mg alloys because the powders display a high reactivity to oxygen and thus, easily form oxides on their surfaces, which render quite difficult the sintering process [3]. However, for biodegradable stents, very small grain size is required, in first place because it enhance the mechanical properties [4–6], and also to optimise corrosion behaviour [1,7], therefore, the choice to choose the powder metallurgy (PM) techniques is to start with a small grain and try to reduce it through extrusion. Other advantage of using PM is to allow the better control of the alloy composition, in view of further developments. Showing that using PM a stent can be produces, open a wide field of research to develop new alloys that can improve the final product.

Within the PM technologies, spark plasma sintering (SPS) showed to be highly effective in promoting a good densification of Mg powders. After producing the SPS samples, the tube extrusion will be performed to produce tubes, which are going to be machine and further laser cut, obtaining the final stent. Therefore, the fabrication route is according to the following scheme:

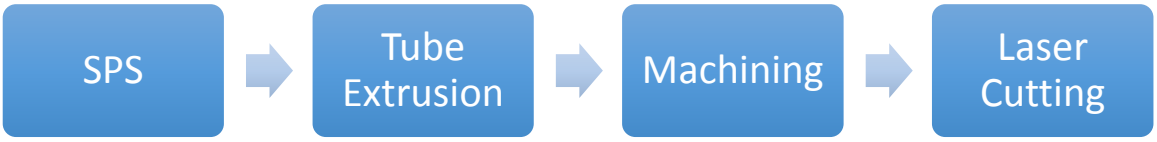

3.2. Spark Plasma Sintering (SPS)

Spark plasma sintering (SPS), or also called “pulse electric current sintering”, a sintering technique quite similar to the hot pressing sintering,

where a uniaxial pressure is applied over the powder to induce the sintering. The difference lays on the many advantages that the SPS technique has to offer, such as the reduced sintering time from hours to minutes. In addition, many materials that require high temperatures to be sintered in conventional process can be more easily processed using the SPS, such as titanium alloys and tungsten carbide. Bringing down both time and temperature of sintering is even possible to achieve nanoscale microstructure and thus increasing highly some properties. Fig. 3.1 shows the main components of a SPS unit.

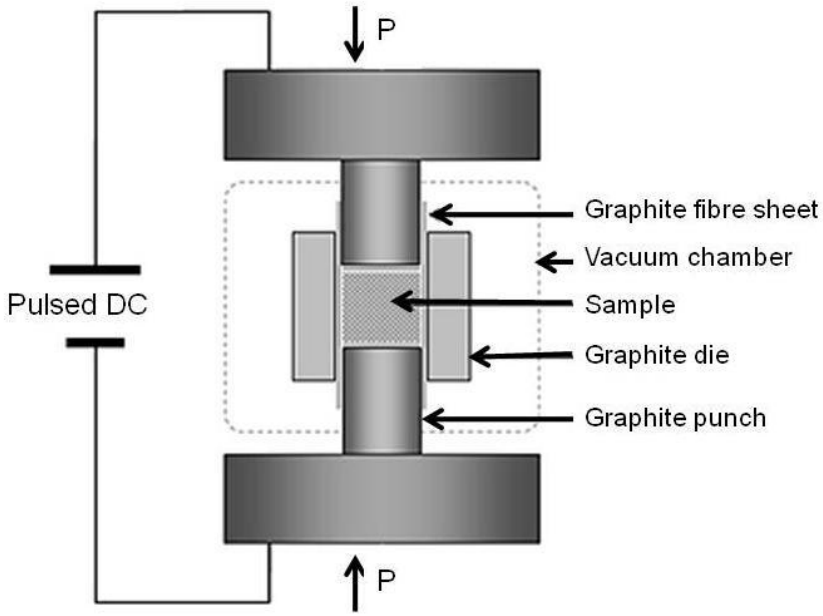

Fig. 3.1 – Main components of a SPS unit.

SPS is quite similar to “hot press sintering”, in which a pressure is applied to the powder and together with the heating, it induces the sintering processes. The main aspect which differentiate SPS from others process, is the pulse direct current flowing through the material and the die. When the neck is formed between conductive particles, the local resistivity decreases rapidly and a high current flow in the neck, generating a local heating through the Joule effect. After the local heating, the resistivity tends to revert and rise, inducing the current to other part of the material, forming other necks. This mechanism allows the material to have a uniform sintering. Fig. 3.2 illustrates the current flow through the particle.

Therefore, the fast densification process is given mainly by the use of high pressure, an equal and efficient heat transfer, the presence of local discharges generated between the particle boundaries and the presence of the electric field.

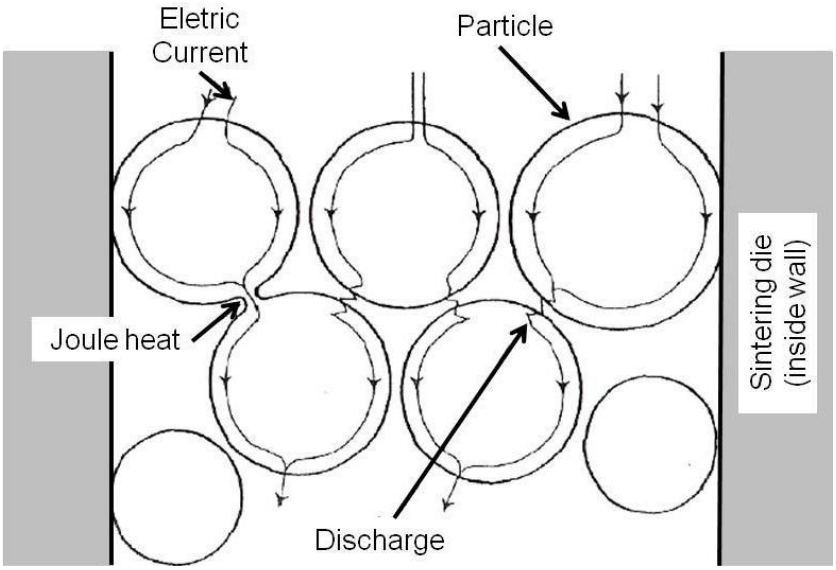

Fig. 3.2 - Current flow through the powders particle.

For non-conductive materials, the die and the punches are heated first, and heat is transferred to the sample. As the temperature of the sample increases and with the application of the DC current, the thermal and electrical breakdown phenomena are most likely to occur and the current may flow even in non-conductive materials.

Some materials, such as aluminium and magnesium alloys form a passive oxide layer on the particle surface. Therefore, they are very hard to sinter. However, with the SPS process, these oxides can be broke down by the discharges present on the SPS, helping to form and grow the neck, allowing the sintering process to occur [3], [8]. The role of the pressing is to induce the mass transport through plastic flow and creep.

SPS for structural magnesium alloys it was not widely researched, in literature is possible to find some paper on the subject. Kim et al. showed that is possible to consolidate Mg-Zn alloys powder through SPS [53]. Three different particle sizes were compared (33 µm, 46-63 µm and 46-90 µm) and

after, the preforms were extruded. The size of the original powder does not showed significant changes on the final microstructure and mechanical properties of the extruded part.

Lee et al. was also capable of consolidate the powder through SPS of gas-atomized powders [54]. Ultimate tensile strength and elongation to failure were in the range of 280 and 293 MPa and 8.5 to 20.8% respectively, which showed to be dependent in the SPS temperature.

3.3. Extrusion

Extrusion is plastic a deformation process used to produce long, straight, semi-finished metal product such as bars, solid and hollow sections, tubes, wires and strips. The concept is quite simple: a billet is forced by a high load to flow from a closed container through a die in order to modify its shape or size. Extrusion can be performed at room temperature or at high temperature, depending on the material and the desired properties after the process [55].

The extrusion ratio, R, is defined as the ratio of the initial area of the billet (A_o) and the final area of the extruded part (A_f). For Al alloys, R can reach values up to 400, whereas for Mg the values of R can reach 100, depending from the temperature. The strain is given by:

$$\varepsilon = \varepsilon_1 = ln\frac{A_0}{A_f} = ln\frac{L_f}{L_0} = \ln R \quad (5)$$

where L_o is the initial length of the billet and L_f is the length of the extruded part. Strain is, generally, in the range 2-5. Since the speed of the piston may vary in the range of 0.1-1 m/s, the strain rate is typically in the range of 10^{-1} - 10^{2} s^{-1}. The extrusion is performed by means of hydraulic presses with a capacity typically between 50 and 200 MN.

Fig. 3.3 shows schematically the typical characteristics of plastic flow that can take place during extrusion of a billet to obtain a round bar. The angle of semi-opening of the matrix is indicated by α and the angle of extrusion is

indicated by α_s. The plastic flow is evidenced by the method of the grids. In Fig. 3.3a, α = 90 ° it is observed an accumulation of metal with the formation of the dead zone and the angle of the extrusion is formed spontaneously. With good lubrication, $\alpha_s \approx 70$ °, while in the absence of lubrication, α_s can be estimated by the following experimental relation: $\alpha = 54 + 3.45 \ln R$. Conical matrices (Figures 3.3 b and c) are generally used in the presence of good lubrication. As can be seen, if α is high, the plastic flow is very heterogeneous with a significant presence of plastic deformation by shear. At the decrease of α, the plastic deformation becomes more homogeneous, but increases the contribution of the friction due to the sliding between the metal and the surface of the matrix.

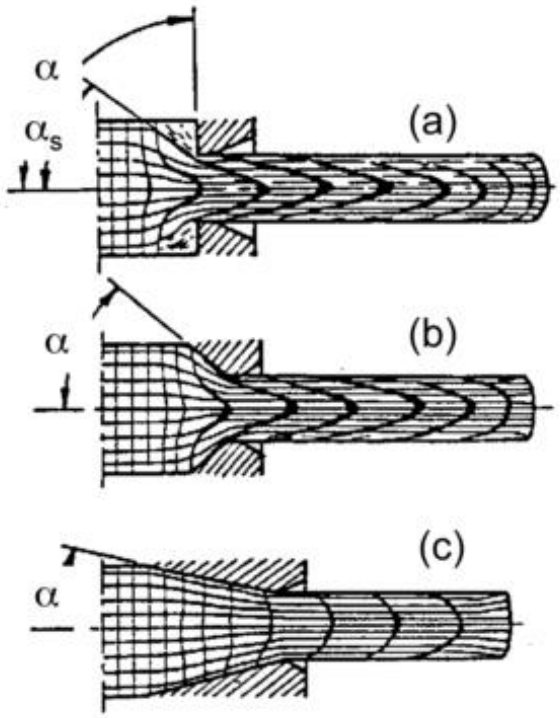

Fig. 3.3– Schematic representation of the typical characteristics of plastic flow that can take place during extrusion of a billet to obtain a round bar.

To calculate the pressure, p_o, which the plunger applies during the extrusion of a bar, it is necessary to neglect initially the friction in the metal-matrix surface and in the bar-container surface. Considering also that the plastic deformation, which lead a bar with length L_o and area A_o into a final bar with length L_f and area A_f, is uniaxial. Being $\overline{\sigma}$ the average Yield strength, is

obtained that the work for plastic deformation is $\overline{\sigma} \cdot \varepsilon \cdot \mathrm{L}_o \cdot A_o$. It is also known that the total work during the extrusion process is also equal to $\mathrm{p}_o \cdot \mathrm{L}_o \cdot A_o$, then [56]:

$$p_o = \overline{\sigma} \cdot \varepsilon = \overline{\sigma} \cdot \ln R \tag{6}$$

Nevertheless, since the plastic deformation during the extrusion is not uniaxial, as we considered before, the relationship need to be adjusted with a factor ß. Then:

$$p_o = \overline{\sigma} \cdot \varepsilon = \beta \cdot \overline{\sigma} \cdot \ln R \tag{7}$$

For a symmetric cylindrical bar being extruded through a 90º matrix, it is obtained that ß is equal to 1.34. For more complex shapes is possible to estimate the pressure by substituting R for R' as follows

$$R' = R \cdot \sqrt{\frac{p_e}{p_b}} \tag{8}$$

Being p_e the external perimeter plus the inner perimeter of an extruded section and p_b the circumference of a bar equivalent to the extruded section.

Another relationship that takes into account the friction between the metal and the matrix is the following:

$$p_o = \overline{\sigma} \cdot (a + b \ln R') \tag{9}$$

The values of a and b are 0.88 and 1.3 respectively for low friction, 0.9 and 1.5 respectively for intermediate friction and 1.06 and 1.55 for high friction.

To evaluate the influence of the friction on the plunger pressure it is necessary to consider the role of the friction between the bar and the container and between the metal and the matrix. Being p_μ the contribution of the friction on the total pressure and p_{ext} the pressure that the plunger applies during extrusion, is obtained that [56]:

$$p_{ext} = p_o + p_\mu = p_o + p_o \frac{4\mu L}{D_o} = p_o \left(1 + \frac{4\mu L}{D_o}\right) \tag{10}$$

where L is the instant length of the plunger into the die, D_o is the inner diameter of the die and μ the coefficient of friction.

In the case of hot extrusion, to evaluate the force of extrusion, it is necessary to know the strain rate, $\dot{\varepsilon}$, and the temperature of the metal into the matrix. The average strain rate is given by:

$$\dot{\varepsilon} = \frac{\varepsilon}{t} = \varepsilon \frac{v_o}{L} \tag{11}$$

where t is the time that a slice of metal takes to enter and exit from the matrix, L is the length of the matrix and $v_o$is the speed of the metal into the die, which can be considered equal to the ram speed. To make it simple, using a bidimensional geometry for the extrusion, it is obtained that:

$$L = \frac{D_o - D_f}{2\, tg\alpha} \tag{12}$$

and then:

$$\dot{\varepsilon} = \frac{2 \cdot v_o \cdot tg\alpha}{D_o - D_f} \tag{13}$$

With analogous approach, in the case of an extrusion to obtain a rod with diameter D_f:

$$\dot{\varepsilon} = \frac{6 \cdot v_o \cdot D_o^2 \cdot tg\alpha}{D_o^3 - D_f^3} \cdot lnR \tag{14}$$

Extrusion is often used to induce a decrease in the grain size of magnesium alloys [4], [57]. Many factors influence on the final grain size of the material submitted to the extrusion. Fig. 3.4 [5], shows the influence of the extrusion ratio on the final grain size, as well as the difference of microstructure on the surface and in the centre of the extruded billet. As the extrusion rate increases, the grain size tends to become more rounded and more homogeneous, because of the dynamic recrystallization that occurs during extrusion.

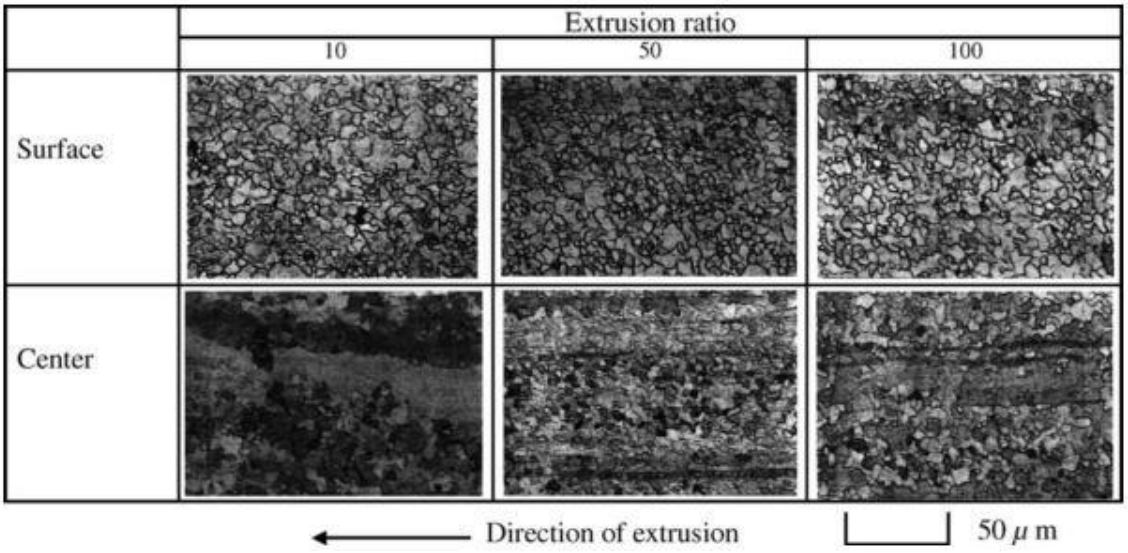

Fig. 3.4 - Microstructure of AZ31B Mg alloy extruded at different extrusion rates, in the centre and in the surface [5].

Lapovok et al. showed by finite element simulation that specially in extrusion with α=90°, there are significant changes on the local temperature, effective strain and strain rate [58]. These gradients may influence the homogenization of the microstructure, and can lead to differences between surface and centre shown in Fig. 3.4.

As the extrusion ratio increases, the risk of crack formation, especially in the surface, increases as well. Other parameters that influence directly the final properties are the temperature of extrusion and the ram speed. As the ram speed increases, the strain ratio also rises and this may favour the onset of dynamic recrystallization.

The process temperature must be optimized because a too low temperature may not provide enough energy to recrystallize the microstructure, leaving a highly flattened microstructure. On the other hand, a too high temperature can easily make the grains grow rapidly just before and after the extrusion, inducing the formation of large grains. Fig. 3.5 shows the influence of the extrusion temperature on the final grain size of the AZ91 alloy after extrusion [59].

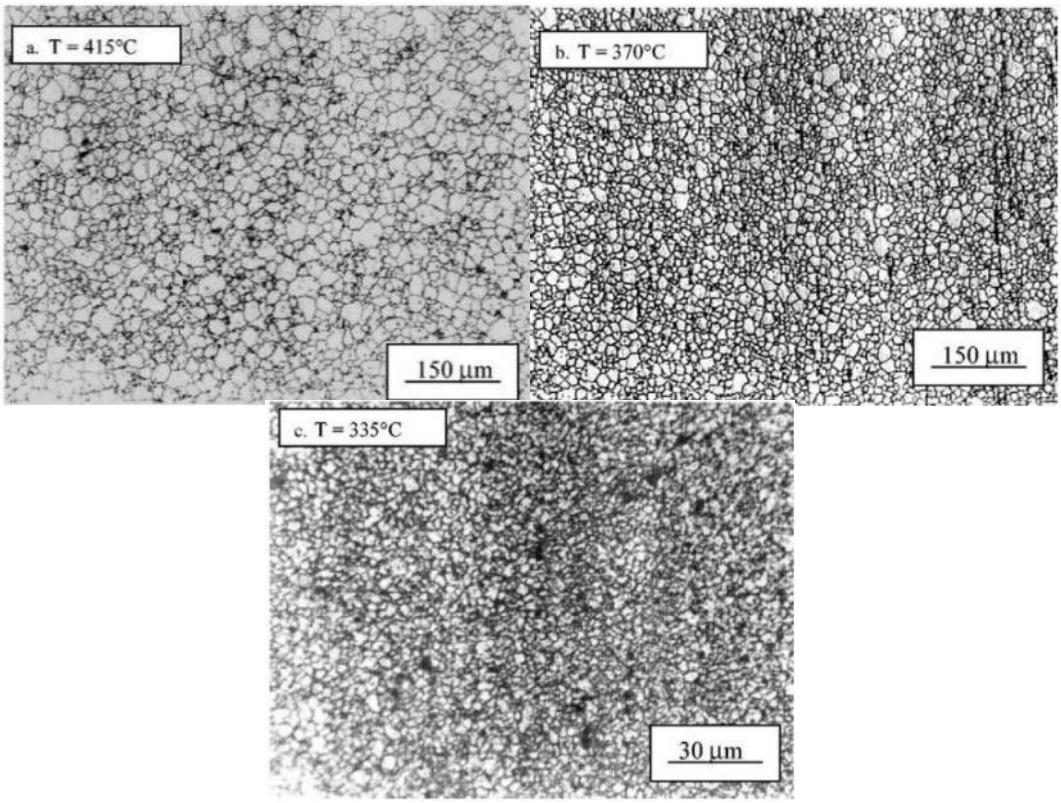

Fig. 3.5 – Influence of the extrusion temperature on the grain size on AZ91 Mg alloy [59].

The grain size is connected with mechanical behaviour of magnesium alloys according to the Hall-Petch equation as follows:

$$\sigma_y = \sigma_o + kd^{-1/2} \tag{15}$$

Where σ_y is the yield stress, σ_o is a materials constant, k is the strengthening coefficient, which is typically a constant for each material, and d is the average grain size. Fig. 3.6 shows that after hot extrusion, the mechanical properties followed the Hall-Petch relationship for both Yield strength and elongation [60]. Since all elongation, yield strength and usually ultimate strength are correlated, all can follow the Hall-Petch equation. The fitting of the following example is $\sigma_y = 165\ MPa + 14\ MPa.mm^{-1/2}\ d^{-1/2}$.

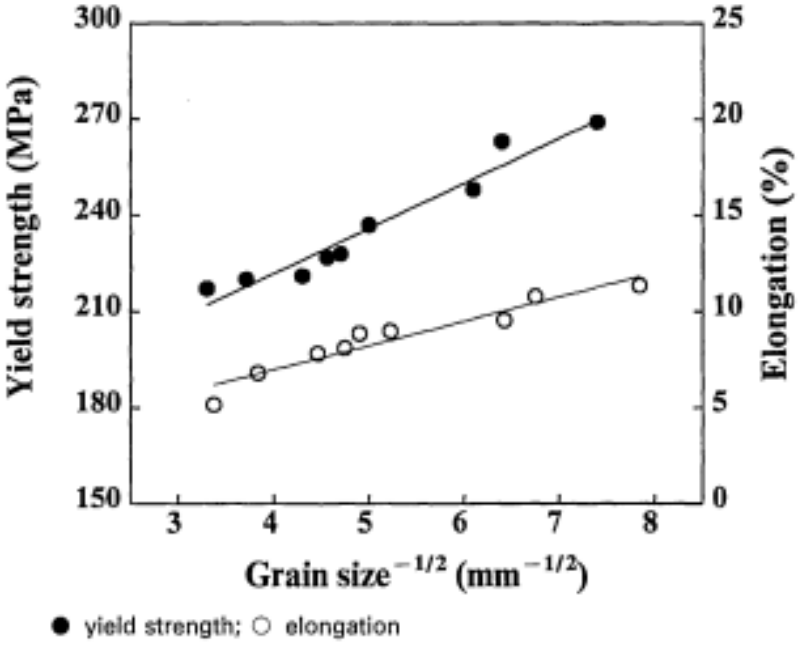

Fig. 3.6 – Yield strength and elongation of AZ91 as function of (grain size)$^{-1/2}$ [60].

3.4. Laser Cutting

Laser cutting is a technique very widely used to produce metallic stents. The main advantage is to be a noncontact cutting method, capable of cut very precise and complex shapes. Lasers can cut stents of a wide range of materials, such as stainless steel, Nitinol and magnesium alloys.

Laser cutting is often applied in two different ways: continuous wave (CW) or pulsed wave. The process of cutting with the CW lasers consists in locally melt the material, forming the kerf and with the action of the gas, expel the material from the kerf. This is called “melt and blow” technique and is very productive due to the fast heat penetration and comparatively lower temperatures required to melt the material. With the introduction of fibre laser sources [9], [10], [14], CW was widely accepted in industrial fabrication of metallic stents, However, it has been only studied on stainless steel.

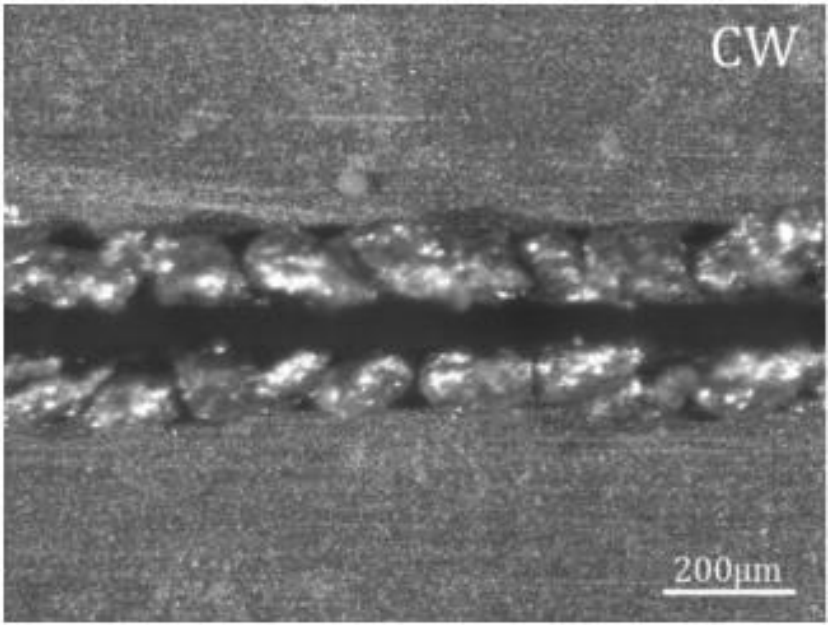

Fig. 3.7 – Detail of a CW cutting on AZ31 Mg alloy [11].

Alternatively, laser sources can run in pulsed wave, allowing the release of a pre-defined energy in short durations of time. The parameters that control the energy and the mechanism of material removal are the pulse duration and the shape of the wave. Despite the importance of these parameters in the result of the laser cutting, nowadays, the most part of industrial systems are not capable of regulating them, and when is possible to regulate, it is very limited.

This is because the choice of a laser source has a direct impact on the pulse duration. Thus, the pulse duration is limited by the laser source. This leads to a discussion about the proper laser source for each application. In the case of biomedical device production, the laser cutting must provide high productivity and good machining quality. The goal is to eliminate post processing after laser cutting.

The difference on the change of pulse duration lays in the interaction of the laser beam with the material and the consequences of duration of time that this occurs. By calling T_e the temperature of the electron and T_L the temperature of the lattice [61], [62], and assuming that the time to cool the electron is τ_e and the time to heat the lattice is τ_L, being $\tau_e << \tau_l$ [11].

For pulse duration (τ) lower than 100 fs (100 x 10^{-15}s), occurs the ablation phenomena in the cold state, since the interaction with the electrons and the lattice happens so fast that the bulk material is not affected by the heat induced by the laser beam. Therefore, it remains in the solid state, representing a situation where $\tau << \tau_e$.

If the pulse duration in the range of 100 fs (100 x 10^{-15} s) to about 10 ps (10 x 10^{-12} s), hot ablation occurs, because in this condition $\tau_e << \tau << \tau_L$, which means that the ablation still occurs by evaporation, and the temperature of the electron tends to approach the temperature of the lattice, but the thermal diffusivity of the lattice can be neglected when compared to the electron. Thus, the electrons are being heated, and are transferring this heat to the bulk material, but the time is not large enough to allow the lattice to heat as much as the electron. Surface evaporation remains as the main mechanism for material removal, however there are already some melting present, which can harm the quality of the cutting. As seen in Fig. 3.8, the presence of few molten particles is observed on short duration pulse.

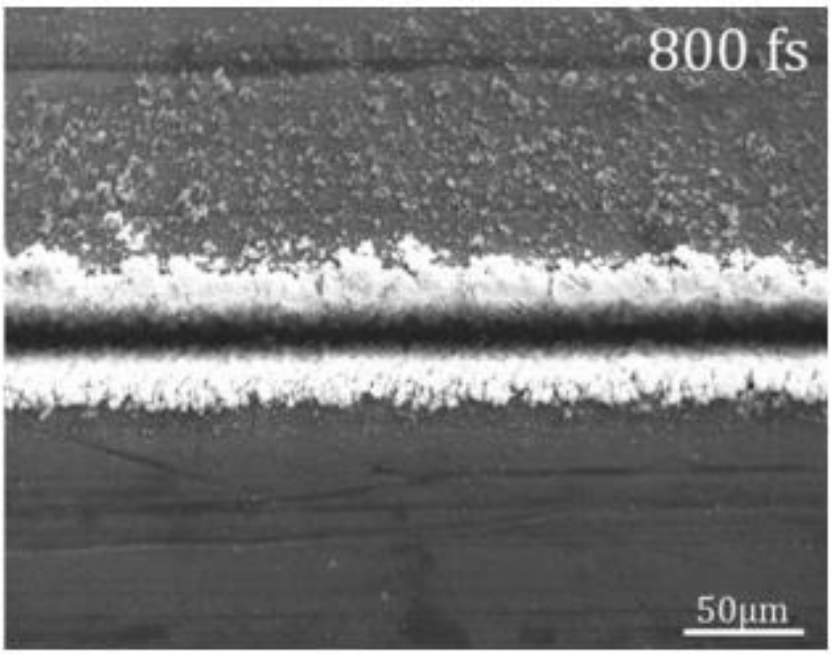

Fig. 3.8 – Detail of a laser cut performed with pulsed duration of 800 fs [11].

While for pulse duration above 10 ps (10 x 10^{-12} s), thermal equilibrium between lattice and electrons is reached and the laser energy dissipates into the bulk material because. Now the removal mechanism is a mixture of vaporization from condensed matter, vaporization from the molten phase and melt expulsion. If the molten phase is not removed during the process causes redeposition of material, creating a layer around the ablation area, which is highly damaging for the machining quality. These depositions are called dross. In Fig. 3.9 is possible to observe a laser cutting with long duration pulse, and the dross quantity is very high.

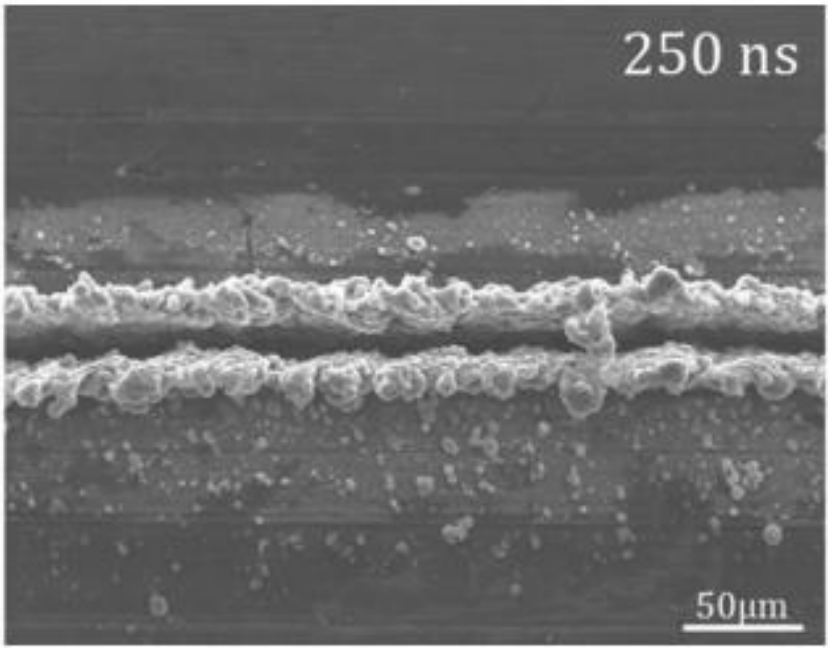

Fig. 3.9 – Detail of a laser cut performed with pulsed duration of 250 ns [11].

After analysing the impact of the pulse duration on the laser cutting, is possible to conclude that this is the parameter that rules the machining quality. Then, in the practice, different sources of laser implicates in different regimes: Long duration pulses (ms and µs), short duration pulses (ns) and ultra short duration pulses (ps and fs).

In literature it is possible to find only few studies related to micro-cutting of stents by CW emission [10], [11], long pulsed [9], [11–14], short pulsed [11], [15] and ultra-short pulsed [11] sources. Demir et al. showed the process of micro-cutting of stents of magnesium alloys. On Fig. 3.10 it is possible to

notice that even at ultra short pulse duration, post processing is required in order to achieve desires quality after laser cutting [11].

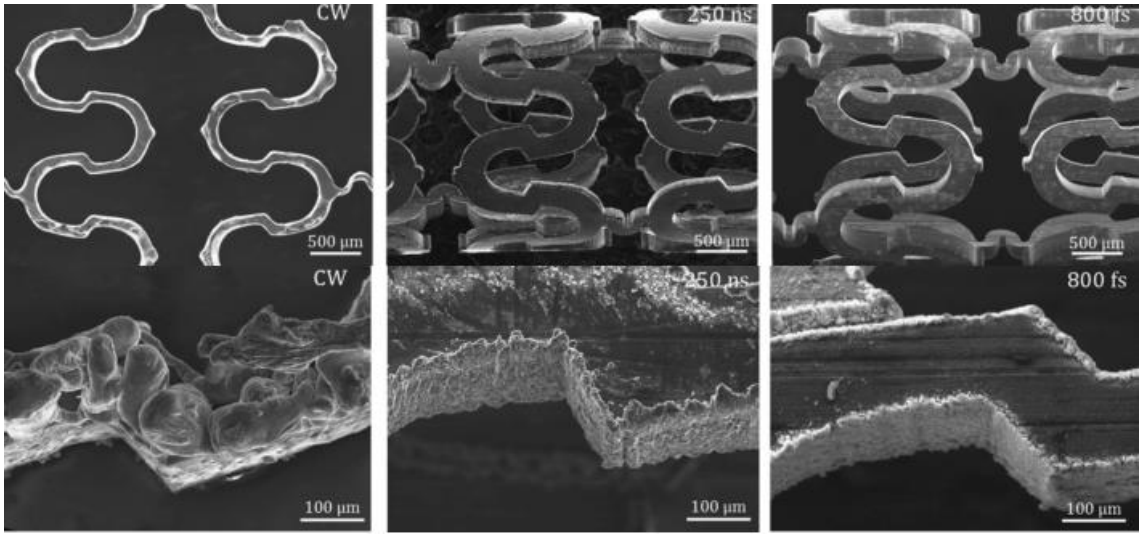

Fig. 3.10 – Stent cutting with CW, short pulse and ultra short pulse duration [11].

Chapter IV

Materials and Methods

4.1. Pure Mg and AZ91 Powder

Pure Mg (99,76 wt.%) powder was produced by chipping and milling by Whole Win (Beijing) Materials Sci. & Tech. Co., Ltd. with a particle size below 75 µm. The powders were regular in shape, but all of them with a thick MgO layer on their surfaces. Using a XRD analysis followed by a quantitative evaluation using the Rietveld method, it was determined that the total amount of MgO was 1%.

The AZ91 powders employed in the present investigation were produced by chipping and milling by Ecka Granules GmbH. The measured chemical composition of the powders is Mg-9.58%Al-0.65%Zn-0.22%Mn-0.029%Si (wt %). The starting powders were quite irregular in shape.

4.2. Spark Plasma Sintering

Spark Plasma Sintering process was carried in a Dr. Sinter SPS 1050 using graphite die and punches. The final samples were cylinders with a diameter of 10 mm and a height of 25 mm. For the AZ91 alloy, one optimized cycle including a homogenization stage has been studied before [3] It consist in heating the sample up to 420°C at a rate of 50 °C/min and holding at this temperature for 50 minutes. The purpose of this first step is to homogenize the material and not allow the formation of a liquid phase. After the homogenization, the powder was heated up to 470°C at the same heating rate and sintered for 10 minutes at this temperature with an applied pressure of 36 MPa. The Fig. 4.1 (a) shows the microstructure obtained by the long cycle.

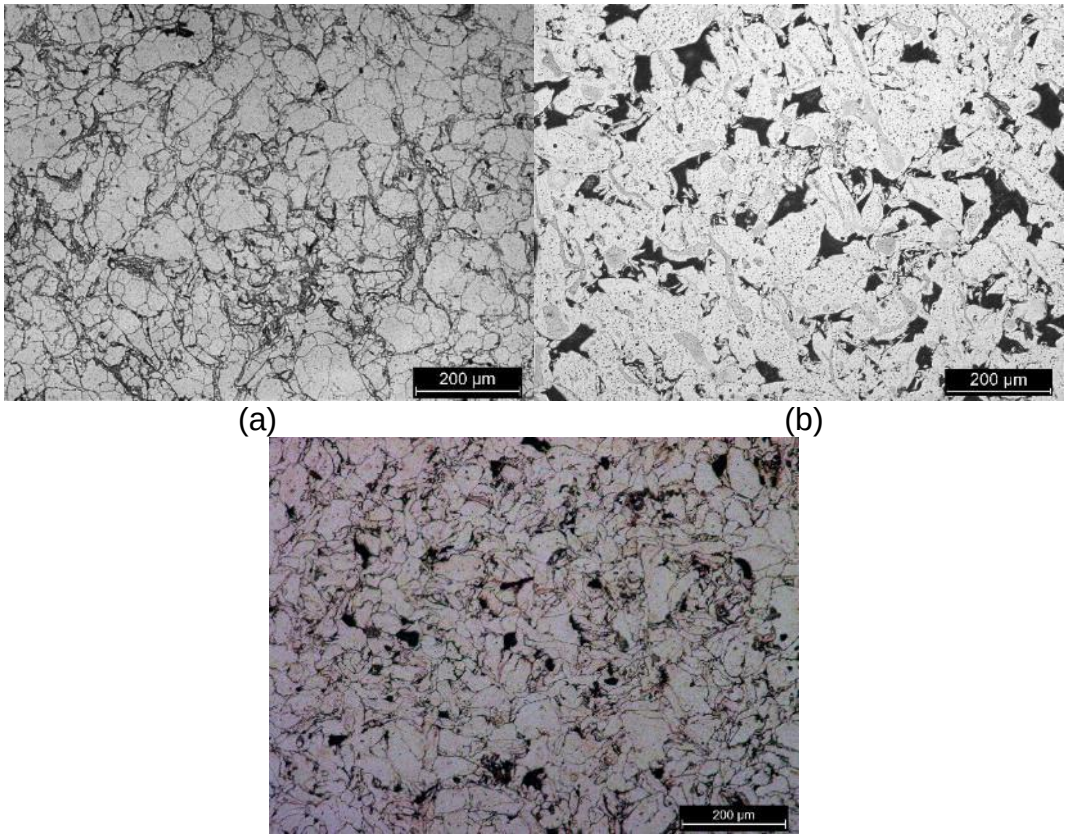

(a) (b)

(c)

Fig. 4.1 – Microstructure of (a) AZ91 long cycle (b) AZ91 short cycle and (c) pure Mg SPS.

Since this cycle take at least one hour to produce each sample, and that after going through the SPS process, the material will be submitted to hot extrusion, a second cycle was proposed in order to reduce the time and also to evaluate the influence of the sintering parameters on the final properties of the SPS preforms. The short cycle consisted in heat the sample up to 420°C at a rate of 50 °C/min and sintered at this temperature for 10 min, without any homogenization. For the Pure Mg powders, two temperatures were studies, 400 and 470 °C. The cycle consisted of heating the sample up to the sintering temperature with a heating rate of 100 °C/min and sintering at the same temperature for 1 minute.

4.3. Density

The density of the sintered samples was measured using the Archimedes principle, according to ASTM B962-08 standard.

For the determination of relative densities of composite materials, their theoretical density was calculated according to the rule of mixture:

$$\rho_{composite} = v_1 \cdot \rho_1 + v_2 \cdot \rho_2 \quad (16)$$

where v is the volume fraction and ρ is the absolute density of each component.

For AZ91, the theoretical absolute density used was 1.81 g/cm^3, and for pure Mg it was 1.74 g/cm^3.

4.4. Hot Compression

The hot compression tests were performed in order to investigate the hot deformation behaviour of the SPS specimen, simulating some aspects of the extrusion process. The extrusion machine had a limitation of 100 kN as a maximum force, and then the results of yield strength under hot compression were used in order to predict the extrusion force.

The hot compression tests were performed on a Bahr 805A/D dilatometer. The tests were carried out using cylindrical samples with a diameter of 2.5 mm and a height of 5 mm obtained by machining the SPS specimens. The samples were then cut in the same direction of pressing during sintering. The samples were submitted to the hot compression at 330 and 380 °C at a strain rate of 0.002 s^{-1}.

As known it is possible to link the between flow stress under hot compression to the extrusion behaviour of the material [59]. The aim of these calculations is to better understand the behaviour of the material under the extrusion process.

The extrusion pressure, p_o, is related to the flow stress through eq. (7) or alternatively, eq. (9). By applying the eq. (9) with the high friction constants, the extrusion pressure can be epressed as:

$$p_o = 3.90\,\sigma \quad (17)$$

As a consequence, the total extrusion pressure, p_{ext} is given:

$$p_{ext} = p_0\left(1 + \frac{4\mu L}{D_0}\right) = 3.90\sigma\left(1 + \frac{4\mu L}{D_0}\right) \quad (18)$$

where, μ is the friction coefficient between the sample and the container, L is the length of the container and D_o is the initial diameter of the billet. Then the load of extrusion F_{ext}, can be described as:

$$F_{ext} = 3.90\sigma\left(1 + \frac{4\mu L}{D_0}\right)A_0 \quad (19)$$

where A_0 is the initial area. Since the extrusion machine has a limit of 100 kN, it is important to know the theoretical value of force of extrusion, considering a suitable value for the friction coefficient.

4.5. Hot Extrusion

The direct rod extrusion tests were performed in a laboratory hot-extrusion system installed in a 100 kN universal testing frame (Fig 4.2). As known, it is very difficult to exactly control the extrusion temperature of the billet, so that the temperature was monitored using a thermocouple inserted in the container, and referring to a previous calibration of the temperature field in the extrusion device.

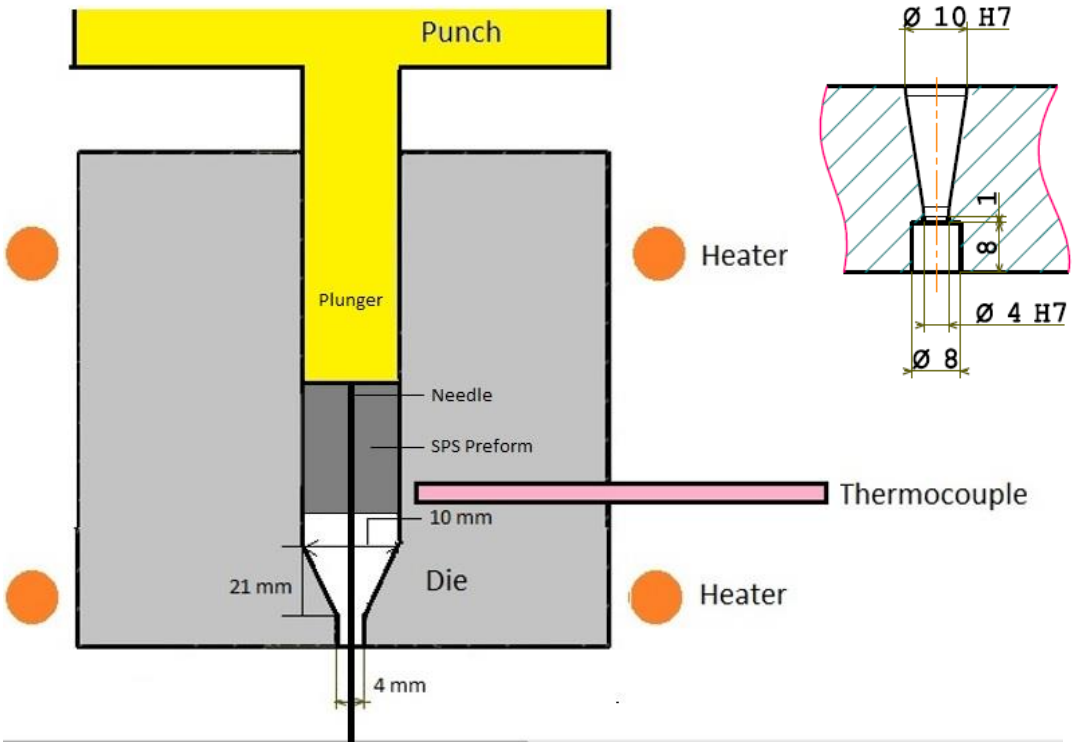

Fig. 4.2 - Schematic drawing of the extrusion (main) and the die drawing (upper right).

The extrusion ratio, R, was 6.25, being the container diameter 10 mm and the diameter of the extruded rod 4 mm. Tests were performed at 330 °C and

380 °C with the ram speed of 0.5 and 20 mm/min, which corresponded, respectively, to strain rates of 1.4 x 10^{-3} and 5.6 x 10^{-2}, according to eq. (14).

The samples will be referred according to the nomenclature reported on Table 4.1.

Regarding the tube extrusion, a needle with 2 mm of diameter was inserted in the plunger. In addition, a hole with 2.1 mm was drilled in the centre of the SPS preform. The extrusion ratio for the tube extrusion was 8, while the calculated R' for the tube extrusion is 24.5. The extrusion was performed at 380 °C at a ram speed of 0.5 mm/min, corresponding to a mean strain rate of 1.8 x 10^{-3}.

Table 4.1 - Sample names and extrusion parameters.

Sample Name	Description	Temperature	Punch speed (mm/min)
330-05	SPS long cycle	330	0.5
330-20	SPS long cycle	330	20
380-05	SPS long cycle	380	0.5
380-20	SPS long cycle	380	20
330-05 S.C.	SPS short cycle	330	0.5
330-20 S.C.	SPS short cycle	330	20
Tube	SPS long cycle	380	0.5

4.6. Microhardness

Microhardness was measured by Vickers methods, according to standard ASTM E384, with a Vickers Paar MHT-4® micro-indenter and load of 0.1 N for 10 seconds holding time.

4.7. Metallographic analysis

The metallographic characterization was carried out using a Zeiss light optical microscope (LOM) equipped with a Leica DC300® camera. Standard metallographic preparation, including grinding with SiC papers up to 2400 grit and final polishing with 3 μm and 1 μm diamond paste was followed. Chemical etching was performed with Nital 5% (5% nitric acid in ethanol solution) and with HF when necessary to observe the γ-phase distribution.

Microstructures, as well as powder morphologies were investigated in a Scanning Electron Microscopy (SEM) and semi-qualitative chemical analysis was carried out by energy-dispersive X-ray spectroscopy (EDXS). Environmental scanning electron microscopy (ESEM) Philips XL 30® (SEM Supra 40 ZEISS, GEMINI column®) was used to characterize the microstructure of the samples. The grain size of the materials was measured using the planimetric (or Jeffries) procedure [63].

4.8. X-ray Diffraction

For powders, sintered and extruded samples, XRD patterns were collected using a Mo kα (λ = 0.7093 nm) source. The experimental data were elaborated with the Rietveld method, using the MAUD software (Materials Analysis Using Diffraction).

In this work, XRD was used to determine the phase composition by quantitative analyses of Pure Mg and AZ91 alloy powders, SPS samples and extruded samples. The quantitative analysis, based on the Rietveld method, considers the area under the peak proportional to the volumetric fraction of the corresponding phase. MAUD software fits the experimental data with the following relation:

$$= I f_j / V_j^2 L_k |F_{k,j}|^2 P_{k,j} A^j \quad (20)$$

where is the intensity of the k peak related to the j phase, I is the incident radiation intensity, f_j is the volumetric fraction of the j phase, V_j is the cell volume of the j phase, L_k is the Lorentz polarization for the k peak, $F_{k,j}$ and $P_{k,j}$ are structure factors and A_j is the absorption factor [64].

4.9. Machining

With the purpose of allow the tube extrusion and the insertion of the needle into the SPS sample, a hole of 2.1 mm of diameter was drilled from the centre of the SPS sample in two steps. At first, a manual 1.7 mm diameter hole was drilled with the speed of 4 mm/min, a second step with the drill of 2.1 mm, and the same speed was performed. The process was carried out with cooling liquid (HYDRO BM) with 6% concentration in water.

In order to obtain tubes with thin walls, the extruded tube of 4 mm of diameter was machined by manual turning, up to reach the external diameter of 2.7 mm. The turning parameters were: turning speed 6 m/min, feeding 0.4 mm and depth of cut 0.1 mm. The cutting was performed without lubrication.

4.10. Laser Cutting

To obtain the stent mesh, a laser cutting of the machined tube was performed under an active fibre laser source, operating in the nanosecond pulse regime with 7 W maximum average power and beam spot of 19 μm. This allowed micro cutting with small kerf widths to be produced across the tube walls. In Table 4.2 the main specifications of the laser source are reported. For tube holding and handling during cutting, a linear and a rotary axis (Aerotech ALS and ACS series) with nanometric resolution were used. The microcutting setup is reported in detail in Figure 4.3. Chemical etching was then performed in HNO_3-ethanol solution under ultrasonic condition to remove the cutting dross and obtain the stent prototype. This part of activities was carried out in co-operation with the group of laser application of the Department of Mechanical Engineering at Politecnico di Milano.

Table 4.2 - Specifications of the laser source.

Wavelength	1064 nm
Maximum average power	50 W
Minimum pulse duration	100 ns
Pulse repetition rate	20-80 kHz
Pulse energy at 50 kHz	1.09 mJ
Collimated beam diameter	5.9 mm
Beam quality factor (M2)	1.7

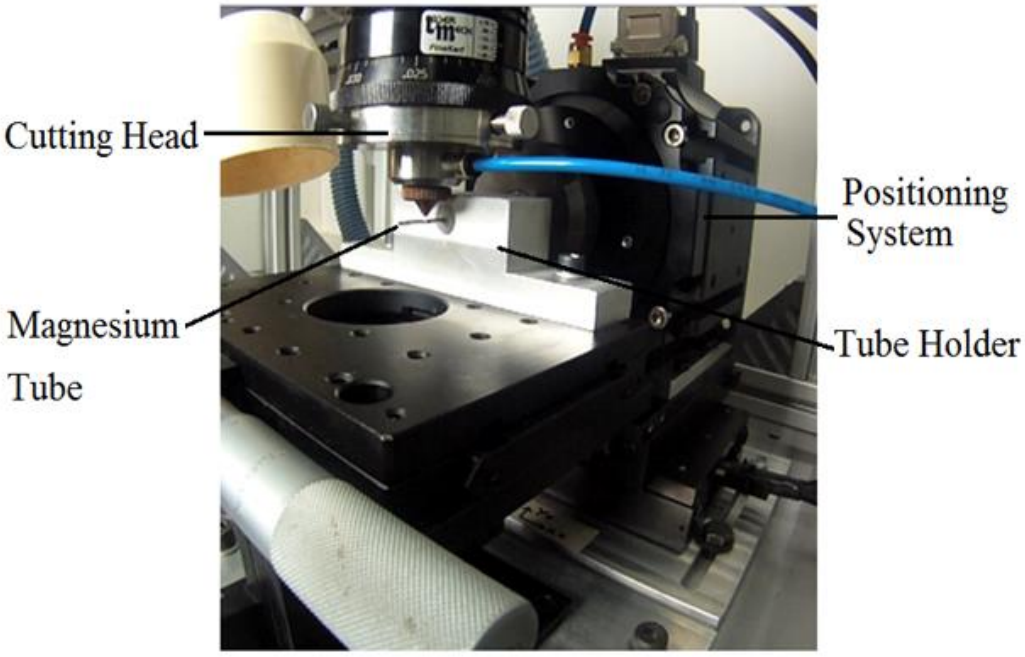

Fig. 4.3 - Laser micro-cutting system.

Chapter V

Results and Discussion

5.1. Spark Plasma Sintering

5.1.1. Powder Characterization

AZ91 powders had a size smaller than 500 μm with an average value of 200 μm. Since they were obtained by chipping and milling, the shape is quite irregular (Fig 5.1) and has a flake-like form, which is not much suitable for compaction of the powder and formation of the green sample. Magnesium is a very reactive material, so, it is expected a layer of MgO on the particle surface, which is corroborated by an EDXS scan, revealing a considerably high amount of oxygen in the surface of the powder.

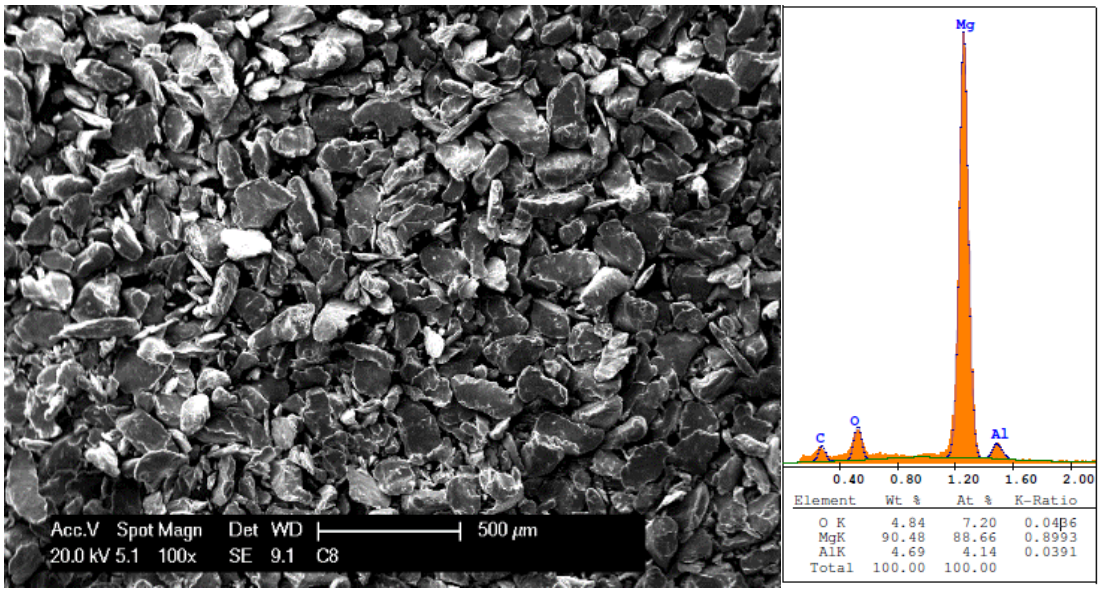

Fig. 5.1 – ESEM images of AZ91 powder (left) and EDXS analysis (right). The C content on the analysis is due to the tape used to hold the powder together.

Fig. 5.2 shows the microstructure of the AZ91 powder, which consists of a Mg rich phase (α phase), the $Mg_{17}Al_{12}$ phase (γ-phase), which is on the grain boundaries, and the lamellar α+γ eutectic precipitates. The considerably high amount of γ-phase, especially as a lamellar phase indicates that the powder was not homogenized. Thus, it would require a homogenization process to

dissolve the γ-phase into the matrix and improve both mechanical and corrosion properties. Nevertheless, since magnesium is a higher reactive material, it is not favourable to perform the homogenization of the Mg powder without any kind of pressing or special atmosphere. Thus, the homogenization process will be performed during the sintering cycle.

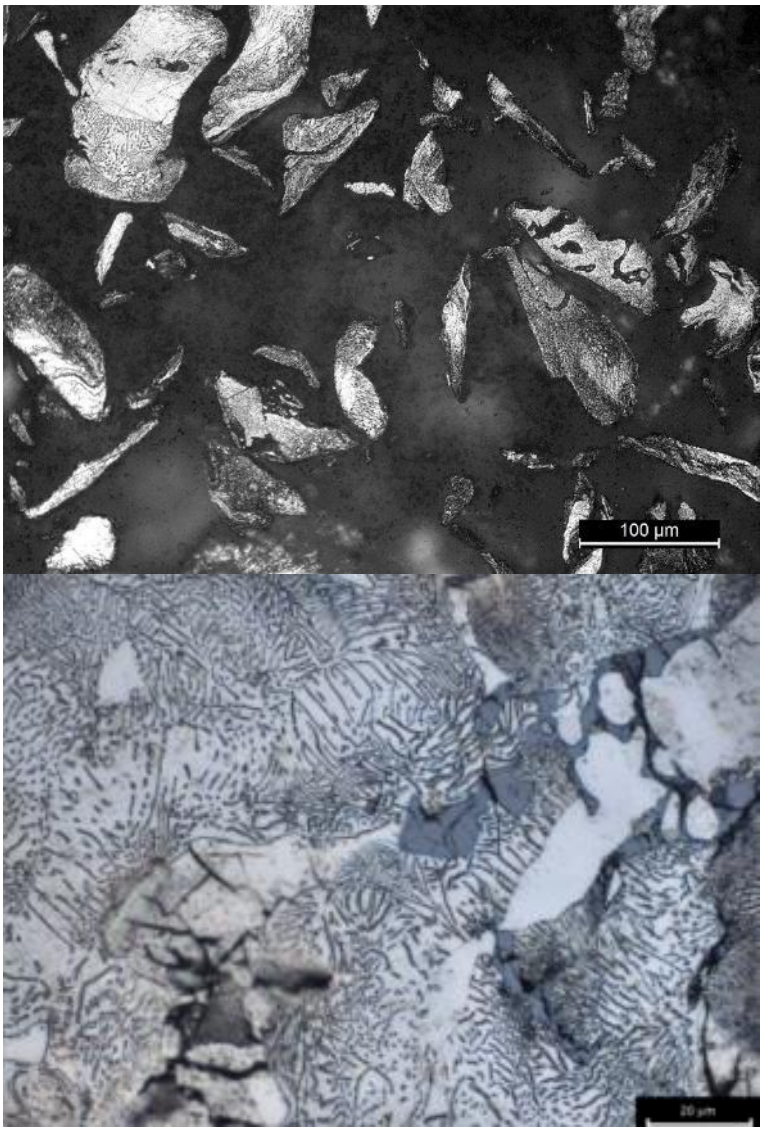

Fig. 5.2 – Microstructure of the AZ91 powder etched with Nital 5% (top) and with HF (bottom).

Through X-ray diffraction (XRD) using Rietveld method (Fig. 5.3), it was determined that the total amount of α phase was 82% vol., the total amount of γ-phase (in grain boundary and lamellar) was 17% vol. and the total amount of MgO was 1% vol.

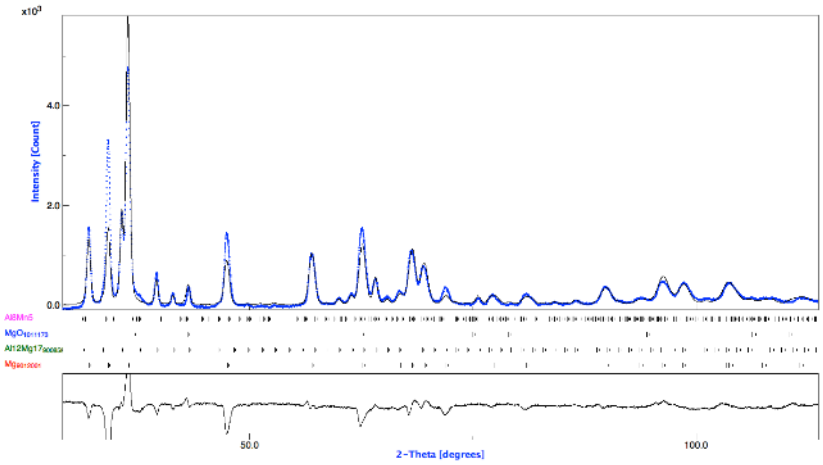

Fig. 5.3 – XRD pattern of AZ91 powder.

The Differential Scanning Calorimetry (DSC) curve of the AZ91 powders, carried out up to 650°C with a heating rate of 10°C/min, is shown in Fig. 5.4. The presence of some peaks corresponding to different phase transformations can be recognized. The most evident and important peaks are labelled with 1, 2 and 3. Peak 1 is the formation of the liquid phase by the eutectic reaction α+γ→ Liquid. Such an endothermic reaction occurred at about 420°C, in substantial agreement with the Al–Mg phase diagram, which shows that the eutectic reaction occurs at 437°C [34]. Peak 2 covers a temperature range between 520 and 615°C and is the melting interval of the alloy. Peak 3 is observed upon cooling. It is an exothermic peak at about 570°C and represents the solidification of the alloy.

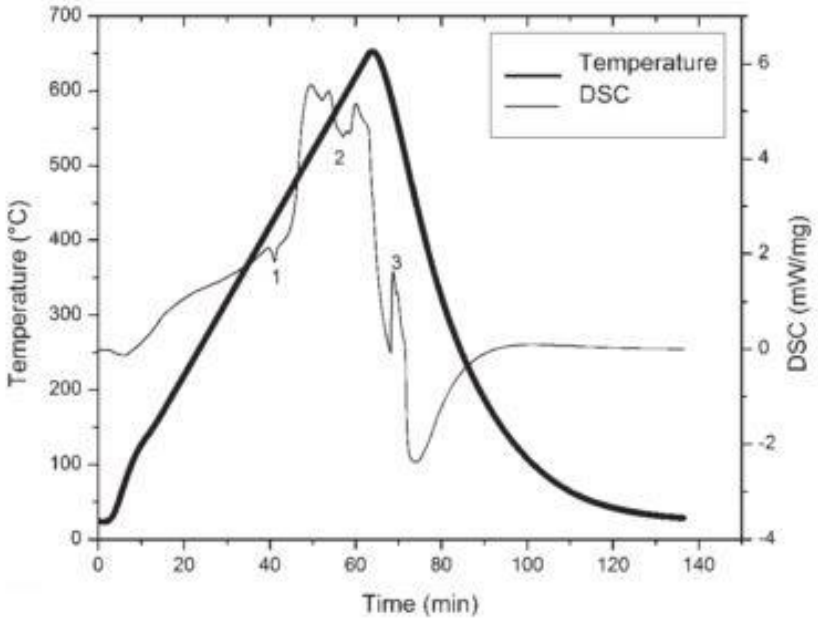

Fig. 5.4 – Differential Scanning Calorimetry (DSC) of AZ91 powders

The pure Mg powder, however, has a much smaller particle size, not exceeding 75 μm. In Fig. 5.5 an optical metallography of pure Mg powder. Since the powders were also obtained by chipping and milling the shape is quite irregular and have a flake-like form, which is not favourable for compaction of the powder and formation of the green sample. However, due to the higher ductility and smaller particle size, the compaction of the green sample is expected to be higher than in the case of the AZ91 powder. On the other hand, the oxide layer should be thicker on the pure Mg, due to the absence of Al and γ-phase, which tends to improve the oxidation resistance [65].

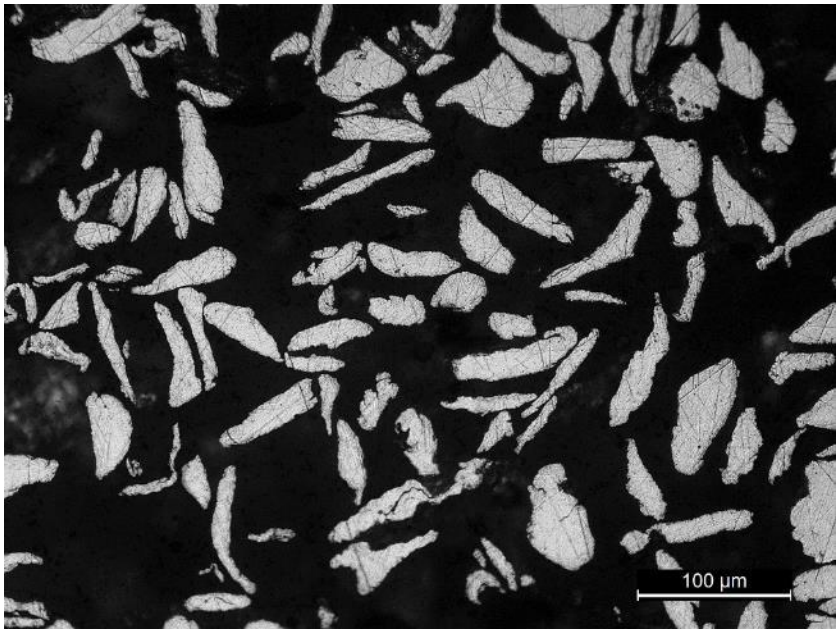

Fig. 5.5 – Optical microscope images of pure Mg powders.

5.1.2. Definition of sintering parameters

If not homogenized, AZ91 forms a liquid phase at about 437 °C. Since this liquid phase is harmful for the SPS process, it must be avoid at any cost. The first and more obvious solution is to keep the temperature below this value. That is the first cycle to be performed. This cycle is named “short cycle”, and consists of heating the powder up to a temperature of 400 °C with a heating rate of 50 °C/min and holding at this temperature for 10 minutes under a pressure of 25 MPa.

Magnesium powders are very difficult to sinter, due to their high reactivity versus oxygen, the MgO layer formed on the powder surface tends to impede the sintering mechanisms. Therefore, the higher the temperature, the higher is the energy available to break this oxide layer. Thus, to achieve a high temperature, a homogenization process is required.

In order to understand the SPS process and observe if the formation of the liquid phase really occur, the displacement rate of the punch was recorded while the temperature was increased up to 470 °C and a pressure of 25 MPa was applied after 400 °C. The obtained graph is shown on Fig. 5.6. It is

possible to notice that the first displacement peak begins when the pressure is applied. The second peak, however, shows a displacement of the punch even if there is no difference on the applied pressure. It starts when the sample reaches 400 °C and have its maximum at a temperature of 430 °C, showing the formation of the liquid phase, according with the DSC and the Mg-Al phase diagram.

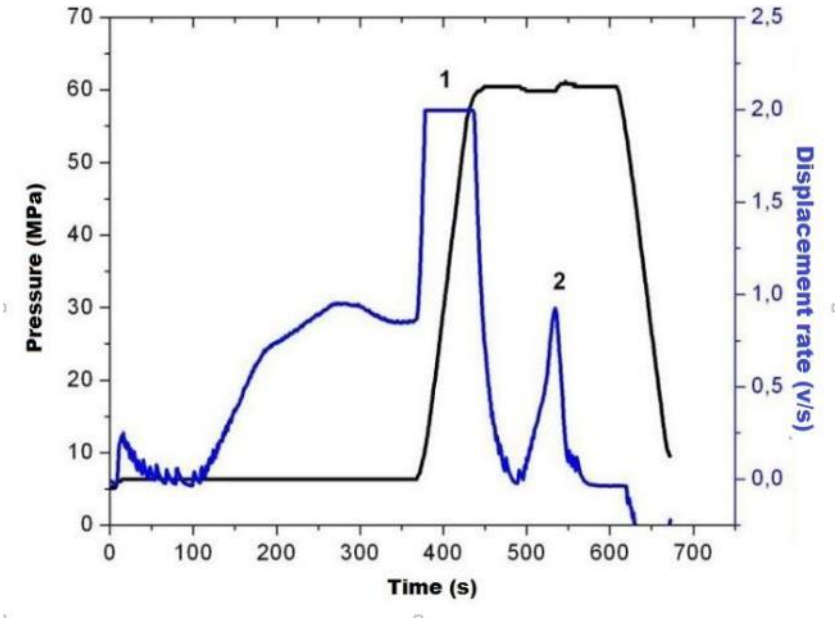

Fig. 5.6.– Change on the dislocation rate of the punch in function of time and pressure applied.

In order to avoid the liquid phase, a homogenization process was carried out for 60 minutes at 420 °C and then the temperature was increased up to 470 °C without any change on the displacement rate during the homogenization and the sintering. This is shown on Fig. 5.7. It is possible to say that the sintering of AZ91 can be performed at 470 °C if previous homogenization is carried out. This cycle is denominated the “long cycle”.

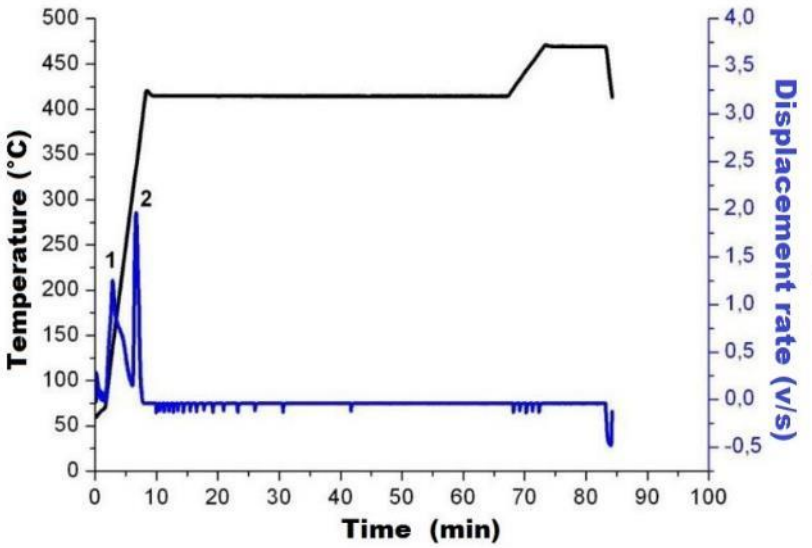

Fig. 5.7 – Dislocation rate of the punch in function of the time and temperature during sintering

For the pure magnesium powders, the sintering was performed at the same temperatures of the AZ91 alloy, namely 400 °C and 470 °C. Since pure magnesium do not form precipitates, no previous homogenization process was adopted. The 4 cycles are displayed on the Fig 5.8.

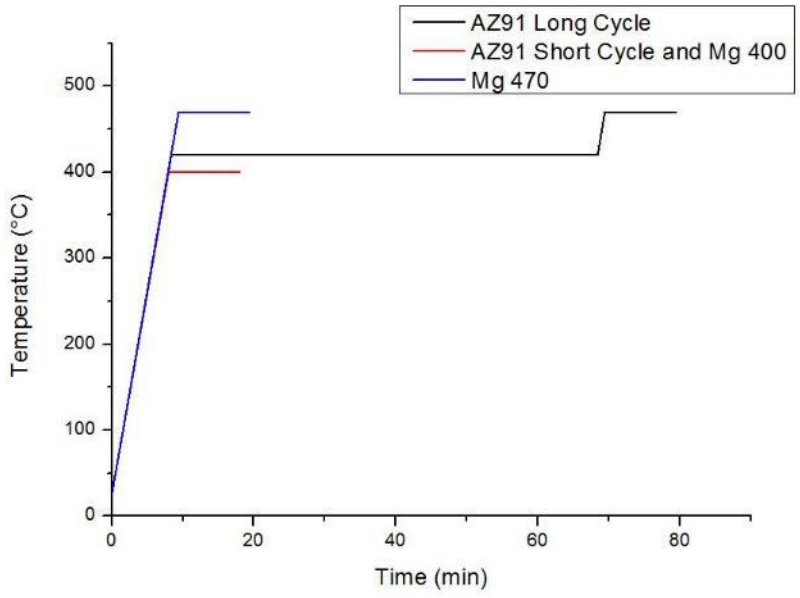

Fig. 5.8 – Defined sintering cycles for both pure Mg and AZ91.

5.1.3. Comparison of Short and Long Cycles for AZ91

Fig. 5.9 shows the microstructure of the AZ91 produced following the short cycle. It presents quite low densification, most probably due to the larger amount of γ-phase, since this cycle was not submitted to homogenization. Other interesting characteristic is the presence of connected pores, which causes a serious decrease in the mechanical properties. It is also possible to notice the original powder surface, indicating that the welding between particles is not present, harming seriously the structural integrity of the preform. The preform obtained with the short cycle showed to be very brittle, even during handling some of them broke. Since the preform is still going to be extruded, it was decided to go further and see if the strain and temperature during extrusion is able to both break the interparticular layer of oxide and close the pores, giving a better mechanical resistance.

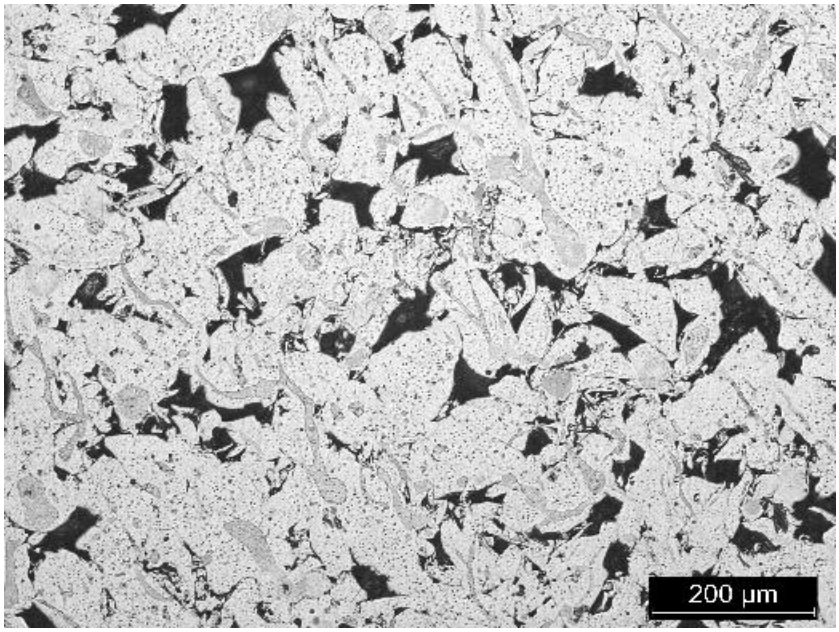

Fig. 5.9.– Optical microscope image of SPS AZ91 short cycle.

On the other hand, the long cycle preform showed a very different microstructure, as shown in Fig. 5.10. The original powders cannot be recognized, and the densification is very good, achieving values of 99.9% of the theoretical density. The pores are small and dispersed, providing the preform with a better mechanical behaviour. Due to the homogenization process, the quantity of γ-phase into the preform decreased to only 4%, which

improves both mechanical and corrosion properties. The lamellar phase disappeared, enriching the α-phase with Al. Through XRD analysis, it was determined that the total amount of γ-phase decreased from 17% vol. in the powder to only 4% vol. after the homogenization on the long SPS cycle. The preforms produced by the long cycle resulted in good resistance during handling and transportation.

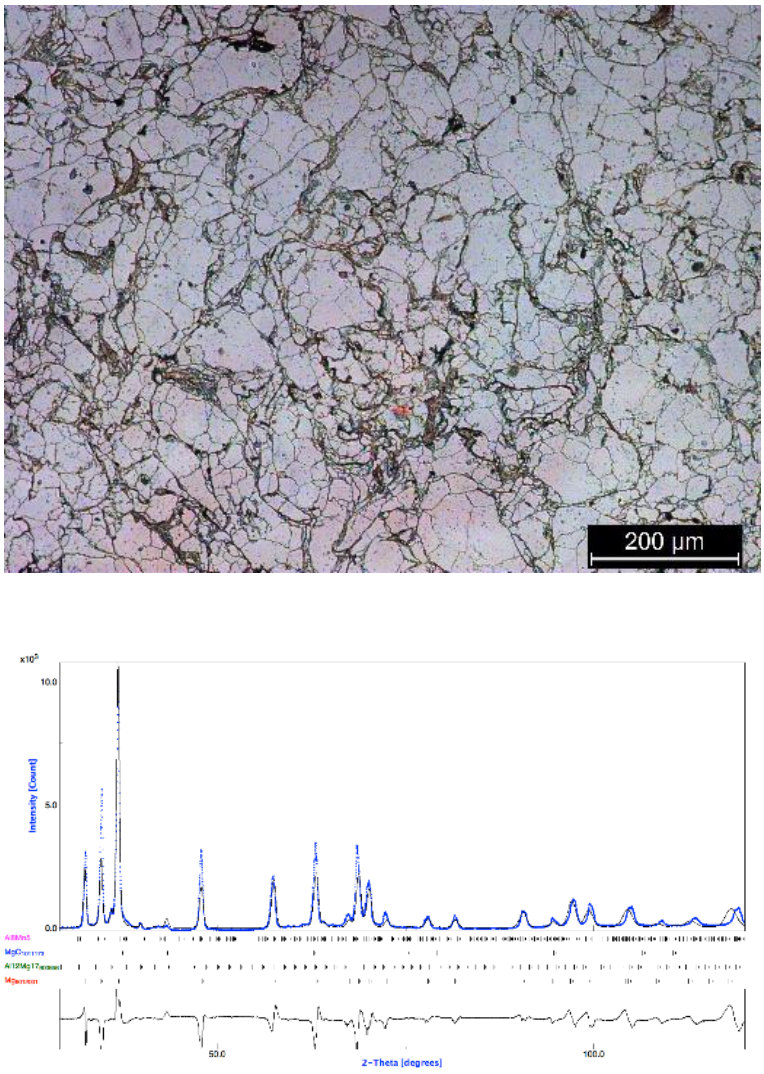

Fig. 5.10 – Optical microscope images of SPS AZ91 long cycle (top) and XRD analysis (bottom).

5.1.4. SPS of pure Mg

For the Pure Mg SPS sample, two different cycles were proposed, the first at 400 °C and the second at 470 °C. The microstructure of the materials are shown in Fig. 5.11. The microstructure obtained at 400 °C showed the presence of some pores, and since the original pure Mg powders are much smaller than the AZ91, the densification turned out to be much higher than the densification of the short cycle on AZ91. Another factor that can influence the densification is the lower mechanical strength of the pure magnesium due to the lack of precipitates in the material. The SPS at 470 °C does not induce a very different microstructure. It is interesting to notice that the grain size in both preforms is equal to the original powders particle. This is due to the grain growth during sintering, and without any barriers avoid the grain growth, except the oxide layers between the particle boundaries the grain grew up to the size of the original powder (maximum 75 μm).

If the grain size equals the particle size, it is clear that the original oxide layer on the powder surface remained intact, and thus, the mechanical resistance of the pure magnesium preform is expected to be similar in both temperatures, due to the net of MgO in the microstructure. In fact, the brittleness of the samples is very evident, and even some powder particles are removed from the preform just by holding it. It was decided to proceed only with the pure Mg preform produced at 400 °C.

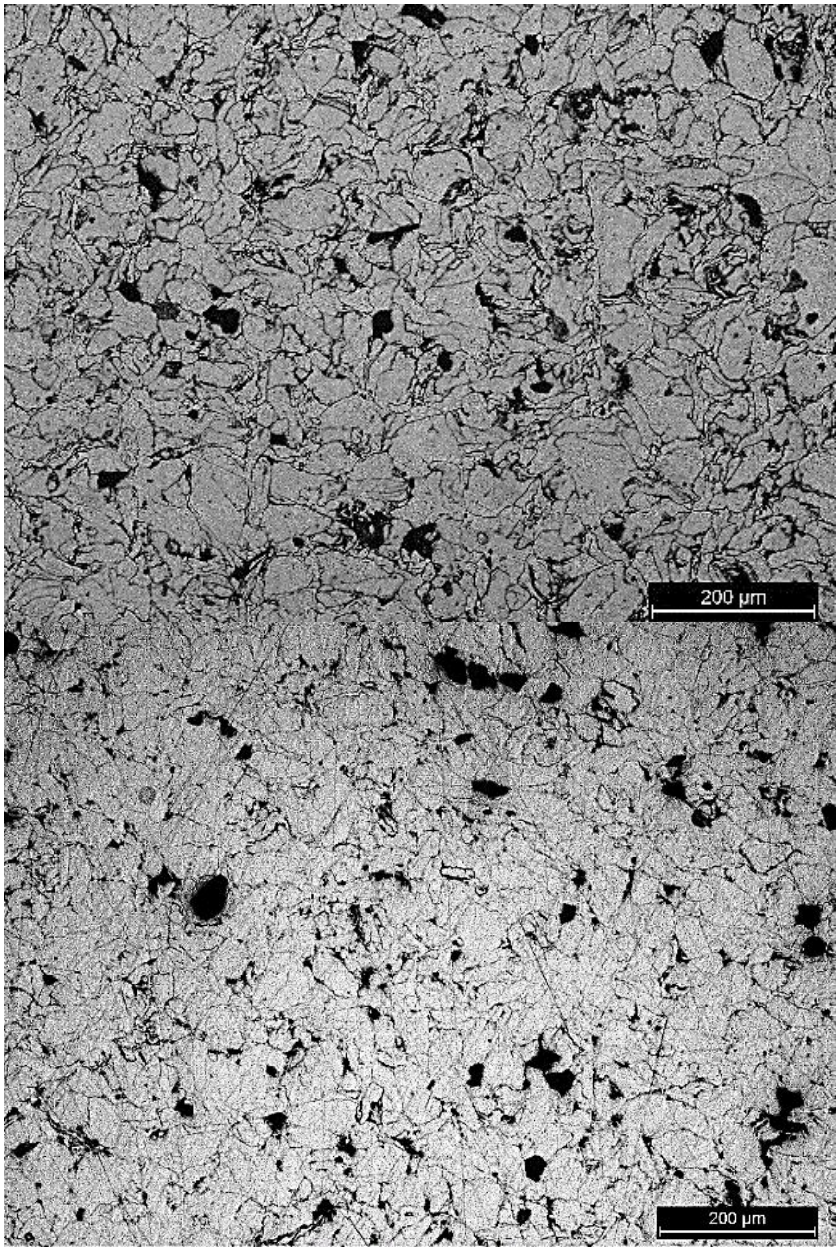

Fig. 5.11 – Optical microscope images of pure Mg SPS at 400 °C (top) and 470 °C (bottom),

5.1.5. Hot compression of Sintered Samples

Fig. 5.12 compares hot compression behaviour for both AZ91 and pure Mg when submitted to a strain of 0.5 at a rate of 0.002 s^{-1}. Two physical events must be considered. The first is the work hardening, which increases the dislocation density and is responsible for the rapid initial stress increase. The high concentration of dislocation together with the high temperature yield the second phenomenon, called dynamic softening, which occurs when the damaged structure of the material finds a way to use the temperature energy

in order to decrease the Gibbs free energy by dynamic recrystallization, for example. These two events compete with each other and define the shape of the curve after the initial yield point [66], [67].

The pure Mg preform shows a typical behaviour with the increasing of the stress during the test. At lower strains, the increase of dislocation density, inducing a rapid increase in strength. After this stage, the flow softening starts to take place and decreases the slope of the curve, but the mechanical hardening is still stronger than the flow softening. In addition, as predicted, the flow stress is higher for the lower temperature, since this parameter is correlated with Zener-Hollomon parameter (eq. 21); thus for lower temperatures, a higher stress is expected.

$$Z = \dot{\varepsilon}\exp(Q_{act}/RT) \quad (21)$$

On AZ91, the initial slope is much higher and this may be due to the presence of γ-phase that induces a higher increase in the dislocation density. After reaching the peak, the flow softening starts taking place and rapidly decrease the flow stress, which tends to induce a steady state value. This is a typical behaviour of dynamic recrystallization (DRX) on AZ91, also shown by Ding et al. [66]. The difference in the slope of the flow stress after the peak stress for the AZ91 samples 330 and 380 °C may be explained by the quantity of energy absorbed during the initial stage, and transformed in DRX.

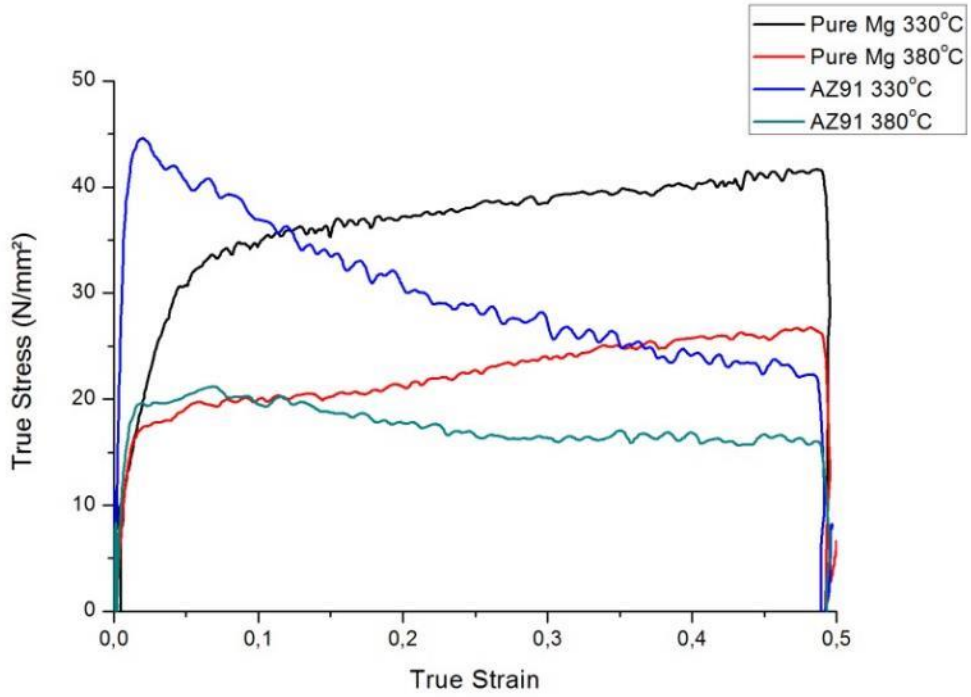

Fig. 5.12 - Flow stress-strain curves obtained from hot compression tests at 0.002 s^{-1} and temperatures of 330 °C and 380 °C.

Pure Mg was also submitted to higher strain rates, however, only the samples at 0.002 s^{-1} did not break during the tests. From the images shown on Fig. 5.13, is possible to observe the high amount of interparticular cracks on both samples. This means that the network of MgO served as a path for the propagation of the cracks on the material. It is also possible to notice no change on the grain size either, the grain size was limited by the original particle size, and the structure could not hold any grain refinement due to the lack of barriers to avoid the grain growth.

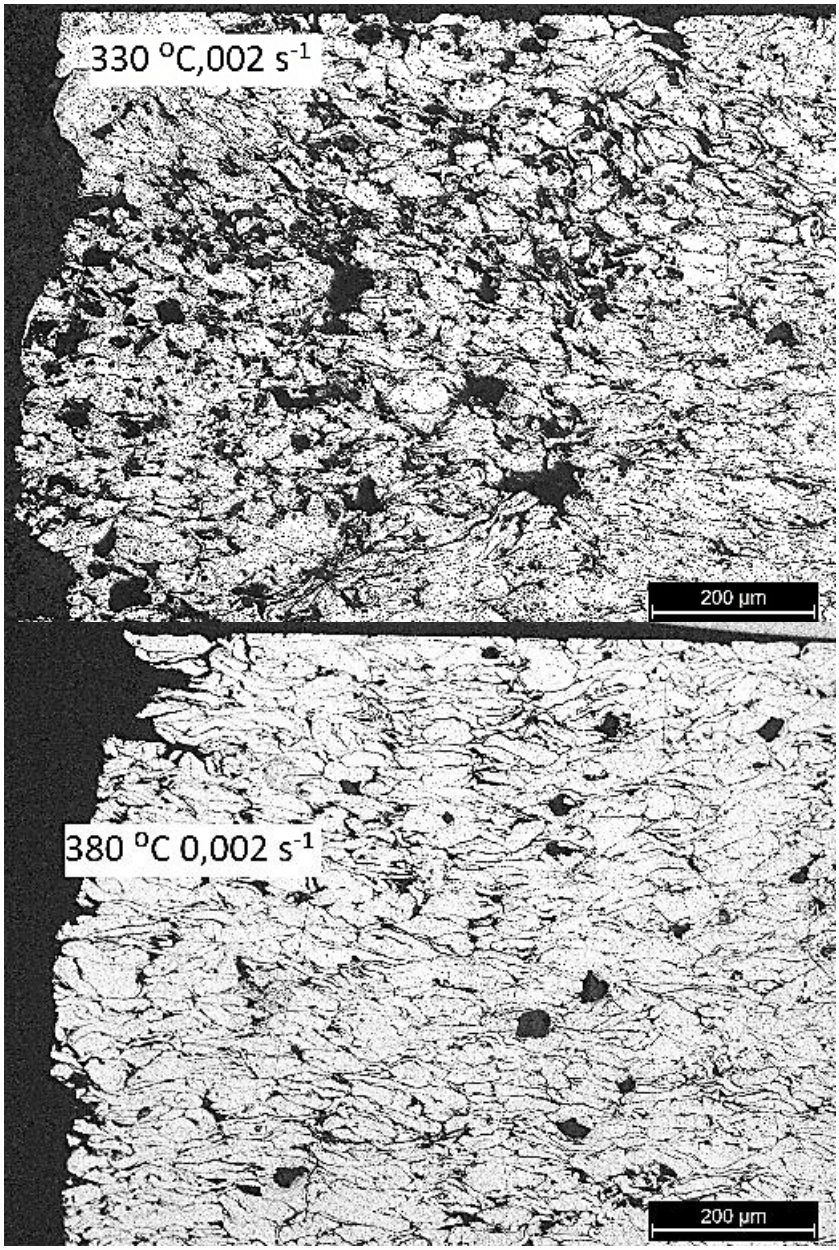

Fig. 5.13 – Optical microscope images of hot compressed samples of pure Mg at a temperature of 330 °C (top) and 380 °C (bottom).

The flow stress curves under compression of AZ91 alloy are presented on Fig. 5.14. Two different temperatures and three different strain rates were evaluated. The choice of 1 s^1 is to see how the material behaves under a high strain rate, and if the sintering of was capable of give enough mechanical resistance to the SPS preform. The other two strain rates were selected to be a simulation of the extrusion tests. The goal was to simulate the extrusion of the SPS preform, with 10 mm of diameter, into a rod of 4 mm of diameter at ram speed of 0.5 mm/min and 20 mm/min. Considering the eq. (14), and the

parameters of the extrusion die, the strain rate of the extrusion tests would be 0.0014 s^{-1} and 0.056 s^{-1}.

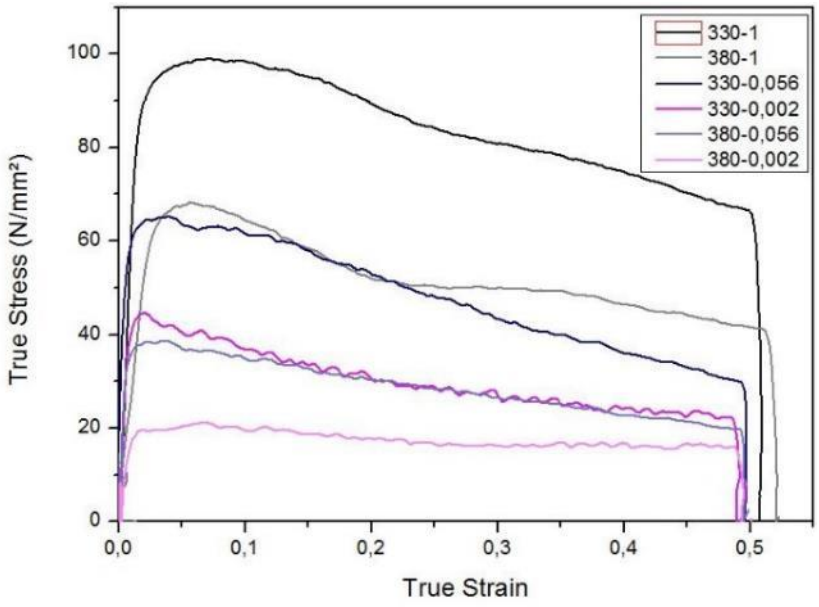

Fig. 5.14 – Flow stress under compression curves of AZ91 alloy.

In every case, at the beginning there is a rapid increase in the stress due to work hardening, which is due to the accumulation of dislocations. Quite soon, the flow stress reaches a peak value and then decreases. Such a decrease is commonly attributed to the occurrence of DRX [59], and this is actually in agreement with our observations, as shown by the microstructures in Fig. 5.15. It is interesting to notice that the influence of the temperature on the behaviour of the material. The yield stress for a hot compression at 380 °C at a strain rate of 1 s^{-1} is almost equal to that of the test at 330 °C at a much lower strain rate, 0.056 s^{-1}, and the same occurs when comparing the hot compression 330-0.002 and the 380-0.056.

It is interesting to notice that a difference on almost 20 times on the strain rate is similar to a change of only 50 °C. This is explained by the Zener-Hollomon parameter (eq. 21). Since strain rate is directly proportional to Z, but the effect of the temperature is exponential.

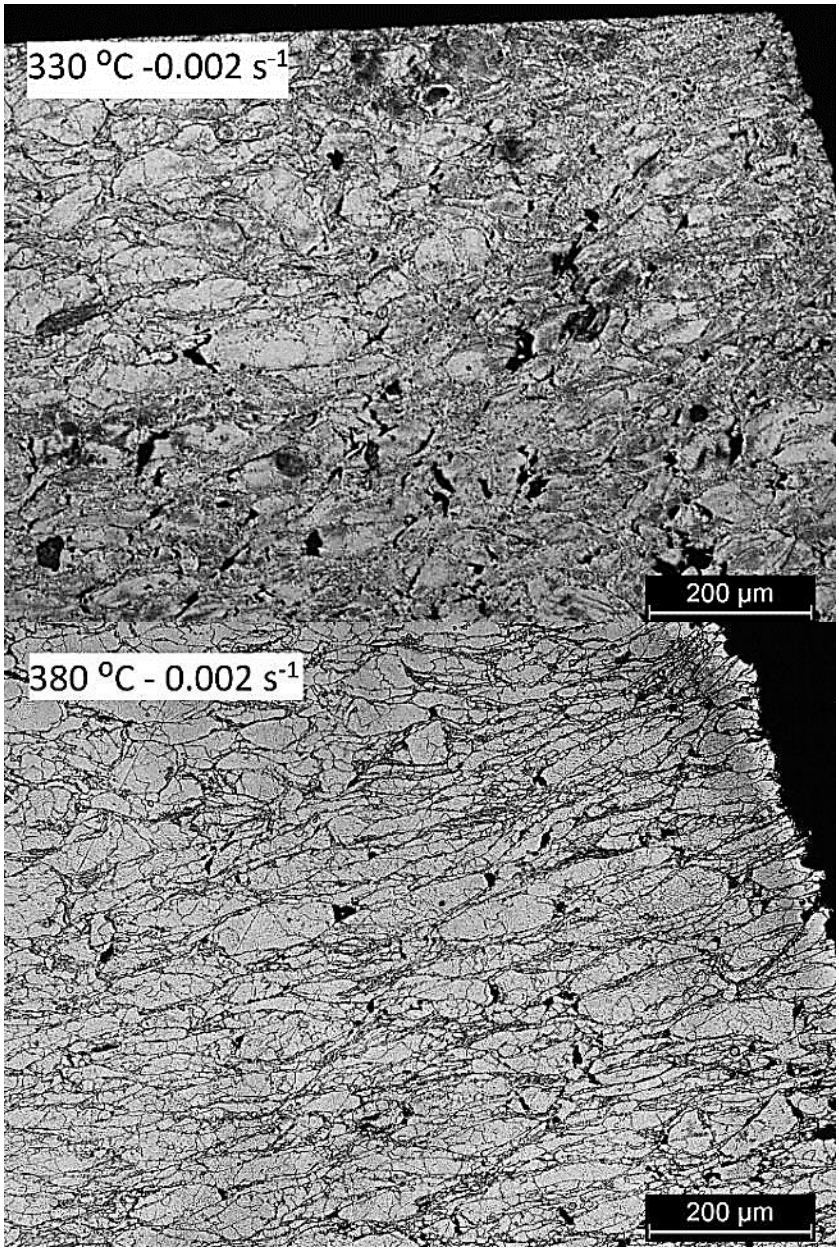

Fig. 5.15 – Optical microscope images of hot compressed samples of AZ91 at a temperature of 330 °C (top) and 380 °C (bottom) and strain rate of 0.002 s^{-1}.

The microstructure of the samples compressed at strain rate of 1 s^{-1} is shown on Fig. 5.16, revealed several cracks on the critical part of the specimen. Despite the high amount of cracks, at both temperatures the material did not break, showing that the sintering was quite successful.

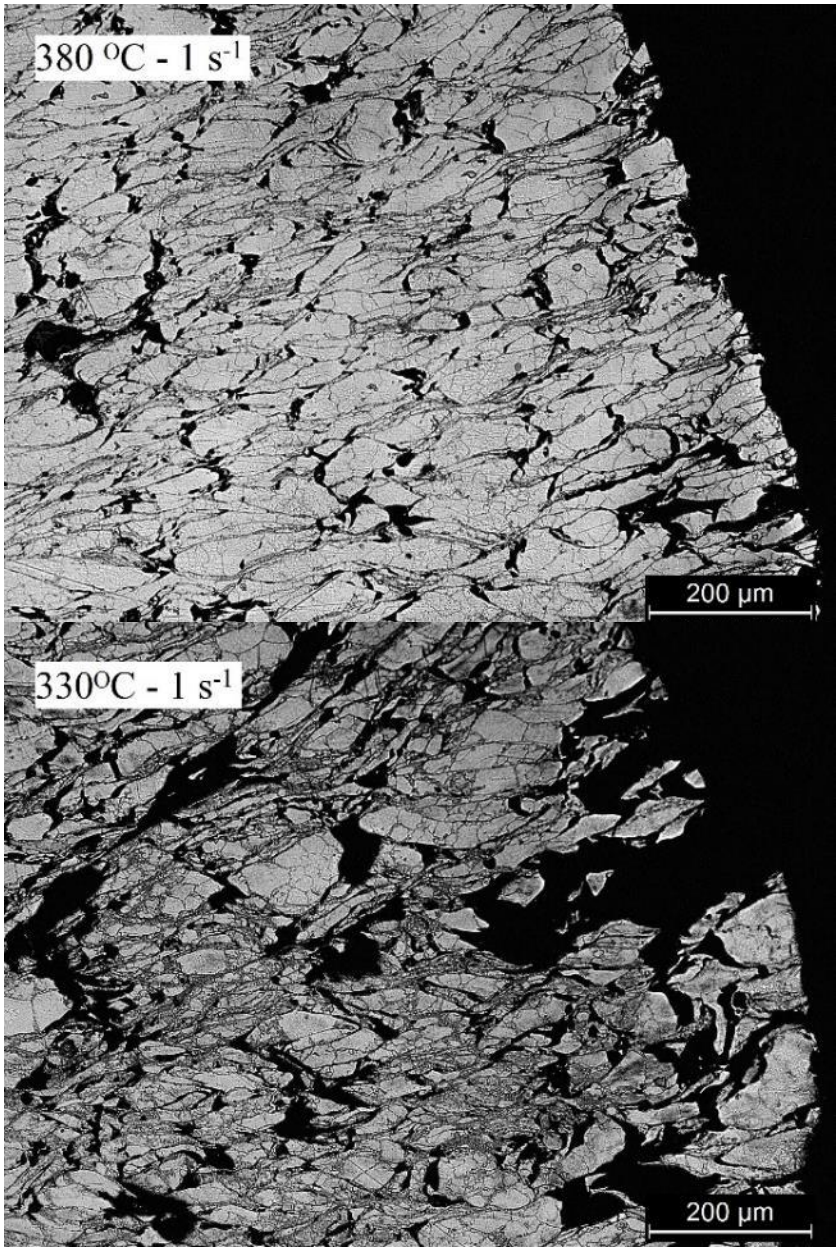

Fig. 5.16 – Optical microscope images of hot compressed samples of AZ91 at a temperature of 330 °C (top) and 380 °C (bottom) and strain rate of 1 s^{-1}.

Due to limitations of the extrusion machine, the load of extrusion must be calculated to be certain that does not exceed the value of 100 kN. In order to do so, the peak stress measured on the hot compression analysis. The peak stresses, σ_e, measured from the graphs in Fig.5.14 are listed in Table 5.1. The data listed in Table 5.1 was then used to get an approximate evaluation of the expected extrusion force (F_{max}), during hot extrusion.

Since μ is defined as a ratio of forces, it cannot be measured directly and an inverse approach should be adopted [68]. By using the peak values listed

in Table, applying it to eq. (19) and assuming that for the magnesium-steel interface a friction coefficient of 0.3 is considered [58], is possible to have a estimation of F_{max}.

Table 5.1 – Predicted values for extrusion load.

Sample Name	σ_e (MPa)	p_0 (MPa)	p_{ext} (MPa)	Predicted F_{max} (kN)
HC AZ91 330-1	99	386	1359	106
HC AZ91 380-1	68	265	933	73
HC AZ91 330-0.056	66	257	906	71
HC AZ91 330-0.002	45	175	617	48
HC AZ91 380-0.056	38	148	521	40
HC AZ91 380-0.002	21	81	288	22

The calculated values of extrusion force showed that if the friction coefficient during the extrusion tests are really 0.3, the tests at higher strain rate than 0.056 s^{-1} (equivalent to a ram speeds of 20 mm/min) is not possible due to the limitation of the extrusion machine of 100 kN of maximum force. Thus, it was decided to proceed only with the strain rate of 0.002 s^{-1} and 0.056 s^{-1}.

5.2. Extrusion

5.2.1. Rod extrusion SPS short cycle preforms

The samples produced by the short cycle (without homogenization and at 400 °C) where extruded at 330 °C at 0.5 mm/min and 20 mm/min. Since the samples were not homogenized, the higher presence of γ-phase induced a very brittle sample. During the extrusion, it was reported some sample rupture, as shown on Fig. 5.17 (a). The more detailed images obtained by ESEM of the fracture surface are shown in Fig. 5.17 (b) shows the existence of brittle cracks caused by the precipitates not solubilized on the SPS cycle.

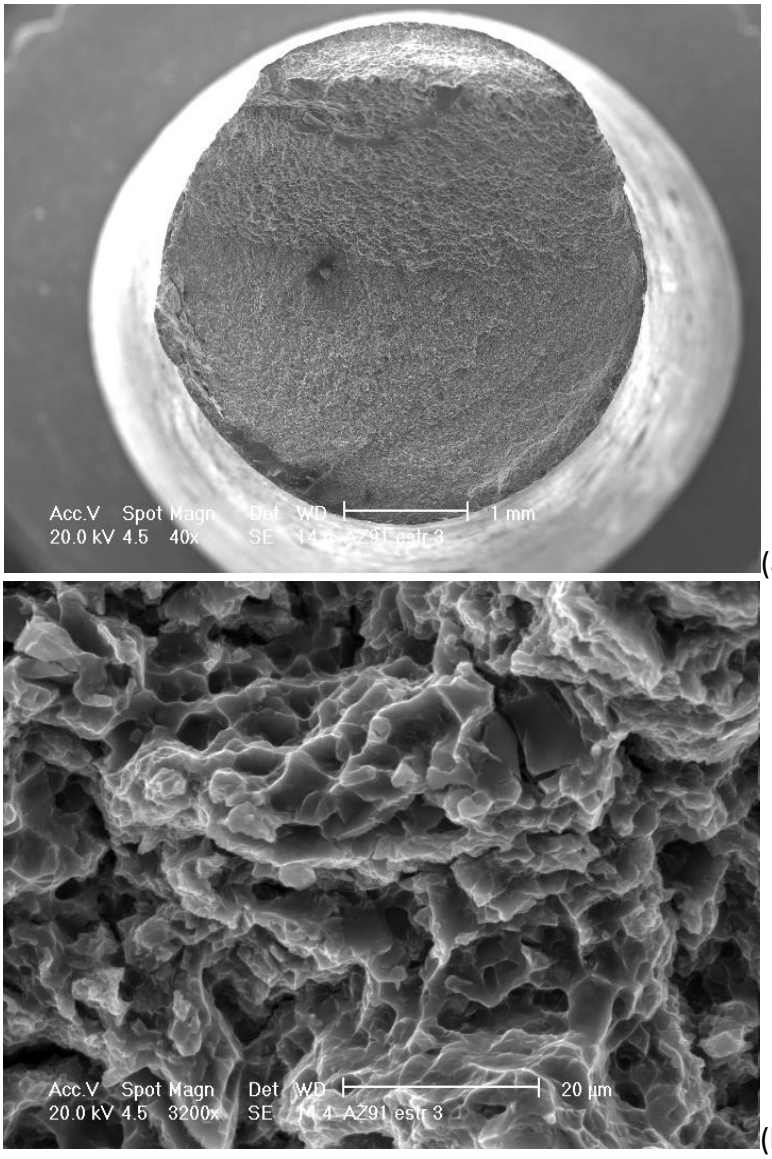

(a)

(b)

Fig. 5.17 – Fracture surface images obtained by ESEM.

Despite the fracture on some SPS samples, the extrusion tests on the short cycle SPS were performed, and the first thing to notice is that, as expected, the pores present after sintering are no longer present after extrusion. It is possible to notice from the Fig. 5.18 that in both conditions the microstructure is very non-homogeneous. It is clear the difference between the γ-phase rich region and the γ-phase poor region. The effects of such microstructure can be catastrophic to both mechanical and corrosion properties. With that in mind and along with the preform brittleness, it was decided to restrict our investigation on the SPS samples produced by the long cycle only.

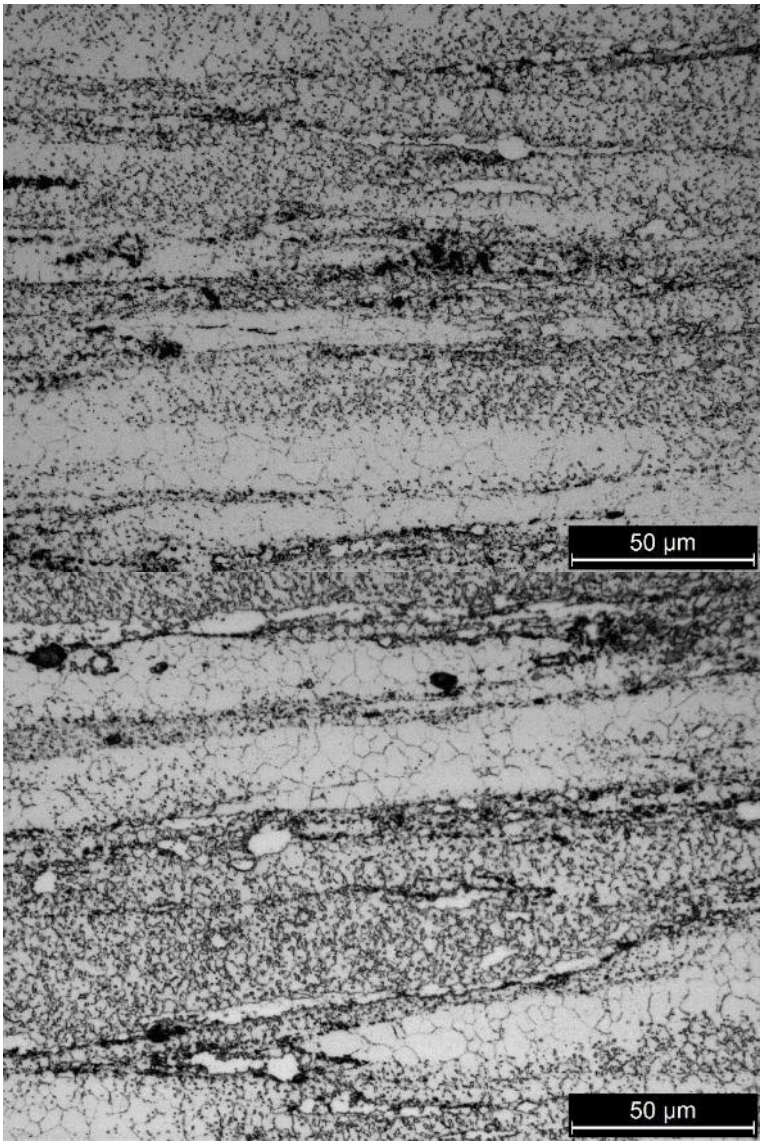

Fig. 5.18 – Optical microscope images of SPS short cycle extruded at 330 °C with a ram speed of 0.5 mm/min (top) and with a ram speed of 20 mm/min (bottom).

5.2.2. Rod extrusion of SPS long cycle preforms

One important factor in develop biodegradable stents is the control of the corrosion rate. It should be controlled in a way that it not penalizes the strength and resistance of the stent, but after performing its function, the stent can be absorbed by the body. One way is to increase the corrosion resistance is the grain refinement by performing the extrusion [65].

The grain refinement is determined by the dynamic recrystallization (DRX) in the material during hot extrusion. The following relation gives grain size in relation to the Zener-Hollomon parameter

$$[Z]d^p = \left[\dot{\varepsilon}\, exp\left(\frac{Q}{RT}\right)\right] d^p = constant \qquad (22)$$

Where Z is the Zener-Hollomon parameter, $\dot{\varepsilon}$ is the strain rate, Q is the activation energy, R the gas constant, T the absolute temperature, d is the grain size and p the grain size exponent. Then grain size can be given by:

$$d \propto \left[\dot{\varepsilon} exp\left(\frac{Q}{RT}\right)\right]^{-1/p} \quad \text{or} \quad d \propto [Z]^{-1/p} \qquad (23)$$

From eq. (23) it is obtained that the grain size decreases by increasing the strain rate and decreasing the temperature, being it< inversely proportional to Zener-Hollomon parameter. In order to reduce the grain size of the material, four different settings were chosen. Table 5.2 shows the extrusion parameters and the corresponding Zener-Hollomon parameter. It was taken from the literature that the activation energy (Q) for lattice diffusion on Mg is about 135 kJ/mol [69], [70].

Table 5.2 – Extrusion parameters and respectively Zener-Hollomon parameter.

Sample Name	Temperature (°C)	Ram Speed (mm/min)	$\dot{\varepsilon}$ (s^{-1})	Zener Hollomon Parameter (s-1)
330-05	330	0.5	1,4E-03	6,91E+08
330-20	330	20	5.6E-02	2,77E+10
380-05	380	0.5	1,4E-03	8,80E+07
380-20	380	20	5.6E-02	3,52E+09

In order to analyse the microstructural evolution of the different samples during the rod extrusion tests, the optical microscopic observations were performed according to the Fig. 5.19 (a), and the regions denominated as “b”, “c”, “d” and “f” represent areas with different mechanical deformations. Region “b” lays in front of the plunger, where there is no strain, but the densification caused by the extrusion pressure and the effects of the temperature are present. Region “c” is in the centre of the extrusion. Region “d” is the centre of the extruded part, the “final” microstructure. It represents the state of the microstructure after the process. Region “f” is the outer part of the extruded rod, close to the die walls.

Fig. 5.19 shows the evolution on the microstructure for the 330-05 sample. On region “b” is possible to notice the presence of a very similar microstructure to the one observed on the SPS preform long cycle. The presence of large grains and a mesh of MgO layer is present. In the regions “c” and “d”, is seen that these oxides become aligned along the extrusion direction, which is an indication that the gradually, the interconnected mesh of MgO is going under deformation and breaking.

On region “c”, on the extrusion part, the signs of recrystallization are evident, with equiaxed grains, but the original particles are still recognizable, since the MgO mesh is not completely broken. In region “d”, after extrusion, the sample does not show any non-recrystallized regions, as noticed on the region c, and the oxide layer is not so evident anymore. It is possible to notice that the grains are completely recrystallized, evidenced by the equiaxed grain present on the microstructure. Fig. 5.19 (e) shows more closely the microstructure of region “d”.

The material is not homogeneous; the microstructure on outside part of material (Fig. 5.19 (f)) is finer than the core. This occurs in all samples and will be studied in detail on a specific section. Despite the action of friction, no cracks were found on this region.

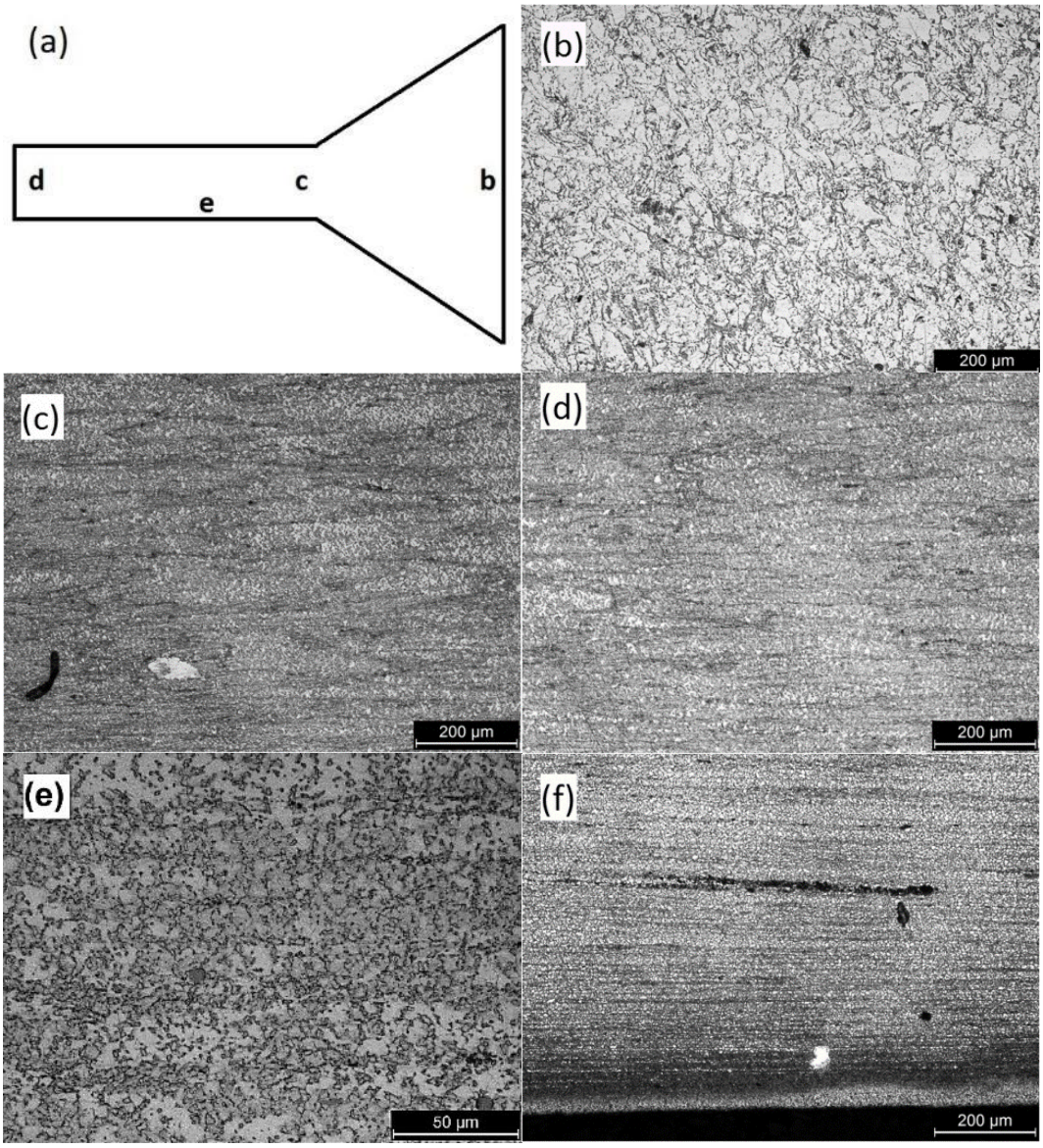

Fig. 5.19 - Microstructural evolution on sample 330-05 at the points indicated in figure (a), being the fig (e) the amplified microstructure of region "d".

The sample 330-20, extruded at a temperature of 330 °C and a ram speed of 20 mm/min. The microstructure is shown on Fig 5.20 In region "b" a very similar microstructure to the preform produced by the long cycle. In region "c" is noticed that most part of the grains are recrystallized, however, some parts present large grains. In comparison with the 330-05, more non-recrystallized areas are formed. One important characteristic observed on the 330-20 sample is that the MgO layer is already broken on the region "c" and is almost unrecognizable on region "d".

Region "d" shows two different microstructures, the recrystallized with refined microstructure and the non-recrystallized with large grains. This is due

the fact that at higher ram speed, the time was not enough to induce the full recrystallization, especially in the centre of the rod, where the local strain is lower. Fig. 5.20 (e) shows the microstructure of region “d” in more detail. In the outer region of the rod, the region “f”, the higher ram speed induced many cracks in the materials. In the outer region, is possible to notice the flow of the material and the small grains formed in the outer region.

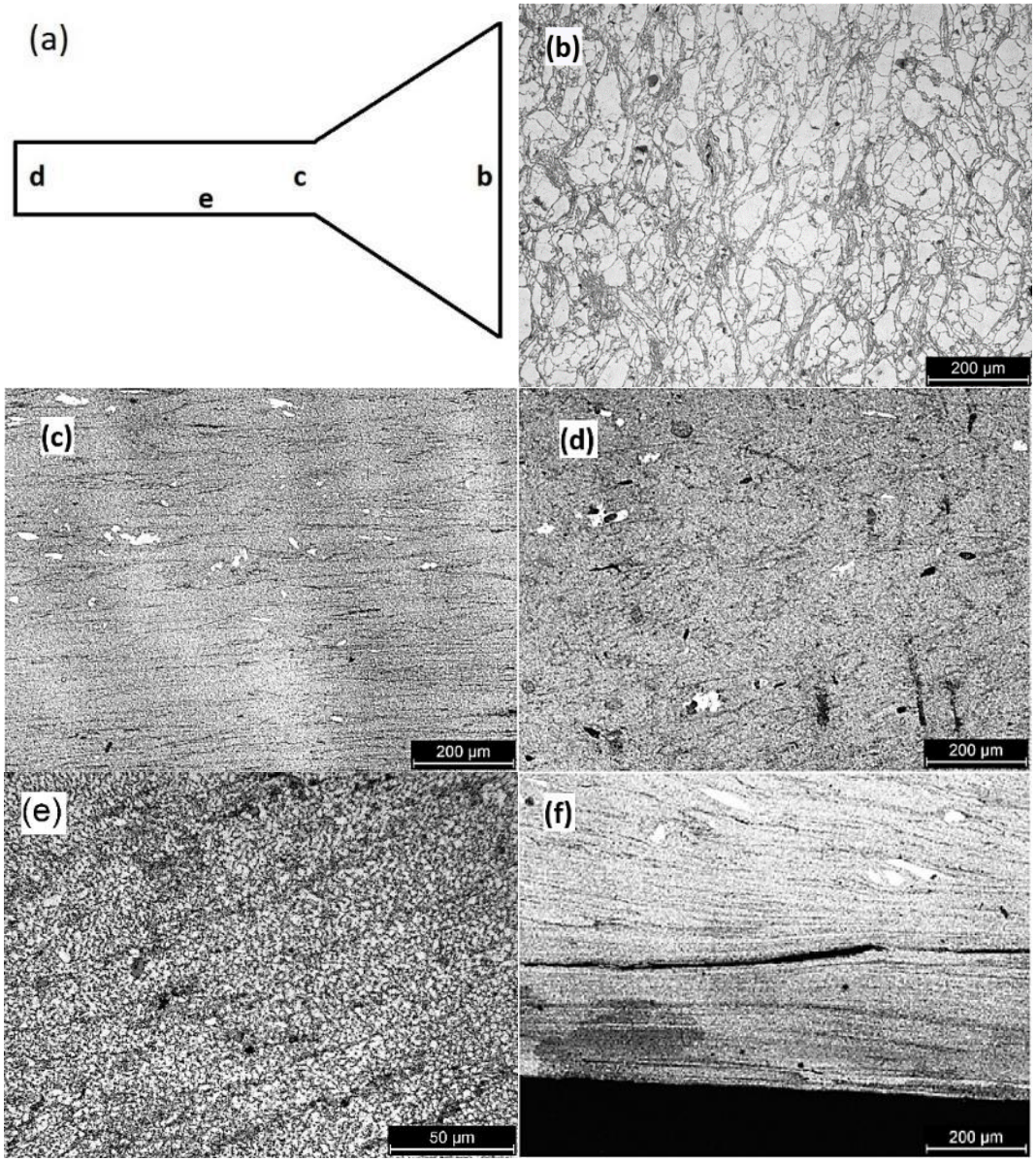

Fig. 5.20 - Microstructural evolution on sample 330-20 at the points indicated in figure (a), being the fig (e) the amplified microstructure of region “d”.

Fig. 5.21 shows the microstructure evolution on the rod extrusion test 380-05. Fig. 5.21 (b) shows that the grain coarsening occurred before the extrusion, since the grain size is slightly bigger than the original preform

sample. Unlike the extrusions performed at 330 °C, the non-recrystallized regions was not present. The grain size after the extrusion is, as expected higher in comparison with the extrusions performed at 330 °C. On region “c” and “d” is possible to notice that the oxide mesh is oriented with the extrusion direction and after extrusion (region “d”) the oxide mesh is almost unrecognizable. In both regions “c” and “d” the equiaxed grains are a sign of the occurrence of DRX. Also on this sample, the outer region showed a higher level of DRX, but the difference on this sample was not so evident when compared with the other samples, it appears that at high temperature and low speed the material had time to induce a uniform microstructure regarding the grain size. It is also important to notice that the region “f” does not show any sign of cracks.

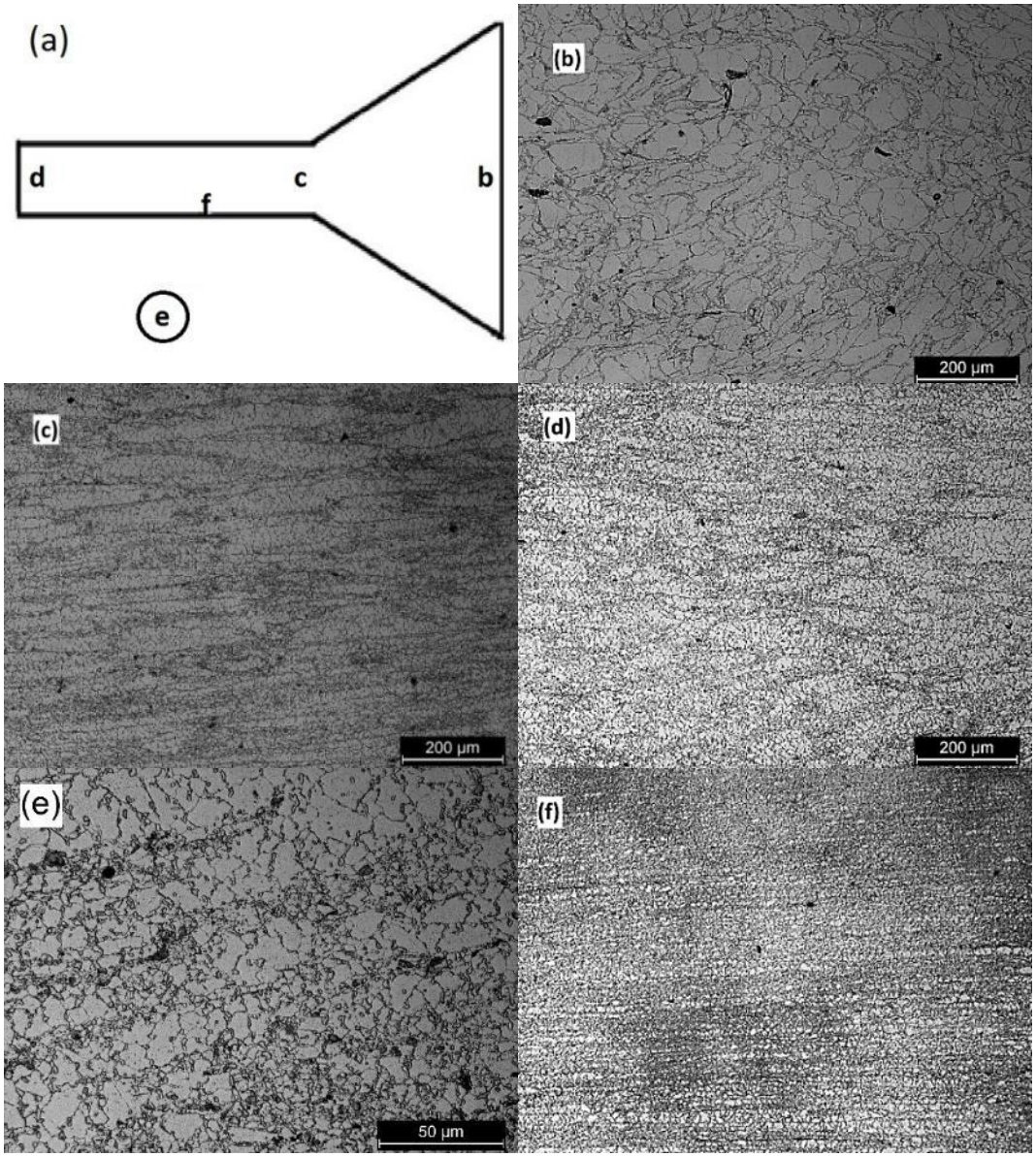

Fig. 5.21 - Microstructural evolution on sample 380-05 at the points indicated in figure (a), being the fig (e) the amplified microstructure of region "d".

Fig. 5.22 shows the microstructure evolution for sample 380-20, the one produced at high temperature and high ram speed. The region "b" presents a microstructure very similar to the preform. In both regions "c" and "d", the oxide mesh is still present and aligned with the extrusion direction. Fig. 5.22 (d) shows that the material is quite homogeneous in the core, but few coarse grains are present, due to the lack of time to the material to recrystallize. In Fig 5.22 (e), the region "d" is seen in more detail, where is possible to notice that the grains are equiaxed and thus recrystallized. The outer region of the sample (region "f") shows a finer microstructure and some cracks on the very border of the extrusion.

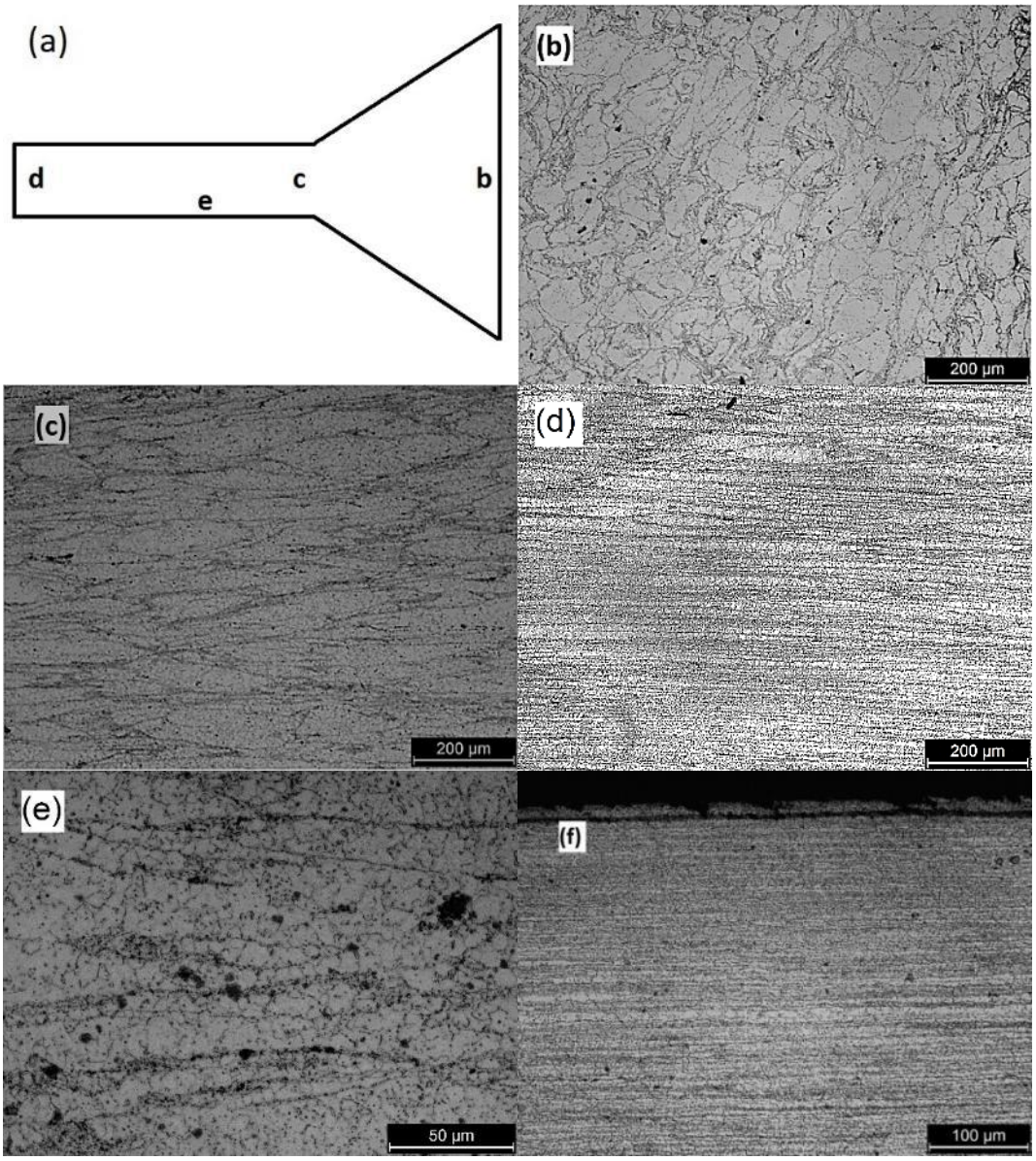

Fig. 5.22 - Microstructural evolution on sample 380-20 at the points indicated in figure (a), being the fig (e) the amplified microstructure of region "d".

In general, the average grain size decreases with the increasing of the strain rate and decreasing of the working temperature. The relation that summarizes this behaviour is the Zener-Hollomon parameter. Within the present study, the finer grain size in the core of the rod was found in the extrusion 330-20 and the average grain size was 4 µm where the larger grain size was found in the 380-05 sample (17.5 µm). The typical recrystallization temperatures for Mg alloys is between 250 and 400 °C, which is satisfied on all extrusion tests. The relationship between the Zener-Hollomon and the grain size is shown on Fig. 5.23 and it is given quantitatively by:

$$\ln d = 6.5 - 0.21 \ln Z \quad (24)$$

It should be noted that the ranges for d and Z in the present study are very narrow, thus the uncertainty is higher. However, when compared with the study presented by Chang et al. [70] using more than 20 different sets of data, the obtained that for the extrusion, the relationship of d and Z is

$$\ln d = 6.0 - 0.17 \ln Z \quad (25)$$

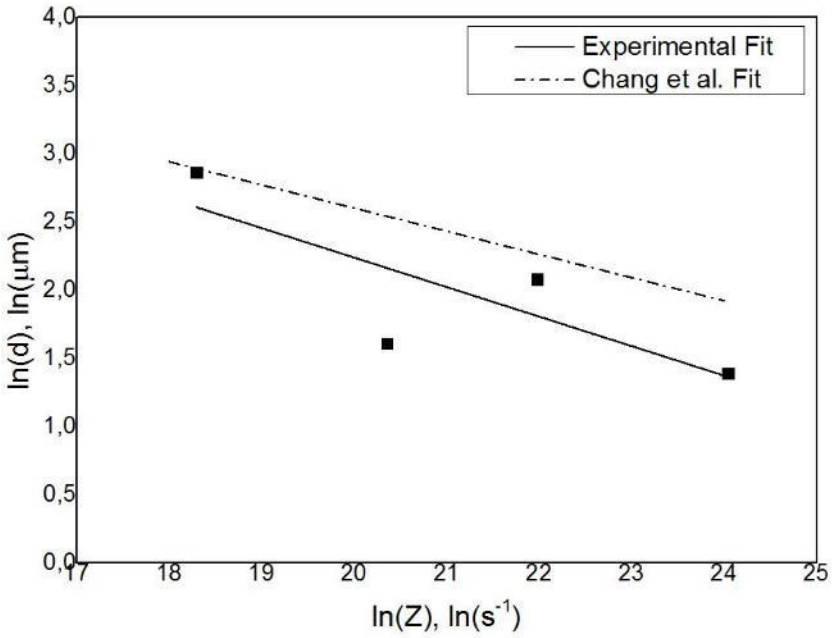

Fig. 5.23 – Plot of the relationship between grain size and Zener-Hollomon parameter.

The relationship found is in total accordance with the eq. (22) presented in the beginning of this section. If $[Z].d^p = constant$, then is possible to affirm that

$$d^p = \frac{C}{Z} \rightarrow \ \mathrm{d} = \left(\frac{C}{Z}\right)^{\frac{1}{p}} \rightarrow \ \ln d = \frac{1}{p}\ln C - \frac{1}{p}\ln Z \quad (26)$$

Being C a constant, d the grain size, p the grain size exponent and Z the Zener Hollomon parameter. By this approximation, the value of p is 4.76.

The rod extrusion tests performed with the long cycle preforms showed many interesting aspects. At first, the expected recrystallization with small grain size is present, which is a good result regarding the mechanical and

corrosion properties. Several works have studied the grain refinement and the influence of the temperature and strain rate on the process [57], [59], [71], [72], many of them achieved similar grain sizes, but the extrusion ratio was usually much higher than the 6.25 applied on this study. The fact that instead of starting with an as-cast or as-rolled material we used the SPS process to prepare the preform may be the responsible to achieve finer microstructures.

5.2.3. Relationship between grain size and microhardness

Fig. 5.24 shows that in every sample, DRX took place, leading to the formation of fine and equiaxed grains. However, the grain size is not uniform on the cross section, as reported in section 5.2.1. The grains close to the surface of the extruded bar are much smaller than those at the centre of the rod. In Table 5.3 the average grain sizes of the materials under study at the surface and at the centre of the extruded rods are listed. In the same table, the results of the microhardness tests are also included. As expected, the microhardness decreases with the grain size, d. As shown in Fig. 5.25, the correlation obeys the Hall-Petch equation, i.e., microhardness increases with $d^{-1/2}$.

Table 5.3 – Relationship between average grain size and microhardness on extruded samples.

Sample	Average grain size at the centre, μm	Average grain size at the surface, μm	Microhardness at the centre, HV0.1	Microhardness at the surface, HV0.1
330-05	5	3	103	118.5
330-20	4	1.5	112	127
380-05	17.5	7	95	98
380-20	8	4	98	105

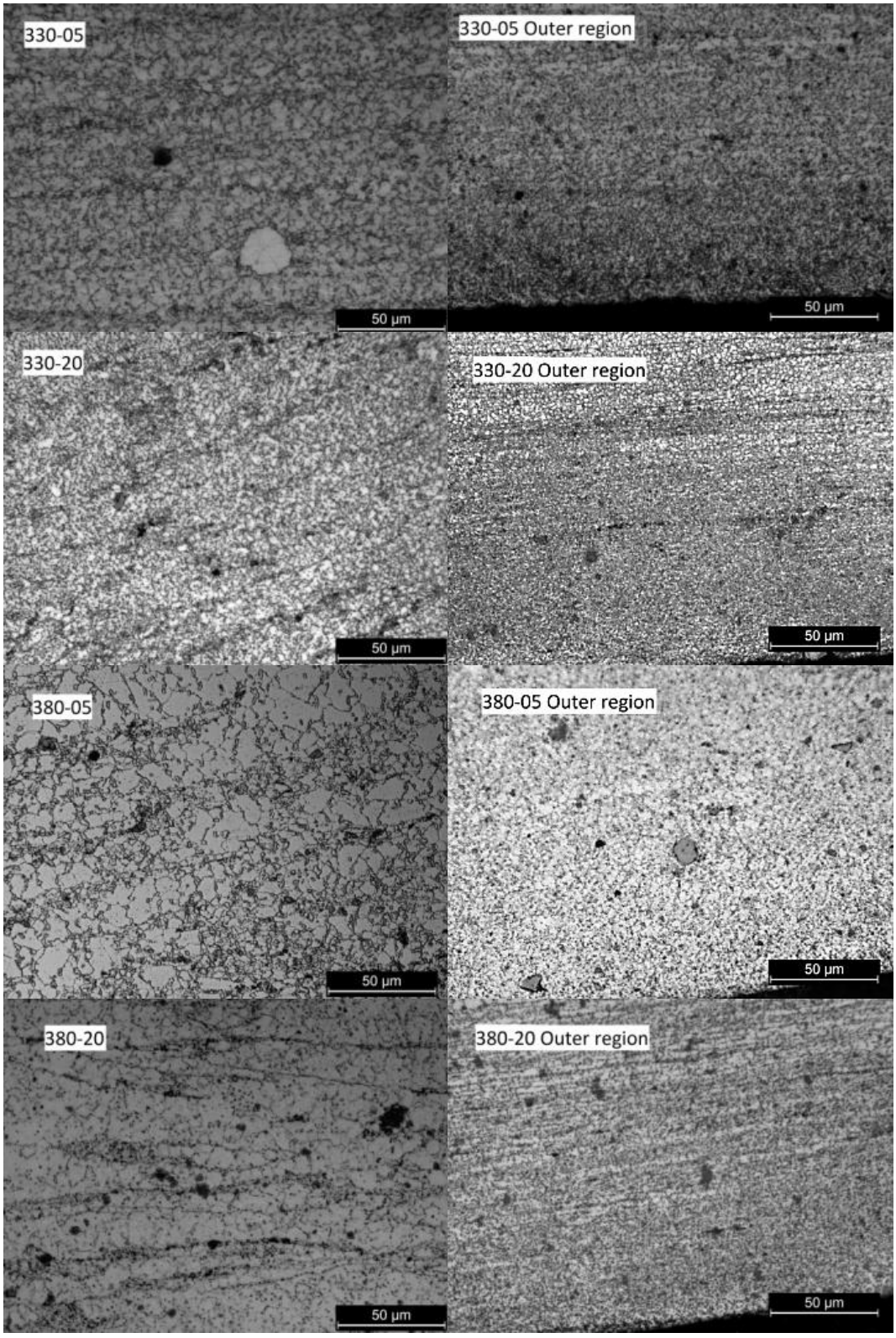

Fig. 5.24 - Grain size after extrusion in inner and outer region.

The correlation between mechanical properties and grain size is defined by the following Hall-Petch equation [73].

$$\sigma = \sigma_0 + K_v d^{-1/2} \quad (27)$$

where σ is the yield strength, K_v is the Hall-Petch slope and d is the grain size. According to the literature, this relation is also valid for the microhardness correlation with the grain size [73]. Fig. 5.25 shows the linear correlation between microhardness and $d^{-1/2}$. The correlation is according to the eq. (27) and HV_0 can be considered 77.45 and K_v 62.37. With a r-square of 0.91. These values are in agreement with those described in the literature [70], [74]. The difference between the two fits in Fig. 5.25 is because Chang et al. used AZ31 in his studies, which has a lower mechanical strength. Nevertheless, the slope of the fit is quite the same, showing that the influence of the grain refinement on the mechanical properties is similar.

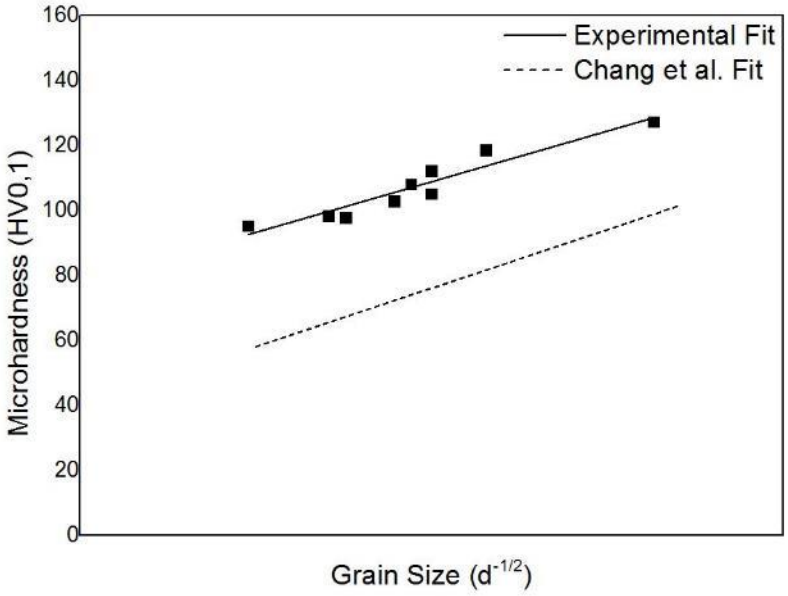

Fig. 5.25 - Correlation between recrystallized grain size and microhardness [74].

This difference in the grain size between the surface and the centre of the extruded rod was also observed by Murai et al. [5] and may explained by considering the greater surface plastic deformation at the die land during extrusion due to friction. Such an increase in strain at the surface was also responsible for the formation of a surface crack in the material extruded at 330 °C and at the highest strain rate here investigated (Fig 5.20 (f))

5.2.4. γ-phase content on AZ91 rod extrusion

In order to analyse the influence of the extrusion parameters on the γ-phase dispersion, a metallographic analysis was performed using HF to etch the material and the microstructures are shown on Fig 5.26. It is possible to notice that for the extrusions made at the lowest temperatures and lowest strain rates, the quantity of γ-phase tends to be higher. This can be explained by looking at the Mg-Al phase diagram (Fig. 2.5). The line that divides the α and α+γ regions intercept the AZ91 composition at a temperature of about 350 °C, which means that any process that occur below this temperature is inducing the formation of γ-phase, while above this temperature, it is inducing the solubilisation of the γ-phase into the α matrix. Thus, for the extrusion performed at 330 °C, the formation of the γ-phase is occurring during the process, and the 380 °C extrusions are dissolving this phase into the matrix. The role of the strain rate is related with the ram speed and thus with the time that the material spend at the experiment temperature. As higher is the time (lower strain rate), more γ-phase is formed, in case of 330 °C extrusion, or more γ-phase is being dissolved, in case of extrusions performed at 380 °C.

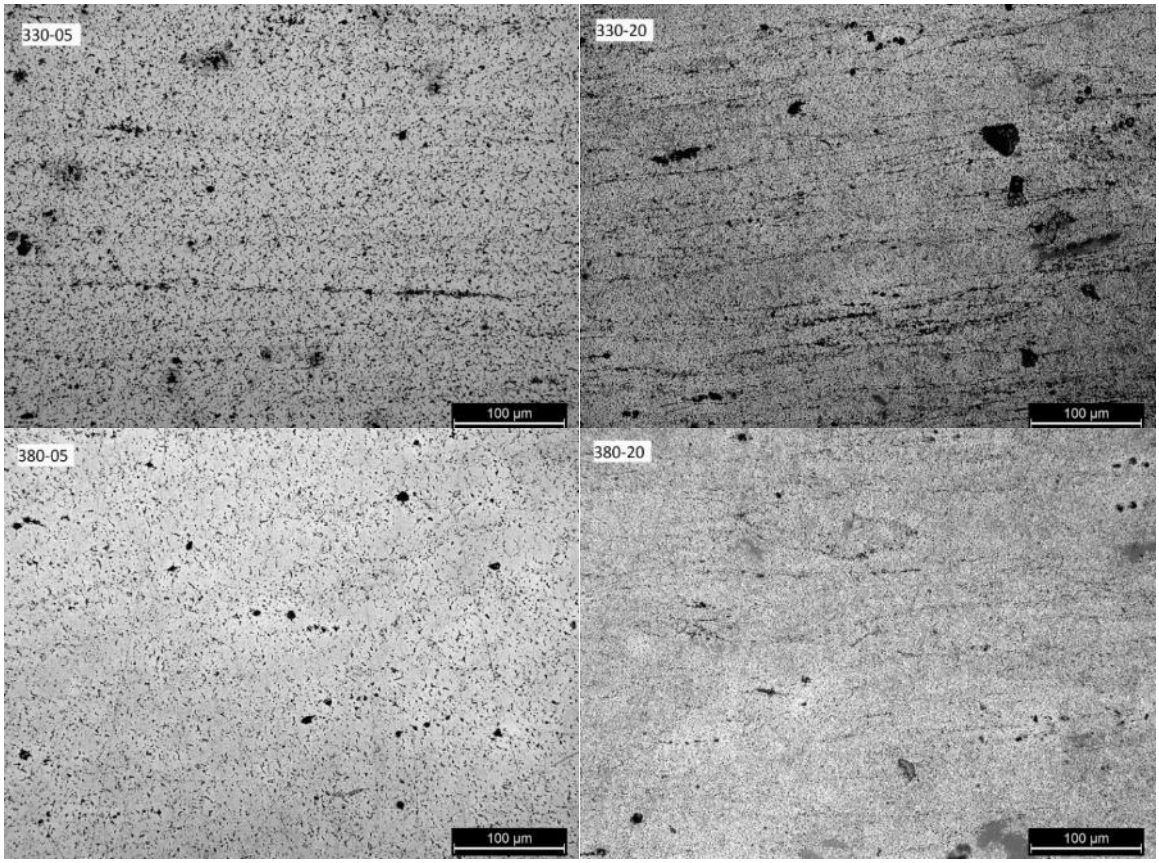

Fig. 5.26 – Micrographs showing the γ-phase on extruded samples.

In addition, ESEM analysis using BSE and EDXS to identify the phase content was performed, the observations are shown on Fig. 5.27. It is possible to identify 3 different phase: the first one is the matrix, the second one is a light grey phase identified as Al_8Mn_5 and the third one is the γ-phase $Mg_{17}Al_{11.5}Zn_{0.5}$. γ-phase a stoichiometric composition of $Mg_{17}Al_{12}$. It was showed that the same phase is also formed on ternary alloys with ratio larger than 3:1 between Al and Zn (such as AZ91). In this case, instead of forming a new phase, the structure of the so-called γ-phase is maintained with substitutional Zn, having a stoichiometric composition of $Mg_{17}Al_{11.5}Zn_{0.5}$ or $Mg_{17}(Al,Zn)_{12}$ [75].

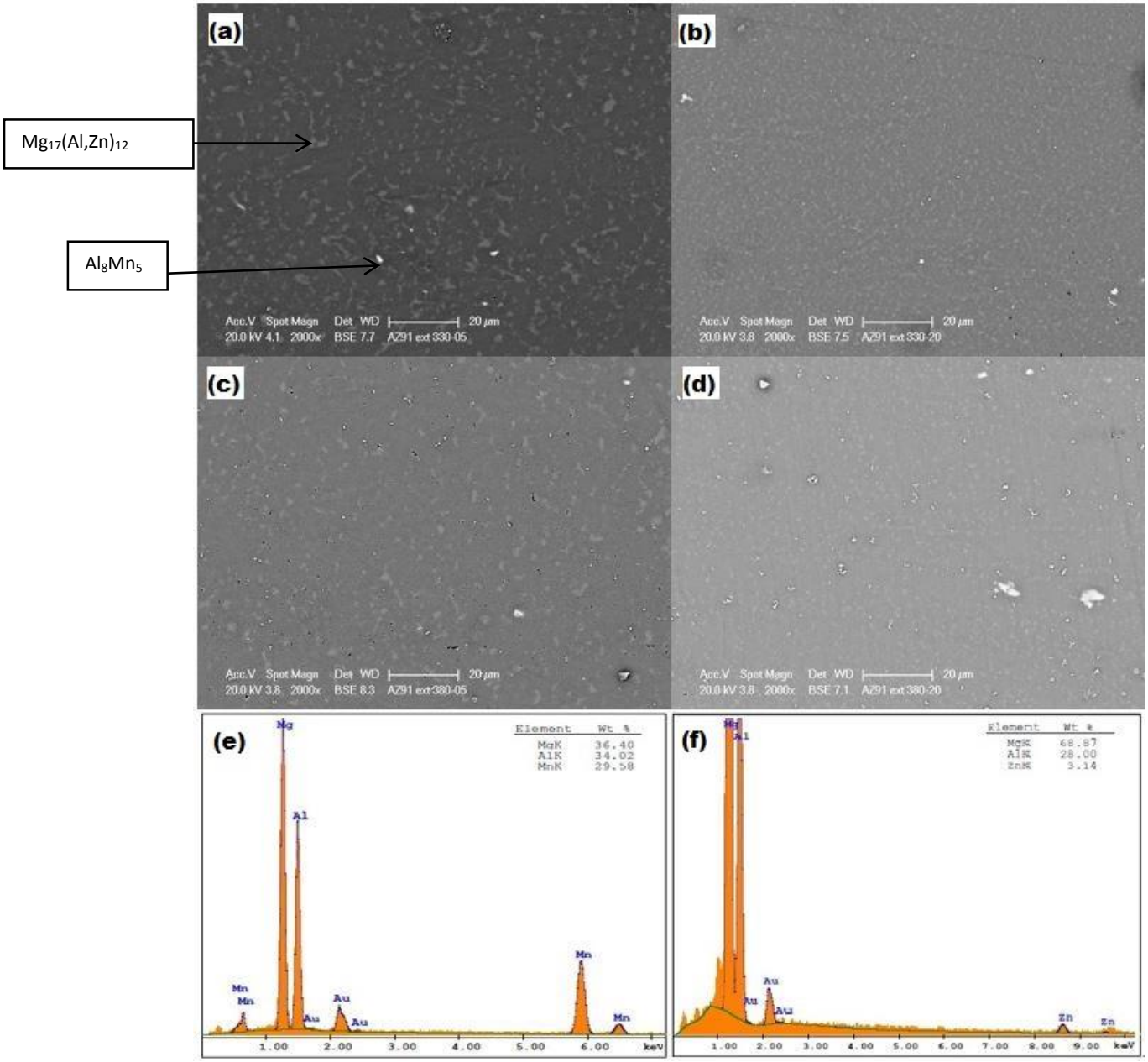

Fig. 5.27 - ESEM image on BSE mode showing the γ-phase on extruded samples and EDXS of light and grey phases. (a) 330-05 (b) 330-20 (c) 380-05 (d) 380-20 (e) EDXS – Al_8Mn_5 (f) EDXS – $Mg_{17}Al_{11.5}Zn_{0.5}$.

XRD analysis using Rietveld method was also used to measure the phase content on each step of the process, and the results are listed in Table 3. According to the results, the adopted SPS cycle was effective to decrease the possibility to form liquid phase during the process and also to improve the quality of the material by a noticeable reduction of γ-phase content. Even after the extrusions, the initial amount of γ-phase is not reached.

To performs the extrusion at 380 °C is the best alternative regarding the γ-phase. Also from the Table 5.4, is possible to notice that even after the extrusion, the oxides present initially at the powder surface remained in the material, but they do not affect the microstructure, since the continuous mesh present on the SPS samples was effectively broken by the plastic flow during extrusion.

Table 5.4 – Phase content on each extrusion condition.

	AZ91 Powder	AZ91 SPS	330-05	330-20	380-05	380-20
Mg Matrix	82%	95%	86%	88%	89%	89%
γ-phase	17%	4%	13%	11%	10%	10%
MgO	1%	1%	1%	1%	1%	1%
Al_8Mn_5	Residual	Residual	Residual	Residual	Residual	Residual

5.2.5. Analysis of the extrusion process

On section 5.1.5, the results of the hot compression tests were used to predict the extrusion load. In some cases the predicted extrusion loads were quite different from the measured loads. Due to these differences, after the extrusion tests, the same equations were used to calculate the effective friction coefficient from the recorded extrusion loads. Fig. 5.28 shows the hot compression curves recorded at 330 and 380 °C and at an average strain rate of 0.002 and 0.056 s^{-1} simulating the forces induced on the samples submitted to extrusion at the speeds of 0.5 and 20 mm/min respectively.

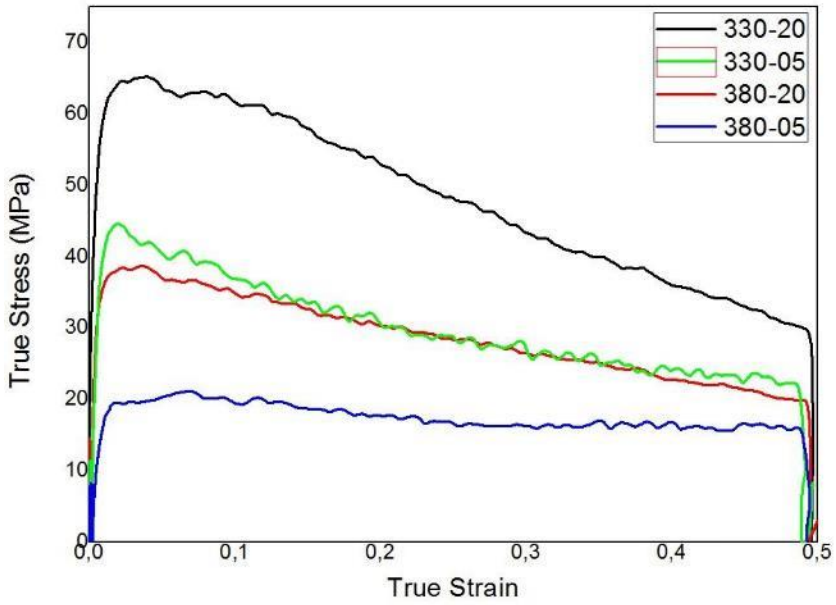

Fig. 5.28- Compression curves at 330 and 380 °C at strain rate of 0.002 and 0.056 s^{-1}.

As described in section 5.1.5, the link between flow stress under hot compression and the extrusion behaviour of the material is present on literature [59]. The friction coefficient, μ, can be described as:

$$\mu = \frac{D_o}{4L}\left(\frac{F_{ext}}{A_o p_o} - 1\right) \quad (28)$$

Table 5.5 presents the measured flow stresses, the predicted extrusion load (considering a friction coefficient of 0.3), the actual extrusion load and the calculated friction coefficient. The correct friction coefficient for the extrusions performed at 330 °C is smaller than that reported in the literature. However, the friction coefficient for the extrusions performed at 380 °C is higher than the literature values. This is because the lubricant used in the extrusion test is set to work at temperatures up to 400 °C. Nevertheless, in the extrusions performed at 380 °C, the upper part of the sample is at slightly higher temperatures and can exceed 400 °C. This overheating impeded the action of the lubricant, especially at lower ram speeds, where the time allowed for lubricant degradation is longer. It is evident the need of finding a suitable lubricant for the application above 380 °C.

Table 5.5 – Recorded flow stress, recorded load during extrusion and estimated friction coefficient.

Sample	σ_e (MPa)	Calculated F_{ext} (kN)	Measured F_{ext} (kN)	Calculated μ
330-05	45	71	37	0.20
330-20	65	48	54	0.20
380-05	20	40	35	0.52
380-20	37	22	50	0.39

5.2.6. AZ91 Tube extrusion

The tube extrusion was performed directly from the SPS preform. A hole was drilled in the centre of the sample with 2.1 mm of diameter, 0.1 mm larger than the needle installed on the plunger. The extrusion ratio was 8, being the preform with the diameter of 10 mm, the external diameter of the extruded tube 4 mm and inner diameter of the tube 2 mm. Tests were performed using the preforms produced by the long cycle at the 380-05 condition. The tube extrusion was performed at 380 °C with the ram speed of 0.5 mm/min, which corresponded to strain rates of 2.44 x 10^{-3} evaluated according to eq, (14), using the adjusted value for R' of 24.56, calculated from eq, (8).

Since R' is almost 4 times R, for the tube extrusion tests, it was decided to perform the tests on the 380 °C condition first at the lowest possible speed (0.5 mm/min). However, even at the less severe condition, the extrusion load increased to values up to 80 kN, not allowing any change in the process parameters. Unfortunately, several needles were broken during extrusion, due to the lack of lubrication in the needle-specimen surface. The flow of the material was forcing the needle too much, and this is another reason for not increasing the strain rate or decreasing the temperature. Fig. 5.29 shows the external appearance of the extruded tube.

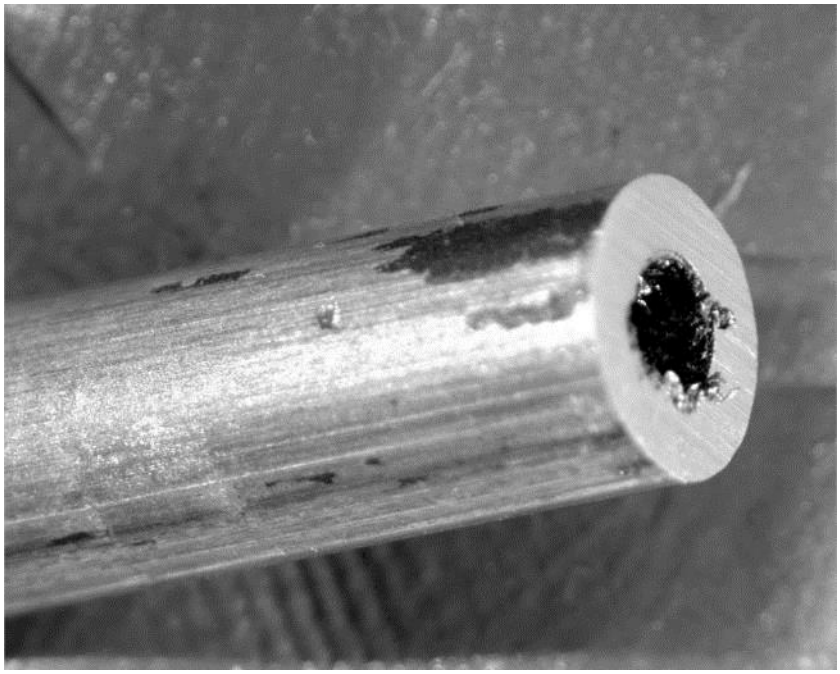

Fig. - 5.29– AZ91 tube general view

Fig. 5.30 shows the microstructure of the extruded tube. The microstructural characterization showed that the extrudate contains some non-recrystallized regions, already seen in the rod extrusion samples. The difference on the grain size between the core and the outer region is no longer present. However, the inner part of the tube, the one in contact with the needle, presented some micro-cavities. The lack of lubrication induced a very high level of shear on this particular region and the micro-cavities were formed by plastic shear around the γ-phase precipitates.

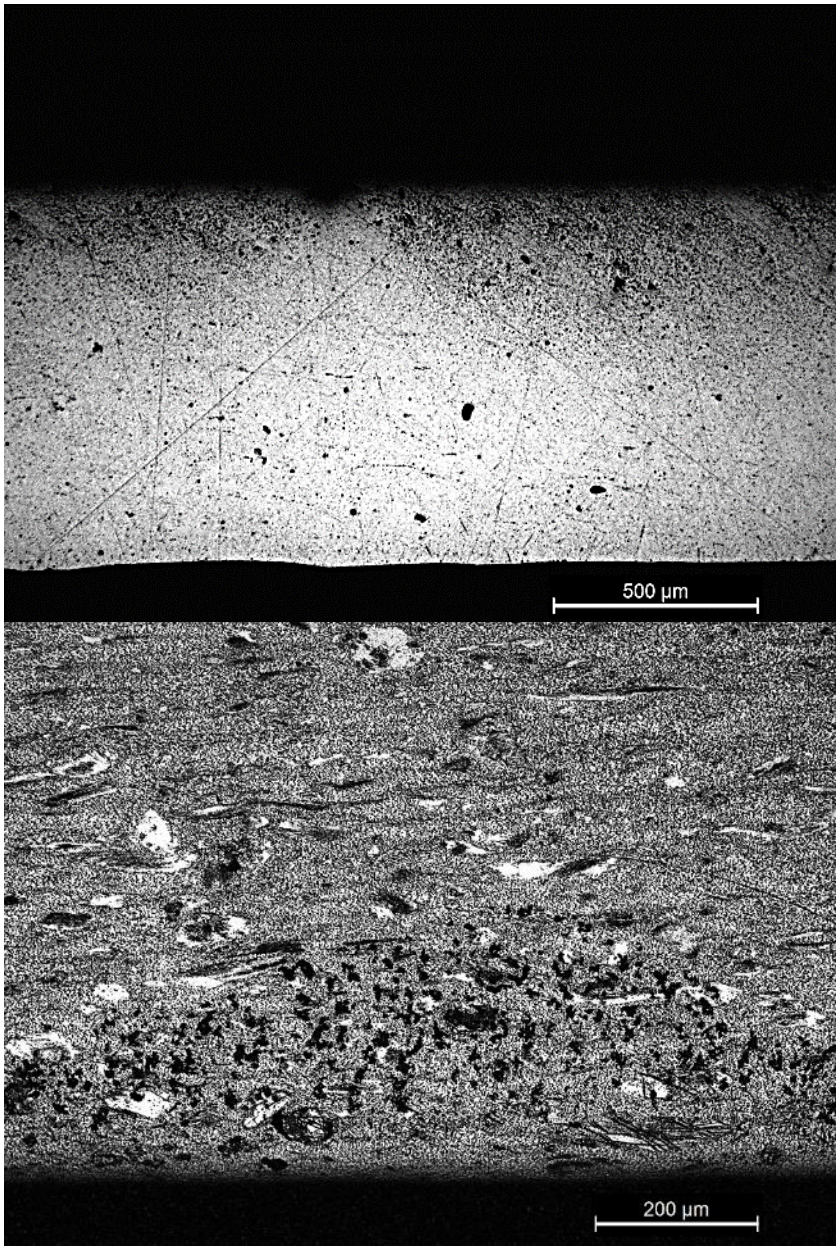

Fig. 5.30 – General view (top) and microstructure evolution on inner region (bottom) of AZ91 tube extrusion.

Since the influence of the friction is very relevant for the extrusion, a simple calculation was performed to have an approximate idea of the actual friction coefficient during the tube extrusion. The extrusion load was found to be 80 kN. The information of flow stress is not available, since the hot compression did not simulate the same conditions for the tube extrusion. Therefore, we made a reference to the relationship of Zener-Hollomon and the peak flow stress, displayed in Fig. 5.31.

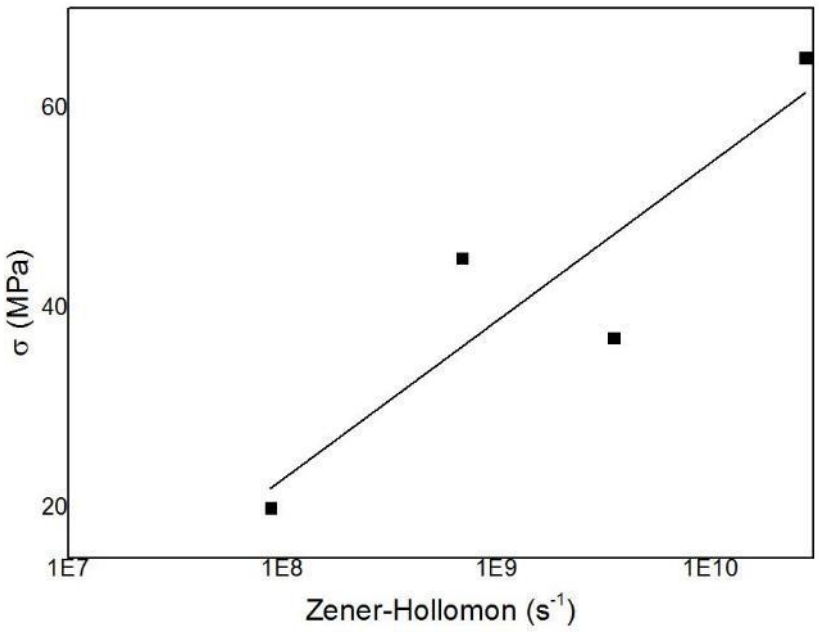

Fig. 5.31 - Relationship between Zener-Hollomon parameter and peak stress.

The equation that better fits the data is $\sigma = 6.88 \ln Z - 130.90$, which would predict a flow stress of 25.8 MPa for the same conditions of the tube extrusion. It was possible to calculate the friction coefficient of the tube extrusion using the same method already demonstrated on section 5.2.5., resulting in a friction coefficient of 1.14.

It is quite evident that the result is not satisfactory since it appears to be high. However, it gives an idea of the large friction between the needle and the sample. The main problem with the lubrication of the tube extrusion tests is that the lubricant is liquid, and thus does not remain on the top of the preform before the onset of extrusion, but it leaks through the hole. A solution it was to change the liquid lubricant, adopting a paste lubricant, which improved the quality of the inner part of the tube, as can be seen on the machined tubes on Fig. 5.36.

Fig. 5.32 shows the detailed microstructure of the core region of the tube. It is possible to notice that the grains are equiaxed, thus leading to a conclusion that dynamic recrystallization was present. The average grain size is 4.5 μm. The microstructural results are in a very good agreement with the results obtained by the core microstructure on the 330-20 rod extrusion.

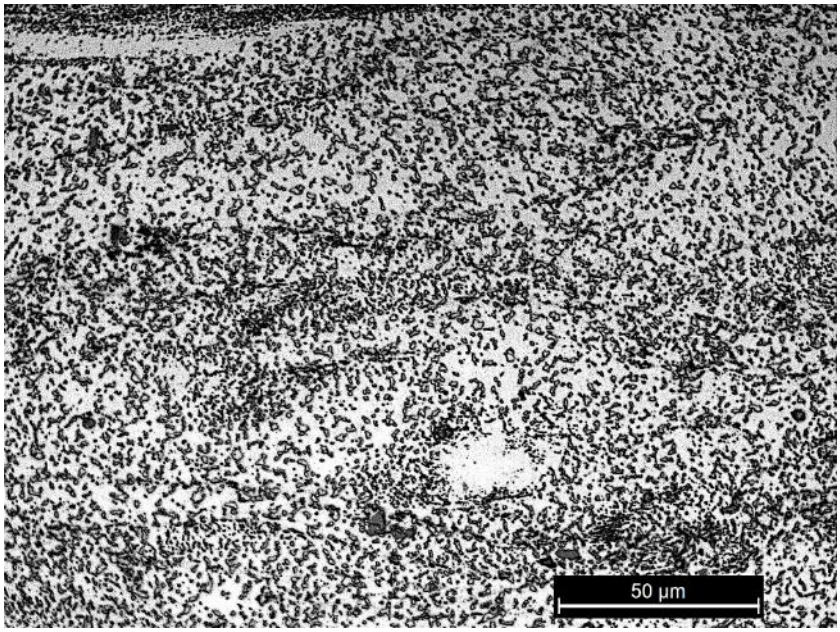

Fig. 5.32 – Microstructure on inner region of AZ91 tube extrusion.

5.2.7. Pure Mg extrusion

Despite the fact that on SPS the pure Mg showed at both temperatures a very low degree of sintering, and a high quantity of pores, the extrusion test were performed anyway since the defects present on the SPS preforms could be repaired by extrusion.

The plastic flow of the material into the die is very likely to break all the oxides on the particle boundaries and at high temperatures allow the material to complete the sintering process. The hot compression tests and the SPS showed that the recrystallization did not occur on the pure Mg samples at these conditions.

It was chosen to proceed with the extrusion test for pure Mg at the conditions of high speed (20 mm/min), in order to try to break the oxide layer on grain boundaries, at the temperature of 330 and 380 °C. The extrusion tests showed that for Pure Mg, the load of extrusion is lower than for AZ91, as predicted by the hot compression tests. Table 5.6 shows the recorded values of extrusion load, the average recorded flow stress and calculated friction coefficient, based on the same equation presented to calculate the friction

coefficient for AZ91. The friction coefficient was quite similar to these calculated during the extrusion of AZ91.

Table 5.6 – Recorded flow stress, recorded load during extrusion and estimated friction coefficient.

Sample	σ_e (MPa)	F_{ext} (kN)	μ
330-20 Mg	38	38	0.27
380-20 Mg	22	30	0.41

For the pure magnesium rod extrusion, the parameters changes did not show to have any influence on the final grain size; this behaviour is expected, since there are few barriers to stop grain growth caused by the heating during extrusion. In Fig. 5.33 is possible to notice that the grain size after both extrusions is similar and not much different from the SPS sample. The only change is the elongation of the grains. The original powder is still recognized, showing that the continuous oxide layer is still present and thus the mechanical behaviour is harmed.

In literature is possible to find some grain refinement on pure Mg using the extrusion process; however, the temperatures involved are usually much lower. For example, Somekawa et al. [76] achieved grain size of 55, 5 and 1 μm extruding pure Mg at a temperature of 180, 94 and 90 °C respectively. It is clear that the Zener-Hollomon parameter is far from the values of the extrusion tests performed on this work.

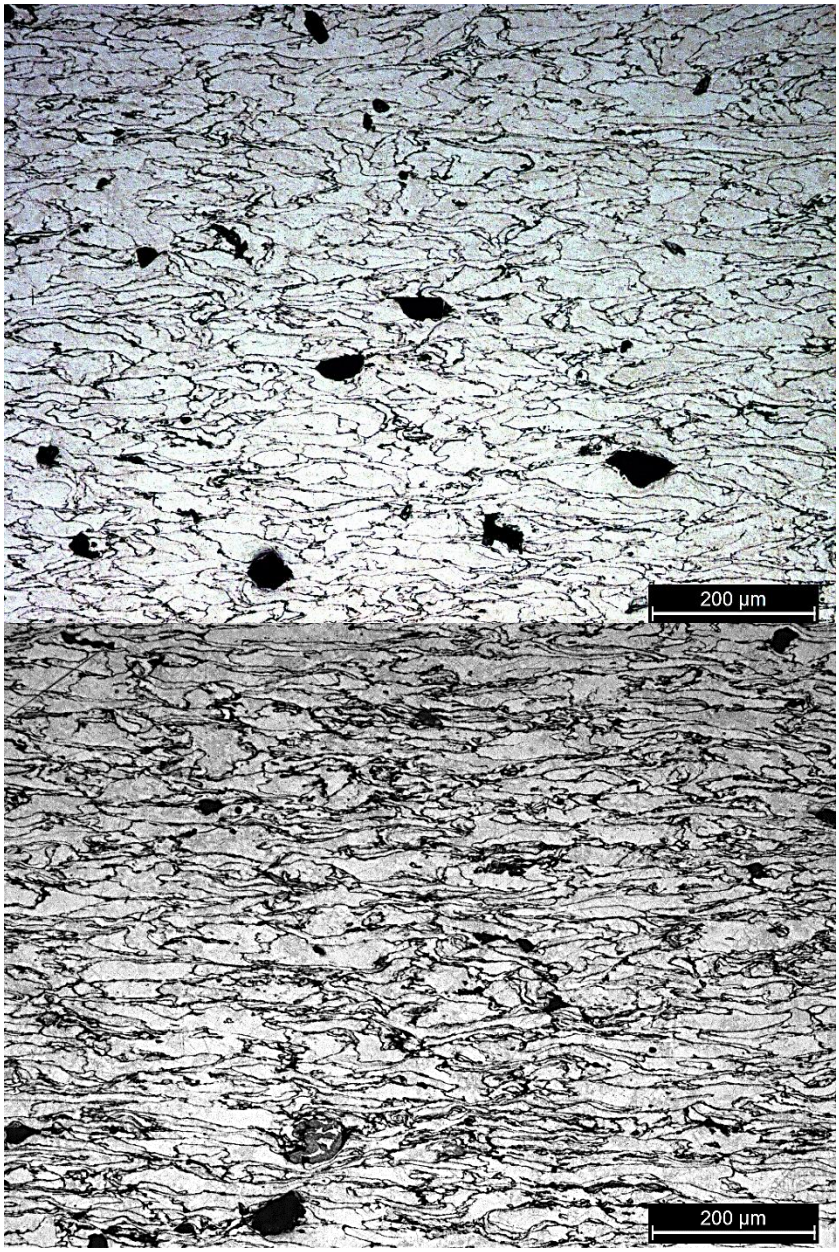

Fig. 5.33 - Pure Mg microstructures after extrusion 330 °C (top) and 380 °C (bottom).

As a last attempt to use the pure Mg powder to produce the stent, the tube extrusion was performed at the same conditions as for the tube extrusion of AZ91. At 380 °C and at a ram speed of 20 mm/min, resulting in a strain rate of 2.44×10^{-3} s^{-1}. Fig. 5.34 shows the external appearance of the extruded tube. It seems that no cracks or important defects are present.

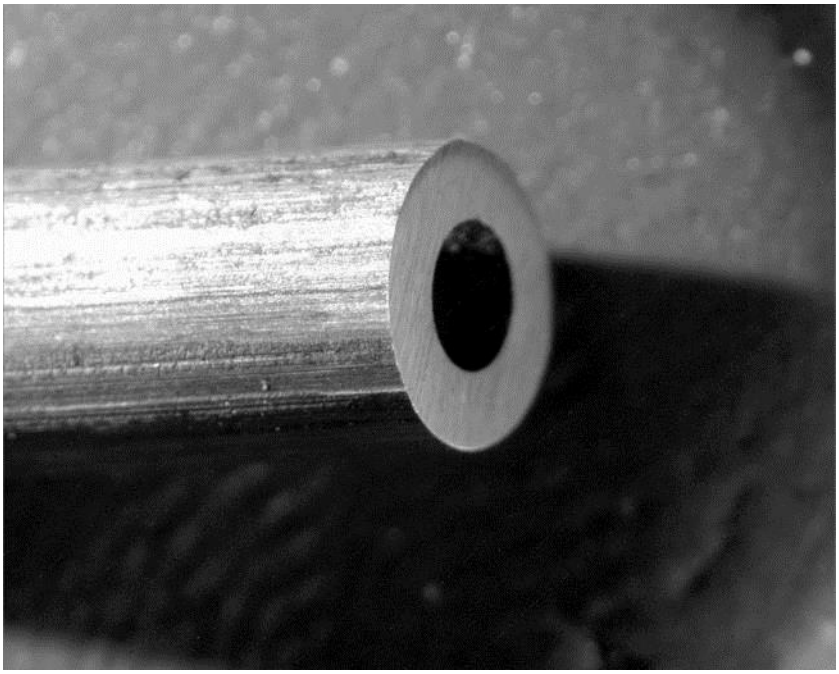

Fig. 5.34– Tube of pure Mg extruded at 380 °C at a strain rate of 2.44 x 10^{-4} s^{-1}

Despite the external appearance of the tube, after optical microscopic analysis showed on Fig. 5.35, several cracks are spotted especially in the inner region. On the AZ91 tube extrusion the same region of the sample suffered with many micro-cavities, caused by the higher local strain and the shear stress due to the high friction between the sample and the extrusion needle. The shear caused by the lack of lubrication showed to be very damaging to the pure Mg tube. The low degree of sintering, with the higher strain rate lead to the formation of these cracks. In some parts, the inner wall of the tube was completely broken into pieces and thus the further processing is unviable.

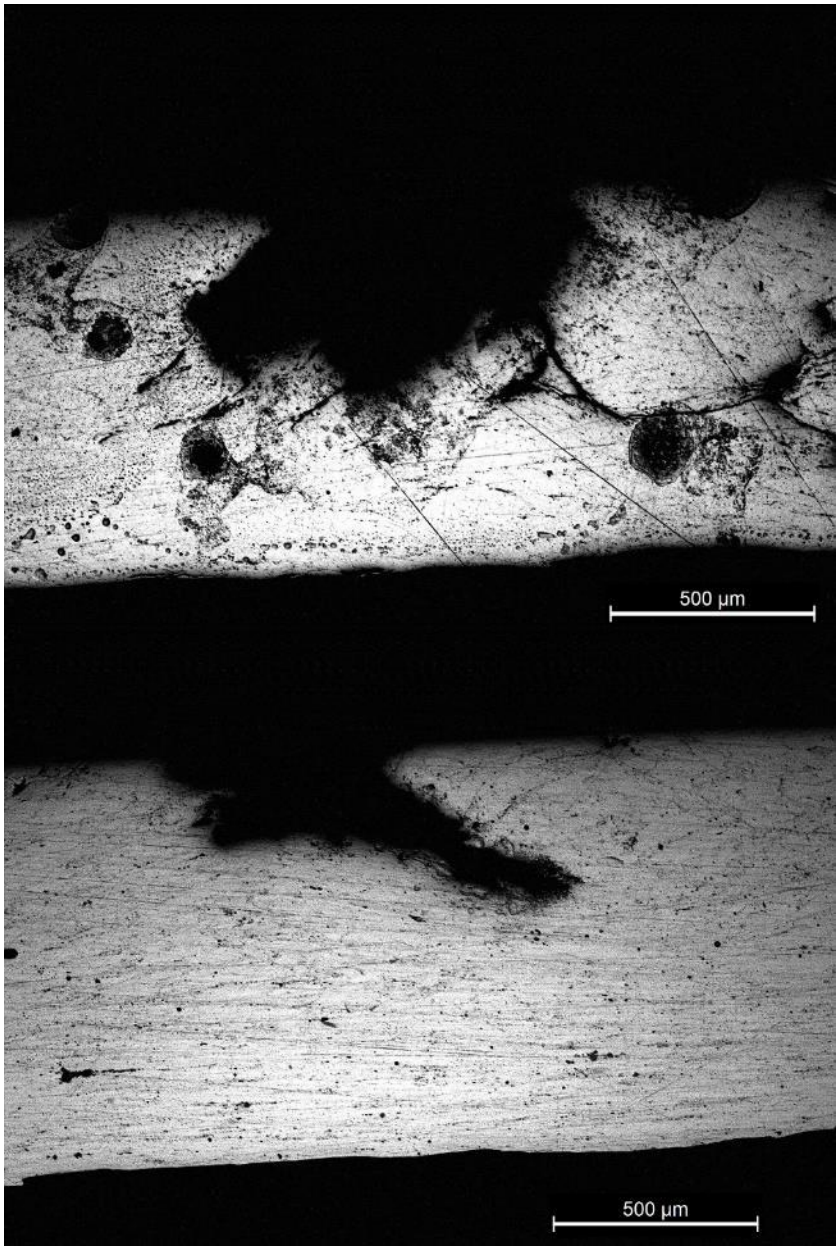

Fig. 5.35 - Micrograph of pure Mg SPS after tube hot extrusion at 380 °C.

5.3. Machining and Laser Cutting

5.3.1. Machining of AZ91 Tubes

After extrusion, the tubes were submitted to machining by turning. In Fig. 5.36 (a), it is possible to notice that the visual appearance of the tube is quite satisfactory. However, it is not perfectly centred after machining. Fig. 5.36 (b)m the interface between before and after machining is showed and is possible to notice that the quality of the inner part of the tube is good, not presenting the previous micro-cracks discussed in section 5.2.6. This is due to the change of lubricant, replacing the liquid lubricant with a paste. The machining process did not affect the microstructure. It is possible to observe on Fig. 5.36 (d) that the microstructure remained similar to before the cutting and at the tube surface, the machining did not induce noticeable plastic deformation or any microstructural change.

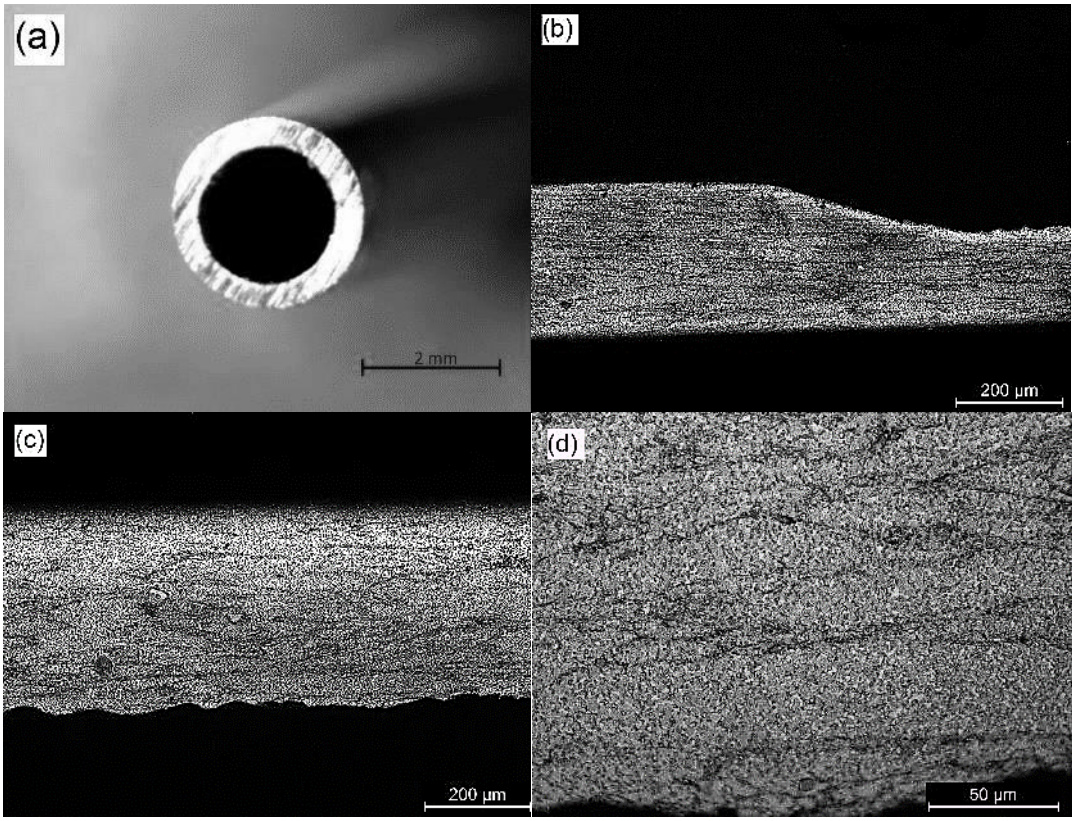

Fig. 5.36 – (a) General view of the machined tube, (b) interface between before and after machining, (c) general microstructure view and (d) microstructure of the machined tube.

Fig. 5.37 shows the measurement of the machined tube using a Coordinate Measurement Machine (CMM). It was found that the external diameter after machining is 2.72 ± 0.07 mm and the inner diameter is 2.00 ± 0.007 mm.

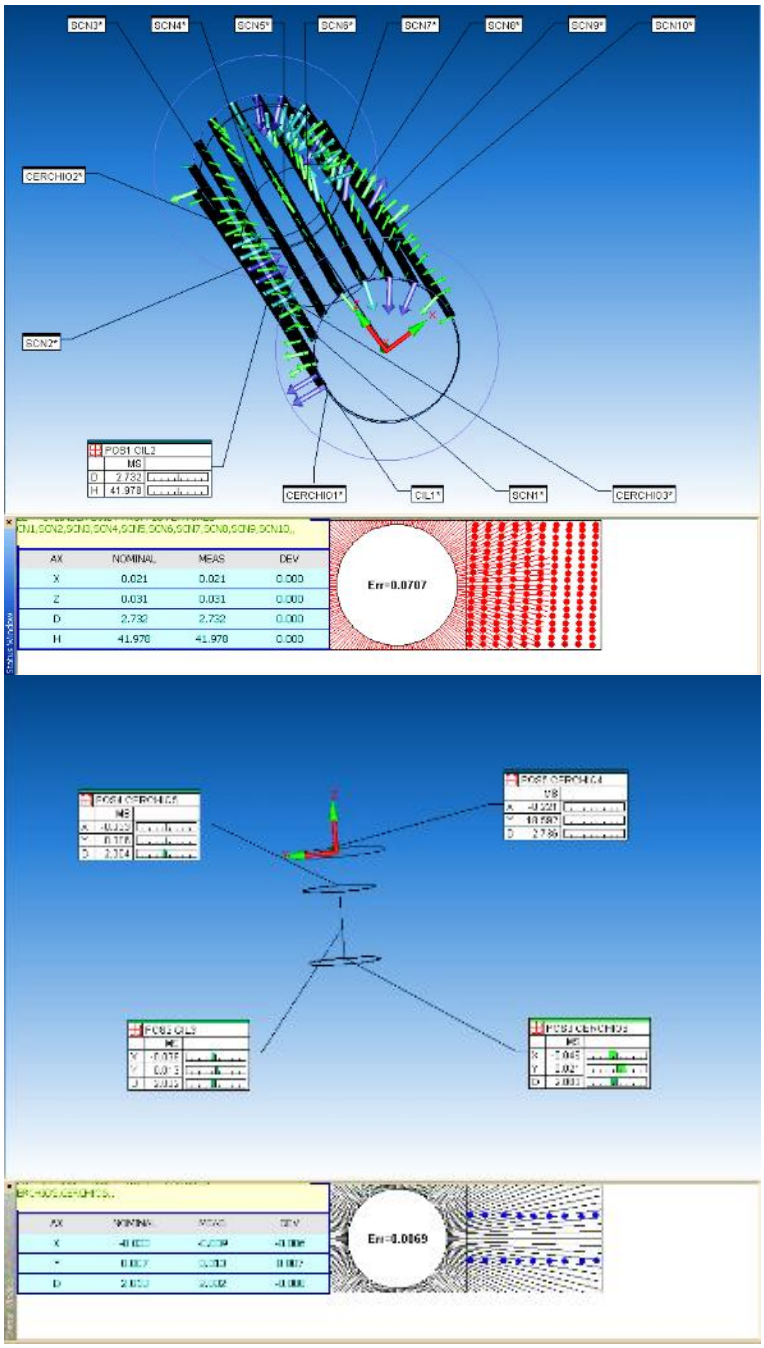

Fig. 5.37 – Measurement of the machined tube on CMM.

5.3.2. Laser Cutting of AZ91 Tubes

The control of the dimensional characteristics of the thin-wall tube after manual machining is very difficult. The ideal would be to perform the hot extrusion and then perform at least 4 steps of cold drawing, as described by Fang et al. [77]. Since the proposed work is to evaluate the viability to produce stent precursors from starting from Mg powders, the cold drawing was not performed before the laser cutting due to time and resources limitations.

Fig. 5.38 displays the CAD model of the desired stent along with the laser cut stent. Even if the geometry of the tube sample was not favourable, it was possible to cut some stents in good shape.

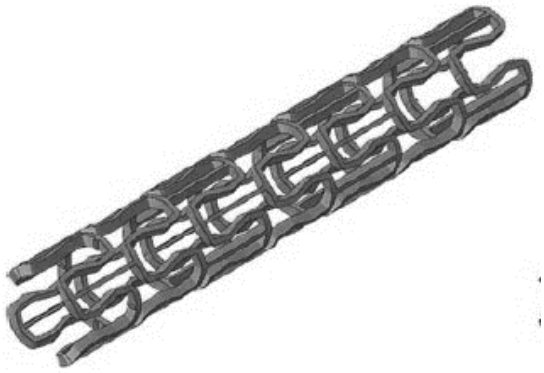

Fig. 5.38 - Magic CAD model (Biotronik, Berlin, Germany).

Fig. 5.39 shows the best stent after the laser cutting, showing that if the machining is carried out with more precision, is possible to obtain from the AZ91 tube a good stent.

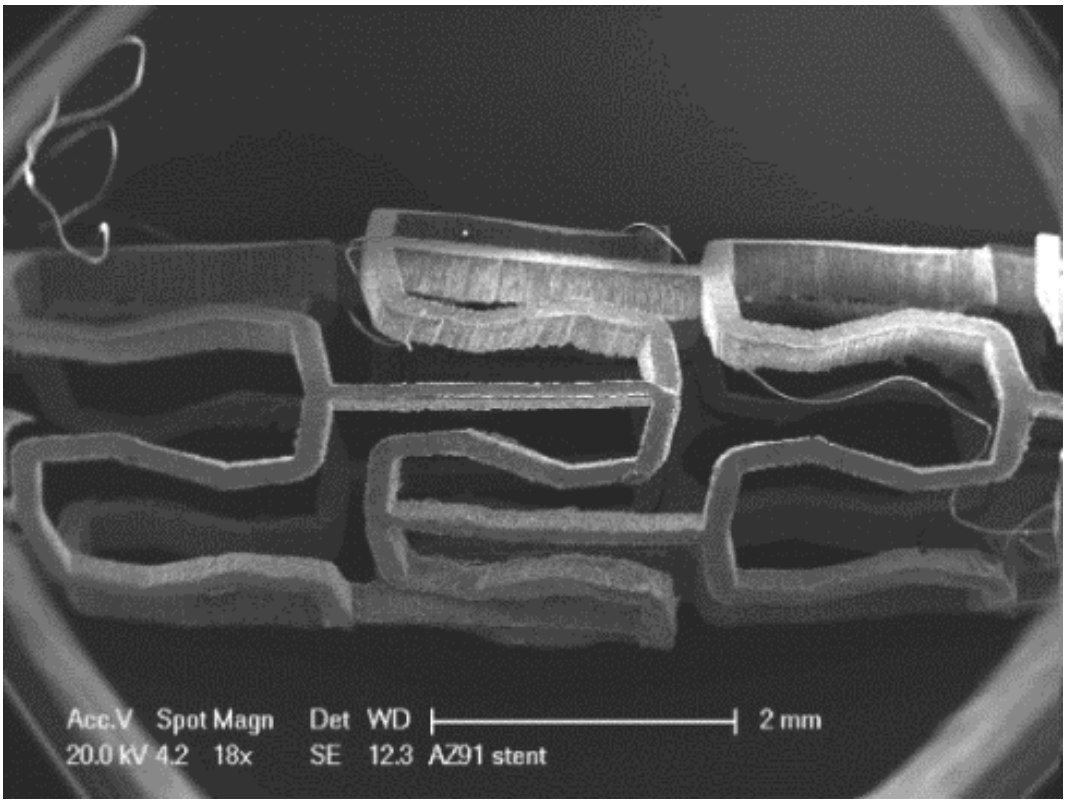

Fig. 5.39 – ESEM image of the stent precursor.

Although the machining have produced a quite good thin tube for a manual machining, the measured variance of 0.07 mm in the external diameter seems to be little regarding the external diameter, but when compared with the wall thickness of 0.36 mm, the tolerances showed to be not satisfactory. The variance of 0.07 mm in a wall thickness of 0.36 mm means 19.5% of variance. For a process so sensitive to dimensional variance, is very harmful. It is possible to notice on Fig. 5.40 some of the defects observed during the laser cutting of the tubes. Due to the variance of the wall thickness, it was very difficult to set the laser parameters, because if the cut speed was too high or the laser power to low, the thicker parts would not be cut, as seen on Fig 5.40. On the other hand, if the cutting speed is to low or the power too high, the

thinner parts of the tube can melt, of even cause big holes as seen on images.

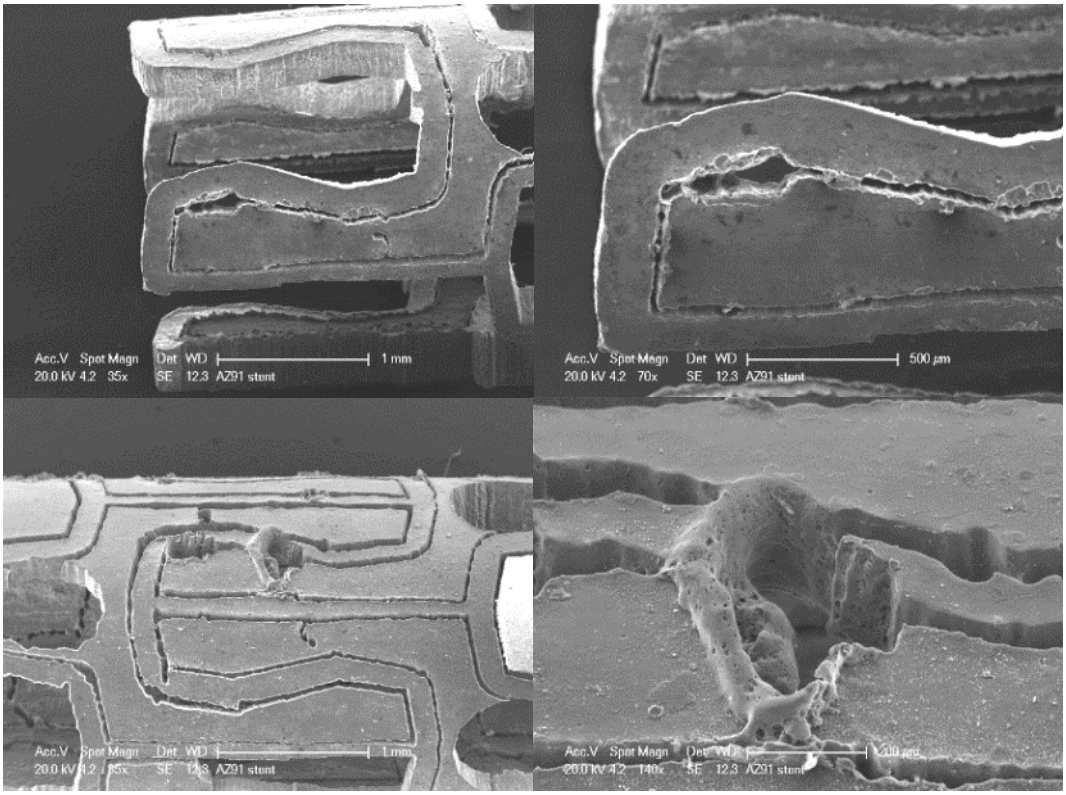

Fig. 5.40 - Stent cutting defects.

Fig. 5.41 shows the microstructure of the laser cut stent. It is possible to notice that the microstructure is very homogeneous along the tube section and that the oxide layer present in the SPS sample is almost not recognized. Some γ-phase agglomerate is present, but not as near as the levels of the SPS sample. It is possible to notice that the laser cutting did not interfere on the microstructure. The fact that the laser did not affect the microstructure can be accredited to the short pulse duration, not giving time to the material to absorb the heat caused by the cutting.

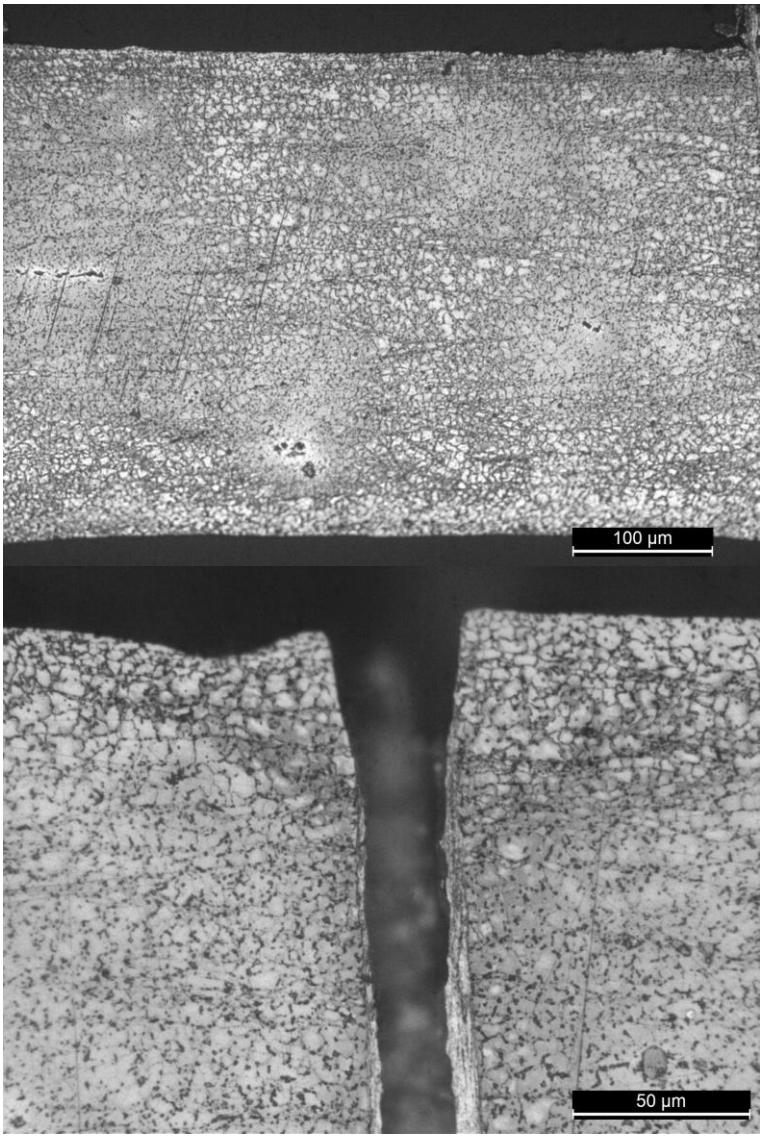

Fig. 5.41 – Microstructure of the stent after laser cutting.

Chapter VI

Conclusion

In this PhD thesis, a route to product biodegradable stents precursors from Mg-based powders was proposed. The received powders were sintered by Spark Plasma Sintering to obtain preforms that were then extruded to obtains a tube. These tubes were then machined to achieve thin wall and finally formed the stent by laser cutting. Specific hot compression tests were also performed in order to better understand the plastic deformation process occurring at high temperatures.

This process route was chosen to exploit the advantages of the PM technique, which allow to start the process with small grain size and reduce it further.

6.1. Pure magnesium

The first material investigated was the pure Mg and the main results are:

- In both temperatures of sintering, the preforms showed poor consolidation of the powders and not complete densification. This is due to the oxide layer on the surface of the particles that damages the sintering process. The temperature of sintering does not highly affect the quality of the sintered sample
- The hot compression of pure Mg preforms at a strain rate of 0.002 s^{-1} induced a high amount of interparticular cracks in both 330 and 380 °C compression tests. This means that the network of MgO served as a path to propagate the cracks on the material.
- No grain refinement was observed after hot compression of pure Mg preforms and the grain grew to the size of the original particle.

- Both rod extrusion tests showed no grain refinement. In order to achieve grain refinement, the extrusion should be carried at much lower temperatures, which would not be possible with the SPS preforms.
- The tube extrusion was carried out and again no grain refinement is present. After tube extrusion, several large cracks were found on the tube, more precisely in the needle-sample surface.

6.2. AZ91 alloy

The second material investigated was the AZ91 alloy and the main results are:

- A sintering cycle was developed aimed on avoiding the formation of a liquid phase. SPS was carried out at 470 °C, which allowed the material to consolidate properly and reduce significantly the amount of γ-phase from 17 % (in the original powder) to only 4 %.
- The hot compression was capable of induce grain recrystallization on the long cycle preform. The hot compressions performed at strain rate of 1 s^{-1} showed a large number of cracks, while with the rate of 0.002 s^{-1} the cracks were present only at the lowest temperature here investigated (330 °C).
- The rod extrusion of the short cycle preforms was capable to close the pores of the sintering process. However, the high amount of γ-phase led to a very non-homogeneous microstructure with regions very recrystallized and other regions maintaining the original grain size. The extruded parts showed a very high brittleness. Therefore, it was decided to restrict the investigation on the SPS samples produced by the long cycle only.
- The rod extrusion of long cycle preforms was capable to refine the grain size down to 1.5 μm through dynamic recrystallization. In all samples, a difference in the microstructure between the core and the outer region was detected. The local strain on the outer region caused more refined grains but in some cases, the cracks were also induced.

- The tube extrusion of AZ91 samples was able to break the oxides present on the original powders surface and the dynamic recrystallization took place, refining the grain to 4.5 μm.
- Machining and laser cutting performed on the tube did not damaged the original microstructure, leaving a very homogeneous microstructure for the final stent
- Several defects were found after the laser cutting due to the dimensional control during machining. It was observed that manual machining is not suitable to produce the thin tubes to be cut by laser. The ideal would be to perform cold drawing and achieve the dimensional tolerances required for the process.
- Despite the defects, it was possible to obtain some good stents precursors starting from the AZ91 powder. This can be considered a big step for the development of biodegradable stents made of Mg alloys.

References

[1] Q. Ge, D. Dellasega, A. G. Demir,M. Vedani, *The processing of ultrafine-grained Mg tubes for biodegradable stents,* Acta Biomaterialia*,* ***2013****. p. 1–7.*

[2] *F. Witte, The history of biodegradable magnesium implants: a review.,* Acta biomaterialia*,* **2010**. 6(5): p. 1680–1692.

[3] G. Straffelini, A P. Nogueira, P. Muterlle, C. Menapace, *Spark plasma sintering and hot compression behaviour of AZ91 Mg alloy,* Materials Science and Technology, **2011**. 27(10): p. 1582–1587.

[4] Y. Chen, Q. Wang, J. Peng, C. Zhai, W. Ding, *Effects of extrusion ratio on the microstructure and mechanical properties of AZ31 Mg alloy,* Journal of Materials Processing Technology, **2007**. 182(1-3): p. 281-285.

[5] T. Murai, S. Matsuoka, S. Miyamoto, Y. Oki, *Effects of extrusion conditions on microstructure and mechanical properties of AZ31B magnesium alloy extrusions,* Journal of Materials Processing Technology, **2003**. 141(2): p. 207-212.

[6] X. J. Wang, L. Xu, X. S. Hu, K. B. Nie, K. K. Deng, K. Wu, M. Y. Zheng, *Influences of extrusion parameters on microstructure and mechanical properties of particulate reinforced magnesium matrix composites,* Materials Science and Engineerging: A, **2011**. 258(21): p. 6387–6392.

[7] S. Zhang, X. Zhang, C. Zhao, J. Li, Y. Song, C. Xie, H. Tao, Y. Zhang, Y. He, Y. Jiang, Y. Bian, *Research on an Mg-Zn alloy as a degradable biomaterial.* Acta Biomaterialia, **2010**. 6(2): p. 626–640.

[8] W. N. A. W. Muhammad, Z. Sajuri, Y. Mutoh, Y. Miyashita, *Microstructure and mechanical properties of magnesium composites prepared by spark plasma sintering technology,* Journal of Alloys and Compounds, **2011**. 509(20): p. 6021–6029.

[9] N. Muhammad, D. Whitehead, A. Boor, L. Li, *Comparison of dry and wet fibre laser profile cutting of thin 316L stainless steel tubes for medical device applications,* Journal of Materials Processing Technology, **2010**. 210(15): p. 2261-2267.

[10] M. Baumeister, K. Dickmann, T. Hoult, *Fiber laser micro-cutting of stainless steel sheets,* Applied Physics A, **2006**. 85(2): p. 121–124.

[11] A. Gökhan Demir, B. Previtali, *Comparative study of CW, nanosecond- and femtosecond-pulsed laser microcutting of AZ31 magnesium alloy stents,* Biointerphases, **2014.** 9(2) p. 029004.

[12] A. Raval, A. Choubey, C. Engineer, D. Kothwala, *Development and assessment of 316LVM cardiovascular stents,* Materials Science and Engineering A, **2004**. 386(1–2): p.331–343.

[13] J. Cheng, C. S. Liu, S. Shang, D. Liu, W. Perrie, G. Dearden,K. Watkins, *A review of ultrafast laser materials micromachining,* Optics and Laser Technology, **2013**. 46(88-102): p. 88–102.

[14] H. Meng, J. Liao, Y. Zhou, Q. Zhang, *Laser micro-processing of cardiovascular stent with fiber laser cutting system,* Optical Laser Technology, **2009.** 41(3): p. 300–302.

[15] A. G. Demir, B. Previtali, C. A. Biffi, *Fibre laser cutting and chemical etching of AZ31 for manufacturing biodegradable stents,* Advances in Materials Science and Engineering, **2013** p. 1-11.

[16] A. G. Demir, B. Previtali, Q. Ge, M. Vedani, W. Wu, F. Migliavacca, L. Petrini, C. A. Biffi, M. Bestetti, *Biodegradable magnesium coronary stents: material, design and fabrication,* International Journal of Computer Integrated Manufacturing, **2013**. p.1–10.

[17] A. Redaelli, F. Montevecchi*, Analisi multiscala di tessuti biologici.* **2012.** Pàtron.

[18] M. Crivellini, M. Galli*, Sanità e Salute, due storie diverse.* **2011**. Franco Angeli.

[19] D. Hall, A. Gruentzig, *Percutaneous transluminal coronary angioplasty: current procedure and future direction.* American journal of roentgenology. **1984**. 142(1): p.13–26.

[20] G. Mani, M. D. Feldman, D. Patel, C. M. Agrawal, *Coronary stents: a materials perspective.,* Biomaterials, **2007**. 28(9): p. 1689–1710.

[21] A. G. Demir, B. Previtali, Q. Ge, M. Vedani, F. Migliavacca, L. Petrini, W. Wu, *Design and production of biodegradable cardiovascular stents in magnesium,* 1st International Conference on Design and Processes for Medical Devices PROMED, **2012**. Brescia.

[22] P. Serruys, P. de Jaegere, F. Kiemeneij, C. Macaya, W. Rutsch, G. Heyndrickx, H. Emanuelsson, J. Marco, V. Legrand, P. Materne, J. Belardi, U. Sigwart, A. Colombo, J. J. Goy, P. van den Heuvel, J. Delcan, M. Morel*, A comparison of balloon- expandable-stent implantation with balloon angioplasty in patients with coronary artery disease,* The New England Jounal of Medicine, **1994**. 331: p. 489–495.

[23] J. Justice, C. Yacono, *Use of drug-eluting stents for patients with coronary heart disease,* Journal of the American Academy of Physician Assitants, **2009**. 22(6): p. 30–34.

[24] A. Abizaid, J. R. Costa, *New drug-eluting stents an overview on biodegradable and polymer-free next-generation stent systems, Circulation:* Cardiovascular Interventions, **2010**. 3(4): p. 384–393.

[25] S. Garg, P. W. Serruys, Coronary stents: looking forward., Journal of the American College of Cardiology, **2010**. 56(10) p. S43–S78.

[26] H. Hermawan, D. Dubé, D. Mantovani, *Developments in metallic biodegradable stents.,* Acta Biomaterialia, **2010.** 6(5): p. 1693–1697.

[27] M. Peuster, P. Wohlsein, M. Brügmann, M. Ehlerding, K. Seidler, C. Fink, H. Brauer, A. Fischer, G. Hausdorf, *A novel approach to temporary stenting: degradable cardiovascular stents produced from corrodible metal-results 6-18 months after implantation into New Zealand white rabbits.,* Heart, **2001**. 86(5): p. 563–569.

[28] M. Moravej, D. Mantovani, *Biodegradable metals for cardiovascular stent application: interests and new opportunities.,* International Journal of Molecular Sciences, **2011**. 12(7): p. 4250–70.

[29] H. E. Friedrich, B. L. Mordike, *Magnesium technology: Metallurgy, design data, applications.* **2006**. Springer.

[30] M. O. Pekguleryuz, K. U. Kainer, A. Arslan Kaya, N. R. Neelameggham, S. Shang, Z.-K. Liu, C. L. Mendis, K. Hono, M. Pekguleryuz, M. R. Barnett, S. Bender, J. Göllner, A. Heyn, C. Blawert, P. Bala Srinivasan, A. A. Luo, H. Dieringa, F. Witte*, Fundamentals of Magnesium Alloy Metallurgy.* **2013**. Elsevier.

[31] K. U. Kainer, *Magnesium – Alloys and Technology.* **2003**. Wiley

[32] I. J. Polmear*, Magnesium alloys and applications,* Materials Science and technology, **1994**. 10(1): p. 1–16.

[33] D. J. Sakkinen*, Physical Metallurgy of Magnesium Die Cast Alloys",*SAE Technical Paper. **1994**. p. 940779.

[34] *C. R. Brooks, Heat Treatment, Structure, and Properties of Nonferrous Alloys.* **1982**. American Society for Metals.

[35] Z. Zhang, A. Couture, A. Luo, *An investigation of the properties of Mg-Zn-Al alloys,* Scripta Materilalia, **1998**. 39: p. 45–53.

[36] Y. Lü, Q. Wang, W. Ding, X. Zeng, Y. Zhu, *Fracture behavior of AZ91 magnesium alloy,* Materials Letters, **2000**. 44(5): p. 265–268.

[37] S. W. Xu, N. Matsumoto, S. Kamado, T. Honma, Y. Kojima, *Effect of Mg17Al12 precipitates on the microstructural changes and mechanical properties of hot compressed AZ91 magnesium alloy,* Materials Science and Engineering A, **2009**. 523(1–2): p. 47–52.

[38] Q. Peng, Y. Huang, L. Zhou, N. Hort, K. U. Kainer, *Preparation and properties of high purity Mg-Y biomaterials.,* Biomaterials, **2010**. 31(3): p. 398–403.

[39] M. O. Pekguleryuz, K. U. Kainer, A. Arslan Kaya, F. Witte, *Fundamentals of Magnesium Alloy Metallurgy.* **2013**. Elsevier.

[40] F. Lux, R. Zeisler, J. Schuster, *Activation analysis of the metabolic behaviour of corrosion products and biological tracer elements in tissue affected by metallosis,* AED-Conf--75-404-027, **1975**. Germany.

[41] J. Romesburg, P. Wasserman, ja C. Schoppe, *Metallosis and Metal-Induced Synovitis Following Total Knee Arthroplasty: Review of Radiographic and CT Findings",* Journal of Radiology Case Reports, **2010**. 4(9): p. 7–17.

[42] F. Witte, V. Kaese, H. Haferkamp, E. Switzer, A. Meyer-Lindenberg, C. J. Wirth, H. Windhagen, *In vivo corrosion of four magnesium alloys and the associated bone response,* Biomaterials, **2005**. 26(17): p. 3557–3563.

[43] F. Witte, N. Hort, C. Vogt, S. Cohen, K. U. Kainer, R. Willumeit, F. Feyerabend, *Degradable biomaterials based on magnesium corrosion,* Current Opinion in Solid State and Materials Sciences, **2008.** 12(5–6), p. 63–72.

[44] A. Eliezer ja F. Witte, *Corrosion Behavior of Magnesium Alloys in Biomedical Environments,* Advanced Materials Research, **2010**. 95: p. 17–20.

[45] B. Heublein, R. Rohde, V. Kaese, M. Niemeyer, W. Hartung, A. Haverich, *Biocorrosion of magnesium alloys: a new principle in cardiovascular implant technology?,* Heart, **2003**. 89(6): p. 651–656.

[46] W.D. Mueller, M. F. L. de Mele, M. L. Nascimento, M. Zeddies, *Degradation of magnesium and its alloys: dependence on the composition of the synthetic biological media.,* Journal of Biomedical Materials Research A, **2009**. 90(2): p. 487–495.

[47] P. Peeters, M. Bosiers, J. Verbist, K. Deloose, ja B. Heublein, *Preliminary results after application of absorbable metal stents in patients with critical limb ischemia.,* Journal of Endovascular Therapy, **2005**. 12(1): p. 1–5.

[48] H. Wang, Y. Estrin, ja Z. Zúberová*, Bio-corrosion of a magnesium alloy with different processing histories,* Materials Letters, **2008**. 62(16): p. 2476–2479.

[49] H. Hornberger, S. Virtanen, A. R. Boccaccini, *„Biomedical coatings on magnesium alloys - a review.“*, Acta Biomaterialia, **2012**. 8(7): p. 2442–2455.

[50] E. Lesma, B. Previtali, M. Bestetti, L. Petrini, ja W. Wu, *Manufacturing of biocompatible magnesium stent mesh using nanosecond fiber laser,* Proceedings of 2nd Symposium on Biodegradable Metals, **2010**. Maratea.

[51] S. Farè, Q. Ge, M. Vedani, G. Vimercati, D. Gastaldi, F. Migliavacca, L. Petrini, S. Trasatti, *Evaluation of material properties and design requirements for biodegradable magnesium stents,* Revista Matéria, **2010**. 15(2): p. 96–103.

[52] J. E. Gray-Munro, C. Seguin, M. Strong, *Influence of surface modification on the in vitro corrosion rate of magnesium alloy AZ31.,* Journal of Biomedical Materials Research A, **2005**. 91(1): p. 221–230.

[53] T. S. Kim, H. J. Chae, J. K. Lee, H. G. Jung, Y. Do Kim, J. C. Bae, *Effect of Powder Size of Mg-Zn-Y Alloy on the Consolidation,* Materials Science Forum, **2007**. 534–536, p. 793–796.

[54] J. K. Lee, T. S. Kim, H. G. Jeong, J. C. Bae, *„Microstructures and Mechanical Properties of Consolidated Mg-Zn-Y Alloy“,* Mater. Sci. Forum, **2007**. 534–536: p. 833–836.

[55] M. Sauer, G. Bauser, K. Siegert*, Extrusion, second edition. **2006**.* ASM International

[56] G. E. Dieter, D. Bacon, *Mechanical metallurgy : SI metric edition.* **1988**. London: McGraw-Hill Book Company.

[57] M. Hu, Z. Ji, X. Chen*, Effect of extrusion ratio on microstructure and mechanical properties of AZ91D magnesium alloy recycled from scraps by hot extrusion,* Transactions of Nonferrous Metallic Society of China, **2010**. 20(6): p. 987–991.

[58] R. Y. Lapovok, M. . Barnett, C. H. Davies, *Construction of extrusion limit diagram for AZ31 magnesium alloy by FE simulation,* Journal of Materials Processing Technology, **2004**. 146(3): p. 408–414.

[59] N. Ravi Kumar, J. Blandin, C. Desrayaud, F. Montheillet, M. Suéry, *Grain refinement in AZ91 magnesium alloy during thermomechanical processing*, Materials Science and Engineering A, **2003**. 359(1–2): p. 150–157.

[60] D. M. Lee, B. K. Suh, B. G. Kim, S. Lee, C. H. Lee, *Fabrication, microstructures, and tensile properties of magnesium alloy AZ91/SiCp composites produced by powder metallurgy,* Materials Science and Technology, **1997.** 13: p. 590–595.

[61] B. N. Chichkov, C. Momma, S. Nolte, F. Alvensleben, A. Tünnermann, *Femtosecond, picosecond and nanosecond laser ablation of solids, Applied Physics A:* Materials Science and Processing, **1996**. 63(2): p. 109–115.

[62] W. Schulz, U. Eppelt, R. Poprawe, *Review on laser drilling I. Fundamentals, modeling, and simulation,* Journal of Laser Applications, **2013**. 25(1): p. 012006.

[63] ASTM E112-13, *Standard Test Methods for Determining Average Grain Size,* ASTM International, **2013**. www.astm.org.

[64] L. Lutterotti, S. Matthies, H.R. Wenk, A. S. Schultz, J. W. Richardson, *Combined texture and structure analysis of deformed limestone from time-of-flight neutron diffraction spectra,* Journal of Applied Physics, **1997**. 81(2): p. 594.

[65] T. Zhang, Y. Shao, G. Meng, Z. Cui, F. Wang, *Corrosion of hot extrusion AZ91 magnesium alloy: I-relation between the microstructure and corrosion behavior,* Corrosion Science, **2011**. 53(5): p. 1960–1968.

[66] H. Ding, L. Liu, S. Kamado, W. Ding, Y. Kojima, *Investigation of the hot compression behavior of the Mg–9Al–1Zn alloy using EBSP analysis and a cellular automata simulation,* Modelling and Simulation in Materials Science and Engineering, **2009**. 17(2): p. 025009.

[67] C. Fang, J. Zhang, A. Liao, S. Xue, F. Yuan, F. Pan, *Hot compression deformation characteristics of Mg-Mn alloys,* Transactions of Nonferrous Metallic Society of China, **2010**. 20(10): p. 1841–1845.

[68] J. G. Lenard ja J. A. Schey, *Metal forming science and practice.* **2002**. Elsevier.

[69] H. Frost, *Deformation-mechanism maps : the plasticity and creep of metals and ceramics.* **1982.** Oxford [Oxfordshire]: Pergamon Press.

[70] C. I. Chang, C. J. Lee, J. C. Huang, *Relationship between grain size and Zener–Holloman parameter during friction stir processing in AZ31 Mg alloys, Scripta Materialia,* **2004**. 51(6): p. 509–514.

[71] J. Li, J. Xie, J. Jin, Z. Wang, *Microstructural evolution of AZ91 magnesium alloy during extrusion and heat treatment,* Transactions of Nonferrous Metallic Society of China*,* **2012**. 22(5): p. 1028–1034.

[72] M. Mabuchi, K. Kubota, K. Higashi, *New recycling process by extrusion for machined chips of AZ91 magnesium and mechanical properties of extruded bars,* Materials Transactions, JIM, **1995**. 36(10): p. 1249-1254.

[73] J. W. Morris, *The Influence of Grain Size on the Mechanical Properties of Steel,* in International Symposium on Ultrafine Grained Steels, **2001**. Tokyo.

[74] G. Nussbaum, P. Sainfort, G. Regazzoni, H. Gjestland, *Strengthening mechanisms in the rapidly solidified AZ 91 magnesium alloy,* Scripta Metallurgica, **1989**. 23(7): p. 1079–1084.

[75] F. Czerwinski, *Magnesium Alloys - Design, Processing and Properties.,* ***2*011**. InTech.

[76] H. Somekawa ja T. Mukai, *Effect of grain refinement on fracture toughness in extruded pure magnesium,* Scripta Materialia, **2005**. 53(9): p. 1059–1064.

[77] G. Fang, W. Ai, S. Leeflang, J. Duszczyk, ja J. Zhou, *Multipass cold drawing of magnesium alloy minitubes for biodegradable vascular stents., Materials Science and Engineering C: Materials for Biological Applications,* **2013**. 33(6): p. 3481-3488*.*

Scientific Production

International Journal

[1] Botelho, P.A.O, Straffelini, G., Menapace, C., Mostaed, E., Vedani, M. *Extrusion behavior of AZ91 Mg alloy produced by spark plasma sintering*. Materials Science and Technology, **2014**. 30: p.1959 - 1965.

[2] Botelho, P.A.O, Straffelini, G., Menapace. *Spark Plasma Sintering and Hot Compression Analysis of Pure Mg and AZ91 Alloy*. Materials Science Forum. **2014**. 802: p.467 - 471.

[3] Mostaed, E., Ge, Q., Vedani, M., Botelho, P.A.O., Zanella, C., Deflorian, F. Investigation on the influence of grain size on strength, ductility, and corrosion properties in Mg and Mg-Zn based alloys for biodegradable stents. European Cells & Materials. **2013**. 26: p.84.

Conference Proceedings

[1] Botelho, P.A.O, Straffelini, G., Menapace, C. *Extrusion behaviour of AZ91 Mg alloy produced by spark plasma sintering*, PTECH 2013, **2013**. Campos do Jordão, Brazil.

[2] Botelho, P.A.O, Straffelini, G., Menapace, C., Vedani, M. *Production of Mg-based preforms by Spark Plasma Sintering for subsequent hot extrusions*. PM World Congress 2014, **2014**. Orlando, FL, USA,

[3] Mostaed, E., Ge, Q., Vedani, M, Botelho, P.A.O, Zanella, C, Deflorian, F. Mechanical properties and corrosion behaviour of ZK60 processed by ECAP for biomedical application. 5th Symposium on Biodegradable Metals, 2013. Indonesia.

[4] Ge, Q., Mostaed, E., Vedani, M., Botelho, P.A.O, Zanella, C., Deflorian, F.. *ECAP processed ZM21Mg alloy and pure Mg for high strength biodegradable stents,* ISMANAM 2013. **2013.** Torino, Italy

[5] Angelini, L., Guerra, F., Persi, C., Straffelini, G. Botelho P.A.O. *Quality improvement of the Acciaierie di Calvisano continuous casting machine through the electromagnetic multistirring technology.* 8th European Continuous Casting Conference. **2013.** Graz, Austria.

Acknowledgements

This research would not have been possible without the support of the support from Fondazione Cassa di Risparmio di Trento e Rovereto (Trento, Italy) and CAPES for founding the research.

I wish to express my special gratitude to my supervisor, Prof. Dr. Giovanni Straffelini, who was abundantly helpful and offered invaluable support and guidance.

Special thanks also to all laboratory colleagues, especially to Cinzia, Luiz, Pablo, Simone, Ibrahim, Marco, Faraz, Anna, Melina, Nicolo, Elisa, Lorena, Samuel, Saliou, Piergiorgio and Sara for the sharing knowledge and friendship during the PhD period.

My gratitude to all friends I have done in Trento, especially Maddalena, Leandro, Andrea, Simona, Dani, Franco. The “Celeti’s”: Miriam, Gennaro, Noemi, Marcio, Andre, Mary, Ruben, Gerson, Maite for being my second family and supporting us in the difficult moments and celebrating the happy ones.

To my Brazilian friends that supported me overseas, Priscila, Frank, Esther, Jhonnathan, Vanessa e Mateus, who made me use all my 3G data on WhatsApp conversation.

Thanks also to my engineering colleagues, Matheus, Rodrigo and Guilherme.

My thanks also to my parents, Guto e Luciana, who in all times were there for me.

I wish to express my love and gratitude to my beloved wife, Bruna, who was a real support during all the PhD period, for her patience with me in the difficult moments. To my daughters Luisa and Ana, that are the inspiration of my life.

Finally, I would like to thank God for giving me strength and energy to perform this work.